Atmospheric Corrosion of Austenitic Stainless Steels

by

Steven Richard Street

A thesis submitted to the University of Birmingham for the degree of DOCTOR OF PHILOSOPHY

School of Metallurgy and Materials

College of Engineering and Physical Sciences

University of Birmingham

September 2016

Abstract

Atmospheric corrosion was investigated using electrochemical and droplet studies. The effects of changes in bulk solution concentration and local pit chemistry on pit propagation and repassivation of 304L and 316L stainless steels were investigated using *in situ* synchrotron X-radiation and electrochemical techniques.

Radiography and zig-zag electrochemical sweeps showed that in dilute chloride solutions, partial passivation was observed to initiate locally and propagate across the corroding surface. This caused repassivation gradually rather than as a uniform event. In concentrated chloride solutions, repassivation did not show a sudden drop in current but rather a gradual decrease as potential swept down. Pitting behaviour was also affected by solution concentration. Dilute solutions showed metastable pitting followed by a sharp breakdown (pitting) potential. Concentrated solutions however showed no metastability and a gradual increase in current when pitting.

To determine the cause of current oscillations in 304L artificial pits in NaCl:$NaNO_3$ solutions near the repassivation potential, the salt layers were scanned *in situ* using XRD. The salt layer was confirmed to be $FeCl_2.4H_2O$ and no nitrate salt was found. A mechanism was suggested to explain the current oscillations in terms of partial passivation being undercut by the advancing corrosion front.

The morphology of pits caused by atmospheric corrosion of 304L plate under droplets of $MgCl_2$ was investigated. Changes in pit morphology were linked to relative humidity and droplet thickness. Initial pit morphology showed a shallow dish region, which is suggested to be caused by elevated passive current dissolution under high concentrations. Position of pits under the droplet was linked to initial

solution concentration. Distinctions between Aerosol and “Splash zone” salt depositions were investigated.

Acknowledgments

A great many people helped to guide me through this body of work and I am sincerely thankful to each of them.

Both my supervisors, Prof Alison Davenport and Prof Trevor Rayment, have shown inexhaustible patience with the meandering path that my research has taken. Many thanks to them and also to all my colleagues in the corrosion research group, who are too numerous to name but have helped me immensely.

I gratefully acknowledge all the assistance that I have received from Diamond Light Source Ltd., particularly Dr Fred Mosselmans and Dr Mahrez Amri of I18, Dr Paul Quinn of I14, Dr Christoph Rau and Dr Joan Vila-Comamala of I13, and Dr Mark Basham of the Software Development Team.

Finally, I would like to thank my family for their continued support, love, and encouragement.

Dedicated to my wife and my daughter.

"*When I was a child, I spake as a child, I understood as a child, I thought as a child: but when I became a man, I put away childish things*."

- 1 Corinthians 13:11

Contents

LIST OF SYMBOLS AND DEFINITIONS

1D	one-dimensional
A	surface area
b_a	Tafel slope
D	average diffusivity
DH	Deliquescence Humidity
E_{app}	Applied potential
E_{corr}	Corrosion Potential
E_{pass}	Primary passivation potential
E_{pit}	Pitting potential
E_{rp}	Repassivation potential
F	Faraday constant
H_0	Null Hypothesis
i	current density
i_a	anodic current density
i_{corr}	open circuit corrosion current density
i_{lim}	diffusion-limited current density
I_{lim}	diffusion-limited current
Int	transmission beam intensity
Int_0	original beam intensity
M_w	average molecular weight of an alloy
n	average valency of an alloy
n_i	integer for Bragg equation
Q	total charge passed
R	Universal gas constatn
RH	Relative Humidity
R_{SD}	Surface Roughness
R_j	Roughness and point j
R_m	Mean roughness
wt%	weight per cent of alloy
x	pit depth
x_t	absorption thickness
ΔC	difference in metal ion concentration between the corrosion interface and the bulk solution
μ	absorption coefficient
ρ	average alloy density
$\boldsymbol{\sigma_{H_0}}$	Binomial standard deviation of the null hypothesis
φ_s	IR-drop across solution
φ_{sf}	IR drop across salt film
χ^2	Chi-squared

1. Introduction

Austenitic stainless steels are currently used in the United Kingdom to build containers to store Intermediate Level Nuclear Waste (ILW), with 304L and 316L alloys being the primary choices. The eventual plan for this waste is to place it underground in a geological disposal facility permanently [1]. However, this facility has not yet been built and it may be one hundred years before it will be ready to accept ILW. In the meantime, ILW containers are kept in warehouses that are vulnerable to salty aerosol deposits [2]. These aerosol deposits come from a variety of sources, such as crashing waves in the sea [3], and commonly have salt species in them. There are other species amongst the salts, such as nitrates which are thought to originate from farming contamination. Nitrates are known to cause surges in electrochemical dissolution, yet the mechanism explaining this has not been confirmed. There is a risk that over the next century, atmospheric corrosion may occur on these ILW containers and provide initiation sites for stress corrosion cracking to occur, causing the containers to fail when being moved from interim storage to their final destination.

The salts that are deposited on the surface of these containers are hygroscopic, i.e. draw in moisture from the surrounding atmosphere [4]. As humidity fluctuates throughout the year it is possible for these salts to draw in enough moisture to become highly concentrated saline solutions. This leads the stainless steel to be vulnerable to localised corrosion. The humidity at which a salt begins to draw in moisture is known as its “deliquescence” humidity, which is a thermodynamic property for each salt. $MgCl_2$ is of particular relevance in atmospheric corrosion due

to its presence in sea water and aerosol depositions, and its relatively low deliquescence RH that is commonly quoted as 33% at 30 °C [5].

Recent developments in synchrotron techniques have allowed the observation of pitting behaviour *in situ* using a range of techniques X-ray diffraction [6, 7] and radiography[8-10]. The high flux and high resolution of synchrotron techniques allow time-resolved results to be collected and correlated with electrochemical data.

Atmospheric corrosion occurs in highly concentrated solutions, although the vast majority of electrochemical corrosion investigations have occurred in dilute solutions. There has been some evidence that the behaviour of corrosion changes in higher concentrations [11, 12], so further investigation in conditions comparable to those in atmospheric corrosion is warranted.

As pit morphologies are complicated, one-dimensional artificial pitting electrodes have been used to simplify analysis of results [13]. The regular geometry of these pits allows realistic values of current density and threshold potentials to be collected, such as the transition between diffusion-limited dissolution and active dissolution, and active dissolution and repassivation.

The principal aims of this body of research are to investigate the localised corrosion of 304L and 316L in terms of interfacial kinetics and repassivation. The influence of nitrate on the mechanism of repassivation of 304L is here investigated using synchrotron radiation to analyse the corroding salt layer during dissolution and when a near repassivation in addition to electrochemical analysis [14]. Repassivation of 304L and 316L in $MgCl_2$ solutions are conducted in highly concentrated solutions to

give insight on repassivation behaviour in atmospheric corrosion conditions, as repassivation is most commonly described in terms of dilute solutions [15, 16].

The influence of initial solution concentration of droplets of $MgCl_2$ on both the morphology and the position of pitting of 304L is also investigated. This will allow analysis of principal mechanisms of propagation in pits found in service that do not often conform to morphologies predicted by electrochemical models of corrosion [13, 17].

2. Literature review

2.1. Austenitic stainless steel

Stainless steels are Cr-rich steels that are highly resistant to general corrosion due to the growth of very stable chromium oxide film on the metal surface. A steel is stainless if it is able to regenerate this chromium oxide layer film after damage, usually requiring at least 11 wt% Cr in solid solution to allow this [18].

There are generally considered to be four categories of stainless steels: ferritic, martensitic, austenitic and duplex [19]. Although steel maintains a face centre cubic (FCC) crystal structure at elevated temperatures, this normally reverts to body centre cubic (BCC) as the alloy cools. The addition of FCC stabilisers, such as Ni, allows FCC structure to be maintained at low temperatures. 300 series alloys have 18 wt% Cr is added to maintain a durable passive layer and promote corrosion resistance. As Cr acts as a ferrite stabiliser, promoting BCC crystal structure at room temperature, 8-10 wt% Ni is also added to maintain the FCC structure.

The most common austenitic grades are 304 and 316 stainless steels, each with approximately 18 wt% Cr and 10 wt% Ni. 316 has an additional 2-3 wt% Mo which has been observed to enhance its ability to prevent pitting corrosion [19]. Low carbon grades of these alloys are denoted with ‘L’ as a suffix: 304L and 316L. These are desirable as they prevent the formation of carbides at grain boundaries that may locally reduce Cr content in solid solution.

2.2. Pitting Corrosion of stainless steels

2.2.1. Introduction

Stainless steels are generally considered to have excellent resistance against general corrosion because of the very stable chromium oxide film that reforms after it is damaged by any scratches in normal use. However, they are susceptible to localised corrosion caused by defects and surface-breaking inclusions in the material microstructure. These inclusions form from alloying elements and impurities introduced during the iron- and steel-making phases of production.

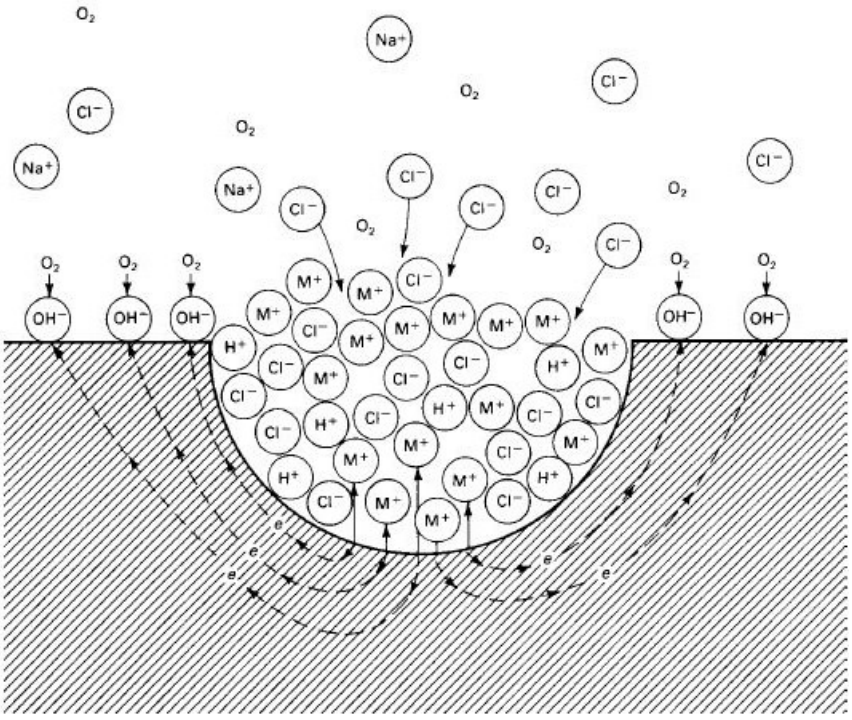

Figure 2-1 Schematic diagram of the key processes involved in pitting of metal in NaCl solution. Anodic reaction is the dissolution of metal and cathodic reaction is the oxygen reduction reaction.[20, 21].

Pitting is an autocatalytic process (Figure *2-1*) where the propagation of pitting creates an environment more susceptible to corrosion. This is enabled by the occluded morphologies generated during the pitting process.

2.2.2. Initiation of pitting

2.2.2.1. Role of Sulphur during solidification

The initiation of pitting in stainless steels has been most widely attributed to the presence of surface-breaking inclusions on the metal surface [22]. Although other mechanisms have been suggested, these generally focus on the structure of the oxide film and are independent of underlying inclusions [23-26] and are most useful in explaining very clean systems such as deposited thin films. Bulk alloys, such as austenitic stainless steels, are typically discussed in terms on initiation at an inclusion [27].

Sulphide inclusions are considered the most significant type of inclusion when considering pitting initiation of stainless steels [28]. Sulphur (S) is introduced into the alloy as an impurity from ore and coke supplies [29] and great pains are taken to remove sulphur from the melt, particularly in the iron-making stage. Alloying additions are used to remove S by reacting it to float off as a buoyant slag. Most commonly lime (CaO) is added but Mg, Na and rare earths are also used.

Not all S can be economically removed in this way and to further mitigate its effect on the alloy elements, such as Mn, are added to the alloy [19]. Mn forms MnS at 1650 °C, 80 degrees above the solidus temperature of the bulk, allowing the overwhelming majority of S in the alloy to be reacted with Mn without preference for grain boundary positions. MnS is also quite ductile, so does not form voids or sharp stress concentrators as it is rolled or formed. Although some stainless steels contain relatively high amounts of S (~0.3 wt%) to improve machinability, e.g.

SS303, most austenitic stainless steel alloys aim to have S content below 0.08 wt% and often below 0.03 wt% [19].

2.2.2.2. Role of MnS inclusions

Localised corrosion in stainless steels was suspected to be influenced by S inclusions long before initiation mechanisms were established [30, 31]. Eklund [32] developed a Pourbaix diagram for MnS and showed sulphides are not thermodynamically stable at the potentials experienced by passive steels, resulting in the lowering of pH locally. Eklund also suggested an initiation mechanism where "virgin" steel under a newly dissolved sulphide is able to be attacked.

Wranglen [33] observed pitting initiating under sulphide inclusions in steel, commenting that the inclusions were less noble than the surrounding matrix and their dissolution resulted in pit solution with higher salt concentration, lower oxygen concentration and lower pH. Wranglen rejected Eklund's idea that the MnS is an anode, which would "shower" the surrounding matrix with S. Instead, Wranglen suggests S^{2-} and HS^{-} strongly adsorb to the surface of metal, reducing activation overpotential.

Castle and Ke [34] suggest a sulphite intermediary existed that lowers local pH to help stabilise pitting. The importance of the intermediary thiosulphate species has been observed to lower pH and stabilise pitting during sulphide dissolution [35]. A suggested mechanism for this is :

$$2MnS + 3H_2O \rightarrow 2Mn^{2+} + S_2O_3^{2-} + 6H^+ + 8e^- \qquad \textit{Equation 2-1}$$

$$MnS + 2H^+ \rightarrow Mn^{2+} + S + H_2 \qquad \textit{Equation 2-2}$$

It has been suggested that preferential dissolution of Cr at the S inclusion interface is the key feature that promotes the stability of pitting around sulphide inclusions [36] but this has not been broadly accepted [37, 38]. However, preferential attack around the edge of sulphide inclusions has been observed using scanning auger microscopy [39] and optical microscopy [40, 41].

Williams *et al.*[42] have shown a FeS region around sulphide inclusions up to 100 nm thick using secondary ion mass spectroscopy. They hypothesised that this will lead to the formation of a polysulphide skin around the inclusion that will trigger its dissolution.

2.2.3. Propagation of pitting

The growth of pits after initiation depends on the ability of the solution around the corroding surface to maintain an aggressive concentration and resist repassivation, i.e. the maintenance of a critical concentration [43]. In terms of electrochemical potential, a pit can be considered to propagate as long as the interfacial potential is above the repassivation potential, E_{rp}. However, E_{rp} varies in definition between authors and applications, which will be discussed later.

Hoar [44] first suggested that an autocatalytic mechanism could be responsible for the sustainability of pitting propagation, with the chemistry inside the pit being different than that of the bulk. In neutral solutions, evidence of a significant drop in pH was observed in inside pits [45, 46] and this was achieved by hydrolysis caused by metal ion (M) release:

$$M \rightarrow M^{n+} + ne^{-} \qquad \textit{Equation 2-3}$$

$$M^{n+} + H_2O \rightleftharpoons MOH^{(n-1)+} + H^{+} \qquad \textit{Equation 2-4}$$

This reduction in pH destabilises any passive film growth, maintaining actively corroding surfaces. The release of large volumes of cations into the pit causes a charge imbalance, which is corrected by the electromigration of anions from the bulk solution into the pit [18]. Cl^- is a particularly aggressive anion as it acts like a strong acid when in solution, i.e. it remains fully dissociated from free H^+ ions. This allows a high concentration of H^+ ions to remain in the pit, further lowering pH. Though there is generally believed to be very little convection inside pits [22], the constant diffusion of ions away from the corrosion interface requires a restricted diffusion pathway to ensure the number of ions being generated is greater than the number of ions exiting the pit. As such, an occluded geometry is typically required for corrosion to continue, resulting in a "pit" morphology (Figure *2-1*).

The occluded pit geometry creates an ion concentration gradient inside the pit with a saturated solution at the corrosion interface. Continued corrosion supersaturates this solution, causing the precipitation of a salt layer that settles at the bottom of the pit [47].

The main cathodic reaction in aqueous corrosion of steels is generally acknowledged to be the Oxygen Reduction Reaction (ORR):

$$2H_2O + O_2 + 4e^{-} \rightarrow 4OH^{-} \qquad \textit{Equation 2-5}$$

The high mobility of electrons through metal allows cathodic and anode reactions to occur at different places on the metal surface, as long as there is a sufficient ion pathway through the solution to allow charge balance. The generation of hydroxyl ions at the cathode increases pH locally, provide cathodic protection against attack in these regions.

2.2.4. Metastable pits

Not all initiation events stabilise into propagation of pits. Those that fail to grow are labelled "metastable", though this is only known after failure to pit as they share the same mechanism of initiation as successful pits [48]. In these cases, although the dissolution of an inclusion occurs, the pitting site is not occluded enough to maintain an aggressive chemistry, so rapidly repassivates [49]. Solution chemistry can affect metastable pitting. In dilute solutions, Pistorius and Burstein observed reducing NaCl solution concentration from 1 M to 0.01 M reduced the occurrence of metastable pitting on 304 stainless steel. They also observed that reducing pH from 9 to 7 increased metastable pitting. Solution concentration also affects metastable pitting, with fewer metastable pits present in highly concentrated solutions of $MgCl_2$ on 304L [12].

2.3. One dimensional pitting

2.3.1. Geometry

The complicated geometry of pits allows different regions inside the pit to experience different corrosion behaviours, as explained above. This makes the interpretation of electrochemical data challenging as the current drawn from pits was averaged over the entire pit interface, and it is difficult to isolate physical geometries

of a growing pit in a wire or plate surface. One dimensional pits, or artificial pits, were developed as an experimental model to better understand the electrochemistry recorded during pitting experiments. Pickering and Frankenthal [50, 51] first developed the "unidirectional" model of pitting for metals in acidic solutions, considering diffusion and migration of ions but not convection as it was viewed to be negligible. Galvele [27] further simplified Pickering's model by accounting only for metal ion diffusion and expanding its utility to any pH bulk solution.

One-dimensional pitting occurs when artificial pits are of a sufficient depth that diffusion along the pit is uniform. As seen in Figure 2-2a, corrosion begins with a pit depth of zero, allowing hemispherical diffusion through the bulk solution. As the pit grows, diffusion from the corrosion front is increasingly restricted by the occluded geometry of the pit, allowing solution at the interface to supersaturate and precipitate a salt layer (Figure 2-2b). There is still significant hemispherical diffusion at the pit mouth, however. As the pit continues to grow, hemispherical diffusion of metal ions from the pit mouth will become negligible, meaning in uniform diffusion in the pit (Figure 2-2c). This results in one-dimensional pitting, and electrochemistry can be interpreted as uniform across the surface of the anode.

Isaacs [52] showed the development of resistive layers in one dimensional crevices, suggesting that these were most likely metal chloride salts due to their solubility and diffusion effects, as highly concentrated bulk solutions reduced current significantly.

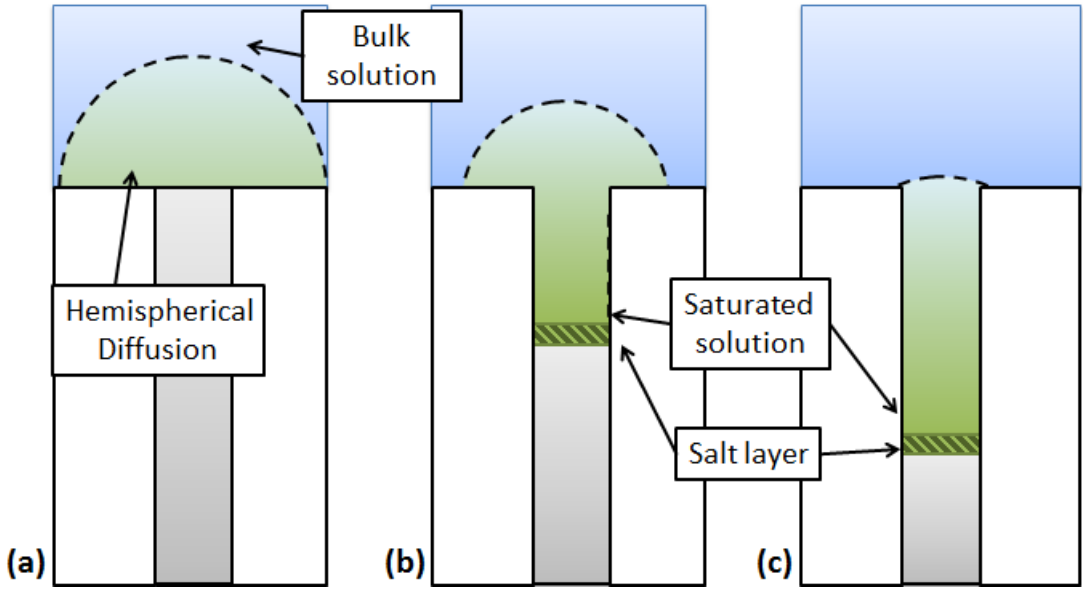

Figure 2-2 Schematic model of one-dimensional pitting experiment. (a) Metal wire embedded in non-corroding polymer initially corrodes with hemispherical diffusion at the pit mouth. (b) Pit with salt layer and some hemispherical diffusion at pit mouth. (c) One-dimensional pit where hemispherical diffusion at pit mouth is negligible.

Beck [53], using titanium cells, also concluded that the drop in potential in the steady state condition was due to the formation of a porous salt layer. Tester and Isaacs [54] went on to develop one-dimensional pitting model assuming a quasi-steady state condition where corrosion rate is controlled by diffusion with a concentration gradient being the driving force. They observed this behaviour in a range of metals, proposing a chloride salt being responsible for the independence of current to applied voltage in each case. The quasi-steady state period is observed after an initial "transient" period, where local pit chemistry is being established at shallow depths (Figure 2-3).

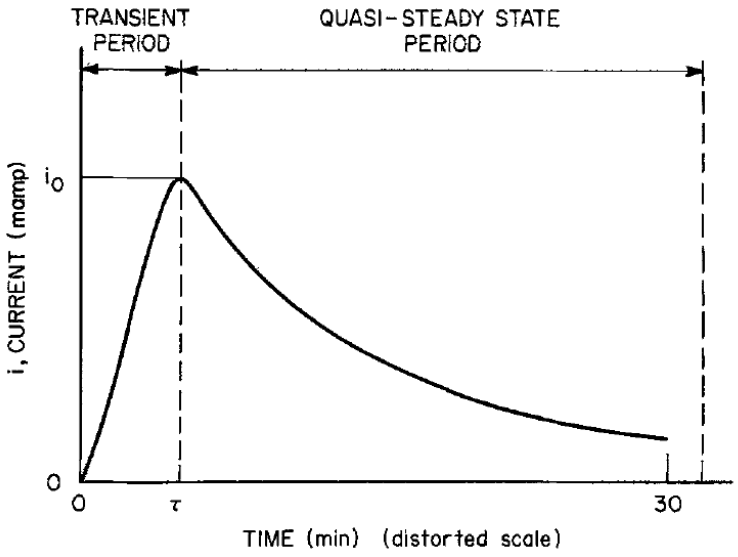

Figure 2-3 Schematic diagram from Tester and Isaacs [54] showing the initial growth of a one-dimensional artificial pit under constant potential. The "transient" region where the pit grows until a salt layer forms at time τ, after which is a region of quasi-steady state attack.

By simplifying the model to account only for mass transport by diffusion, not convection or migration, Tester and Isaacs [54] showed a relationship can be made between current and pit depth. For a wire with a fixed cross-section, the flux of metal ions away from the corrosion interface can be expressed as:

$$N = \frac{I}{AnF} \qquad \textit{Equation 2-6}$$

Where N is the cation mass flux from the interface, I is the current, n is the average number of electrons liberated per cation, F is the Faraday constant, and A is the wire cross-sectional area. The loss of cations at the metal interface will be driven by two processes, namely a concentration gradient and a potential gradient. This can be expressed using the Nernst-Einstein equation

$$\frac{I}{AnF} = D\left[\frac{\delta C}{dx} + \bar{C}\frac{nF}{RT}D\frac{\delta \phi}{\delta x}\right] \qquad \textit{Equation 2-7}$$

Where D is the ionic diffusion coefficient, δC is change in metal cation concentration, δx is change in pit depth, R is the universal gas constant, T is the temperature of the system in K, $\bar{C}$ is the average metal ion concentration in the pit, $\delta \Phi$ is the change in potential. The potential gradient in this system has been observed to have no significant impact in mass transport in one-dimensional pitting under a salt layer, so the equation can be reduced to only consider mass transport via diffusion:

$$\frac{I}{AnF} = D\frac{\delta C}{\delta x} \qquad \textit{Equation 2-8}$$

Simplifying and integrating both sides gives:

$$\int_{x_{min}}^{x_{max}} \frac{I}{A}\,\delta x = \int_{C_{bulk}}^{C_{sat}} nFD\ \delta C \qquad \textit{Equation 2-9}$$

$$\frac{I}{A}[x - 0] = nFD[C_{sat} - C_{bulk}] \qquad \textit{Equation 2-10}$$

Where x_{max} is the pit depth, x_{min} is the top of the pit (i.e. 0), C_{sat} is the saturation concentration of metal ions at the corrosion interface and C_{bulk} is the concentration of metal ions in the bulk. This can be rearranged to give the diffusion limited current density of the pit [27]:

$$i_{lim} = \frac{nFD\Delta C}{x} \qquad \textit{Equation 2-11}$$

Where i is the limiting current density in the pit and ΔC is $C_{sat} - C_{bulk}$. As n, F, D, and ΔC are broadly constant, another relationship can be established:

$$i_{lim}x = nFD\Delta C \qquad \textit{Equation 2-12}$$

$i_{lim}x$ is known as the pit stability product [49] and is constant if one dimensional pitting has been established. If the pit stability product is constant, the hemispherical

diffusion gradient at the mouth of the pit is negligible and pitting can be treated as one-dimensional [54]. Woldemedhin *et al*. [11] used stainless steels in $FeCl_3$ and LiCl with concentrations up to 8.58 M [Cl] to observe a decrease in pit stability product (ix) with increasing solution concentration. Artificial pits have also been extended into two dimensions to see growth under diffusion and ohmic control [8, 55]

2.3.1.1. Measuring Pit Depth

Radiography analysis of 304L corrosion in chloride solution [56] has shown that metal lost during 1D pitting experiments is *via* electrochemical dissolution and very little is lost by flaking, spalling or undercutting. As such, it can be assumed that current can be used to calculate material loss and pit depth during dissolution. The total charge passed during dissolution, Q, is the integration of the current over time. Pit depth can be calculated using Faraday's Second law [52]:

$$x = \frac{QM_W}{AnF\rho} \qquad \textit{Equation 2-13}$$

where x is pit depth and A is surface area of pit, M_w is average molecular weight of alloy, n is average valence of alloy, F is Faraday Constant and ρ is average alloy density. This method of measuring material loss has shown high levels of repeatability for austenitic stainless steels when compared to optical measurements [57, 58].

2.3.2.Salt layers

Salt layers are formed when solutions inside the pit have become supersaturated with ions during high anodic dissolution. Supersaturation is a necessary step to precipitate

a salt layer [59] with current density required to nucleate a salt layer ranging from 1.8 times to 5 times the diffusion limited current density [15, 60, 61]

Salt layers are in a dynamic equilibrium with the pit solution and are continually dissolving and reforming while corrosion continues [62]. Isaacs [52] showed that corroded 304L stainless steel one-dimensional pits in chloride solutions and have salt layers that are highly resistive. The salt layer at the bottom of a pit was originally believed to be non-porous, but this idea was refined to include a hydrated layer that allowed water to pass through it [47]. Danielson then investigated the response of the salt layer to incremental steps in applied current, coming to the conclusion that it should be considered a porous layer [63]. Landolt *et al.*[64-66] suggested a "duplex" structure of the salt layer, with a compact anhydrous region at the corrosion interface and a loosely packed region closer to the bulk solution. This model was developed using results from Fe and Ni alloys. This duplex model has been used to calculate porosity of outer regions of salt layers in Fe systems in chloride solutions [67].

The structure of salt layers has been investigated *in situ* using a range of methods. Sridhar and Dunn [68] used Raman to identify the salt layer at the bottom of a Ni pit to be $NiCl_2.6H_2O$. X-ray diffraction has recently been used on one-dimensional pits of austenitic stainless steels and Fe to show $FeCl_2.4H_2O$ salt layers [7]. Diffraction patterns were also able to show anisotropy, indicating a texture under some corrosion conditions [6, 69]. At the corrosion interface, $FeCl_2.2H_2O$ has been observed in 304L and 316L stainless steels [12] indicating a reduction in access to water.

2.3.3. Current Voltage Characteristic

Figure 2-4 shows a typical current-voltage characteristic diagram for a one-dimensional pit that has been pre-grown, i.e. is of a sufficient pit depth to make hemispherical diffusion at the pit mouth negligible [70]. Starting at point *A*, the potential is increased at a constant rate. The region between *A* and *C* is under ohmic control, i.e. current response is proportional to the potential applied to the system. The solution at the pit interface continues to get more saturated as corrosion continues and will eventually get supersaturated. At point *C* the supersaturated solution reaches capacity and a salt layer precipitates out. This salt layer is resistive so current drops to nearly zero, as seen at point *D*. The precipitation of a large amount of salt from the supersaturation solution leaves the system out of equilibrium. The salt layer then thins as the system approaches equilibrium again. By point *E*, the system is at equilibrium and the limiting current, I_{lim}, has been reached. As the potential gradually increase, no change in current is observed. The system is under "diffusion control" here, and any increase in applied current will be absorbed by a thickening of the salt layer.

When the potential sweep is reversed from point *E* and lowered gradually, current remains constant at I_{lim}. While the potential decreases, the salt layer thins. At point *F*, applied potential has become so low that the salt layer can no longer be maintained and it dissolves fully. This point is known as the Transition Potential, E_T, and marks the transition between diffusion controlled and activation controlled dissolution. As potential sweeps down to point *G*, the current decreases until passivation.

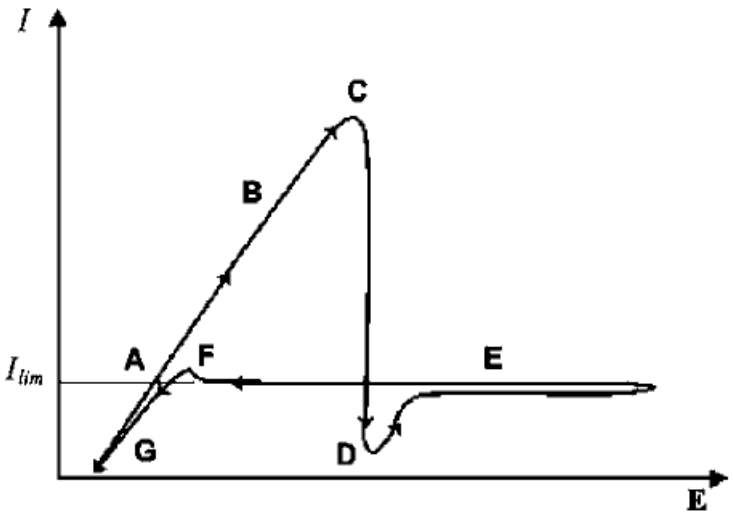

Figure 2-4 Current-Voltage characteristic of a one-dimensional artificial pit of a pre-grown pit. Applied potential increases [70].

2.3.4. Tafel slope

The Tafel slope is a measurement that relates anodic dissolution kinetics to the overpotential (i.e. the difference between the applied potential and the reversible potential of a reaction). In one-dimensional pitting, the Tafel slope is measured when corrosion is under activation control. Laycock and Newman [13], using Beck and Alkire's [47] and Galvele's [27] observations, proposed a model using voltage balance to calculate IR drop across the corroding interface:

$$E_{app} = E_{cor} + b_a log\left(\frac{i_a}{i_{corr}}\right) + \phi_s + \phi_{sf} \qquad \textit{Equation 2-14}$$

Where E_{app} is applied potential, E_{corr} is corrosion potential, b_a is the anodic Tafel slope, i_a is the anodic current density, i_{corr} is the open circuit corrosion current density, φ_s is *IR*-drop across solution and φ_{sf} is the *IR*-drop across the salt film. This relationship can be used for both salt covered and salt free corrosion interfaces.

Anodic dissolution kinetics in near-saturation conditions at the corrosion interface have been investigated by Newman and Isaacs [71], using *IR*-corrected potential to find the Tafel slope. In austenitic stainless steel (19-10 alloy) the Tafel slope was measured to be 60 mV/decade when above -300 mV (vs SCE) and 75 mV/decade when below -300 mV. This led to the suggestion that there may be a change in speciation at lower potentials. Other authors have found a range of Tafel values on stainless steels. Gaudet *et al.* [72] measured a value of 54 mV/decade on 304L stainless steel in supersaturated solution. Enerhaug *et al.* measured 57 mV/decade on martensitic steel [73]. However, some results have shown Tafel values of over 100 mV/decade. Steinsmo and Isaacs [74] measured a Tafel slope of 108 mV/decade on Ferritic stainless steel in supersaturated solutions. Laycock and Newman [13] measured 110 mV/decade in 302 stainless steel in 1 M NaCl, but this cell may not have been fully *IR*-corrected as the *IR*-drop inside the pit was not calculated, only that of the bulk solution [12].

2.4. Passivation

Fe is generally considered a 'reactive metal', i.e. a metal that spontaneously reacts with oxygen or water in ordinary use [75]. James Keir [76] showed that the treatment of iron with nitric acid prevented the precipitation of silver from silver nitrate while maintaining a shiny surface. Reactive metals, such as Fe, do not however revert to their ore-like state immediately after casting because of kinetic barriers that are formed during the process of 'passivation'.

Fontana [21] defines passivity as "the loss of chemical reactivity under certain environmental conditions". Passivity in stainless steels can be observed

electrochemically using a current-voltage characteristic plot (Figure 2-5). As the potential is increased from E_{corr}, the dissolution rate increases with an ohmic relationship in the 'active' region. Active dissolution under potentials above E_{corr} occurs without the presence of a salt film on the corroding surface. Once the Primary Passivation Potential, E_{pass}, is reached, current drops dramatically and further increase in potential after this point does not correspond to an increase in current. This indicates the formation of a surface film that impedes the dissolution of underlying metal. This is largely attributed to the formation of adsorbed hydrated complexes of metals, which then react with water to allow the formation of a stable layer [77]. Increasing potential further into the 'transpassive' region drives the

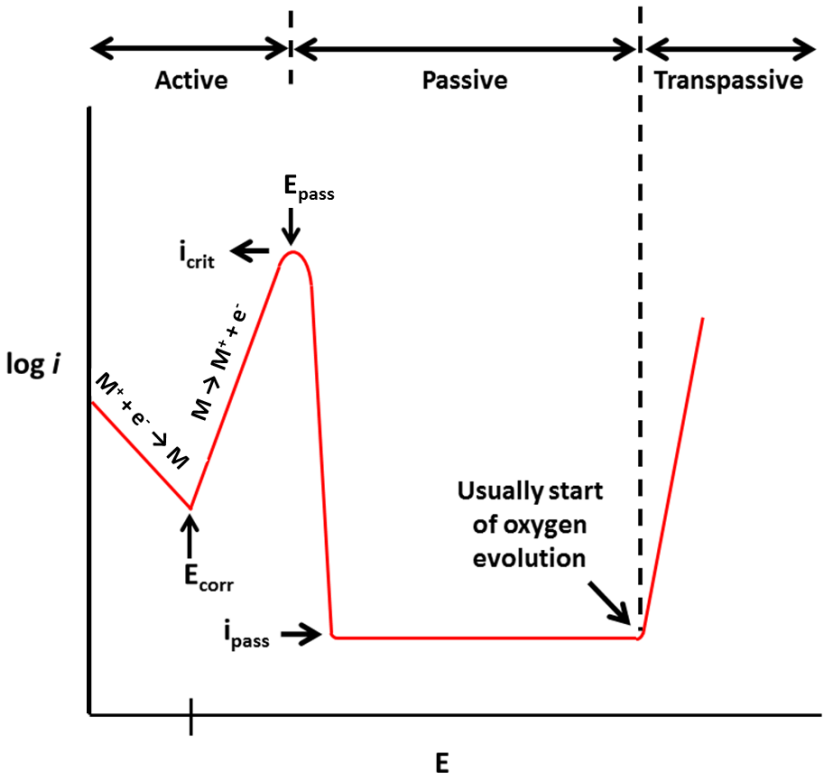

Figure 2-5 Schematic diagram of anodic dissolution of a Cr-rich Fe alloy. E_{pass}= primary passivation potential, E_{corr}=corrosion potential, i_{crit}= critical current density, i_{pass}=passive current density.

system to return to an approximately linear response in current. This accelerated dissolution is not necessarily due to pitting but most commonly due to the start of new anodic processes [18].

Repassivation of pits is crucial in determining the sustainability of pitting. Pourbaix *et al.* [78] conducted a series of experiments on stainless steels in chloride solutions and described it as the potential below which pitting current drops below passive current level. Wilde and Williams [45] showed that in 304 stainless steel neither passivation nor repassivation potentials are material properties and are in fact dependent on environmental and solution conditions.

The concept of repassivation potential was first described by Pourbaix *et al.* as a "protection tension" [78], which was developed by Starr *et al.*[79] suggesting protection may result from a repassivation of an active surface. Here it was determined to be the potential where, once potential was increased, no significant current increase was observed. This has been adopted as a standard definition of E_{rp} [80]. Other definitions include the start of cathodic current on the pitting surface [11] or then the current density drops below an arbitrary threshold current density value [81, 82], which is in fact the definition used in Pourbaix diagrams[83]. When potentiodynamic sweeps are used on bulk electrodes, such as wires, some authors define E_{rp} as the point where the reverse sweep crosses the forward sweep, completing a "hysteresis loop" [84]. The selection of the criteria for the definition of E_{rp} does not necessarily depend on the transition between two competing regimes of corrosion, as at high concentrations repassivation is a much less distinct value and

ohmic response to variation in potential is observed until very low current densities [57].

Solution concentration has a strong effect on repassivation. Yashiro and Tanno [85] observed that pitting potential, $E_{p,}$ and repassivation potential, E_{rp}, decreased linearly with logarithmic increase of NaCl concentration between the range of 0.1 and 3 M in 304L stainless steels. Anderko *et al.* [81] verified these results by showing E_{rp} decreased linearly with logarithmic increase of chloride activity up to saturation, though with two distinct trends: a much steeper decrease occurred at lower concentrations than at higher concentrations. Okada [86] developed a model for repassivation of a pit, where local islands of oxide appear as the potential approached E_{rp}. This oxidation reduces local dissolution, propagating the passive layer as potential decreases.

2.4.1. Role of nitrate on steels

Nitrate is known to prevent corrosion on stainless steels by acting as a strong passivating agent [87, 88]. John Keir described the range of effects of nitrate on steel over 200 years ago, showing that concentrated nitric acid protects steels from corrosion but dilute acid exacerbates corrosion significantly [76, 89]. Lillard *et al*. have also shown that passive layers form more quickly and are thinner in higher nitrate concentrations [90].

When trace nitrate is added to chloride solutions a passivation potential is observed, E_{pass}, above which a corroding surface will passivate [91-94]. A correlation has been observed between E_{pass} and chloride:nitrate ratio, with increasing nitrate concentration resulting in reduced E_{pass} [92, 95].

Just before E_{pass}, current oscillations and fluctuations have been observed [14, 96, 97]. This has been seen as a clue as to the mechanism that operates in passivating stainless steel surfaces in chloride/nitrate solutions. Several theories have been proposed to account for these oscillations:

1. A nitrate-rich salt layer may be formed, with oscillations resulting from competing salt species being formed [14]. This salt may occur as a molten salt, as seen in corrosion of iron in concentrated $NaNO_3$ solutions under high potentials [98, 99], and as such the reduced porosity my increase the resistivity of these salts.
2. A competitive adsorption, as proposed by Leckie and Uhlig [92], between chloride and nitrate ions on the corroding surface. This model accounts for the induction time required as competitive adsorption is kinetically limited. This theory is informed by a literature proposing models of protons being cyclically repelled and attracted to the corrosion surface [100], altering local pH and generating oscillations in current.
3. Nitrate reduction models that consume H^+ ions at the corroding surface and raise pH causing passivation [14, 96, 97]. Evans suggested that the reduction of nitric acid was auto-catalytic [101] on steel and showed this by augmenting nitrite content in nitrate solutions. Increasing nitrite concentration in these nitrate solutions increased cathodic current density, indicating reduction reactions. Autocatalytic reaction sequences were later suggested [102] that involved the reduction of nitrate *via* adsorption to the pit surface (Vetter's mechanism) [58] and in solution near the corroding surface (Schmid's mechanism) [58]. The electroreduction of NH^+ to NO_3^- as a

possible route that has been put forward [103] but no direct evidence for this has been observed in the corrosion of austenitic stainless steels [104].

Carbon steel in nitrate/nitrite solutions is known to evolve bubbles which have been hypothesised to be N_2, suggesting reduction processes [105]. Temperature has also been observed to influence oscillation behaviour, with higher temperatures reducing their occurrence [106].

2.4.2. Role of molybdenum in stainless steel

Empirical studies of the influence of Mo in pitting resistance of stainless steel led to the development of pitting resistance equivalence numbers (PREN) that rank the resistance of steels to pitting corrosion. An example formula [19] is:

$$PREN = Cr\% + 3.3\,Mo\% + 16N\% \qquad \textit{Equation 2-15}$$

Although the influence of Mo in preventing pitting is clearly quantifiable, the exact mechanism that causes this improvement is under debate. Three major theories have emerged.

1. *Mo enriches the surface of the alloy preventing initiation and passive film breakdown*

The oxide has order at the nanostructure level [26] that can be interpreted to be significant in pitting initiation. Mo has been observed using time-of-flight SIMS to be enriched in the passive layer during polarisation of Fe-17Cr-14.5Ni-2.3Mo alloy, existing mostly as Mo(IV) before polarisation and becoming enriched up to 16% of cations in the Mo(VI) state after polarisation[107].

2. *Mo reduces dissolution rate, preventing pits from becoming stable during the propagation phase.*

The theory of enrichment of corroding surfaces with Mo is well established [108]. Newman found that on scratched surfaces of ferritic Fe-18.6%Cr stainless steel the addition of 2.5 wt% Mo reduced the dissolution rate in the active region, but only had a small effect on the passivation potential if passivation was indeed possible [109]. Newman [110] surmised enrichment mainly occurred at the kink/step sites due to the small surface coverage of Mo. The suggestion that the potential needed to generate a salt layer may be higher was also made. Using 1D pits, Newman [110] showed that the anodic dissolution rate of austenitic stainless steels was 5-10 times lower under active (i.e. salt-free) dissolution in alloys when 1.6wt% Mo was added.

3. *Mo causes polymeric networks near the dissolving interface, interrupting diffusion kinetics within the pit solution.*

Kimura *et al*.[111] observed spectra from corroding Mo in chloride solutions using X-ray absorption spectroscopy. From these results they suggested that they resembled results similar to Na_2MoO_4, and suggested a complex matrix of molybdate species could form in the solution near the corrosion interface, preventing ion diffusion and retarding corrosion rates when alloyed with stainless steel. However Davenport *et al*.[112] used synchrotron-based X-ray absorption spectroscopy near the corroding interface of 316L stainless steel to identify Mo(III) species in solution, with no evidence of Mo(VI) polymolybdates.

2.5. Atmospheric Pitting Corrosion

Whilst corrosion often occurs in full immersion conditions, it is possible for situations to occur where small amounts of solution are present on metal surfaces.

These solutions can have trace amounts of salt in them, creating conductive electrolytes that promote corrosion. The restricted volume of the electrolyte in these cases often results in highly concentrated solutions forming, causing localised corrosion. This is known as atmospheric pitting corrosion.

2.5.1.Salt deposition

Salt is often found on the surfaces of structures, particularly if they have been through any form of transit or period of storage outdoors [2]. The majority of salt that acts as catalyst for atmospheric corrosion arrives on the surface of the metal in one of two ways:

1. As an aerosol, e.g. from ocean waves crashing or other such nebulising activity, which deposit on the metal surfaces as solid particles of salt.

2. By being in a splash zone, where dilute saline solutions (e.g. sea water) are splashed onto metal surfaces.

In both cases, maintaining an aggressive solution to allow corrosion to occur relies on the property of salts known as deliquescence

2.5.2.Deliquescence

'Deliquescence' is the process that a hygroscopic salt undergoes of drawing in moisture from the atmosphere to keep equilibrium between the water activities of the solution and the surrounding atmosphere [113]. When humid air is present in a system with salt, an equilibrium in water activities will be reached between these two phases [114]. Salt will draw in moisture if the atmosphere's relative humidity (RH)

is higher that the salts Deliquescence Humidity (DH), and will expel moisture if RH is below DH. Losing moisture is known as 'effluorescence'.

Each salt species has a unique DH [5]. The deliquescence humidity is sensitive to temperature as it is a thermodynamic process. A consequence of maintaining equilibrium in water activities between the atmosphere and the solution is that small volumes of solution will have their concentration controlled by the humidity of the atmosphere. A solution that is in an atmosphere with an RH that is equal to its salt's DH will be, by definition, saturated.

Tsutsumi *et al*. showed 304L stainless steel is vulnerable to atmospheric corrosion when exposed to humidities of less than 65% RH, which is equivalent to approx. 3 M $MgCl_2$ [114]. While "dry" conditions are generally considered to be resistant to corrosion, Schildelholz *et al*. [113, 115] have shown that corrosion can occur on Fe at humidities well below RH for NaCl, $MgCl_2$ and artificial sea water salt crystals.

2.5.3. Evans Droplet Model

Corrosion of Fe was investigated by Evans by depositing droplets of NaCl with a phenolphthalein/potassium ferrocyanide addition as pH indicators [116, 117]. Evans showed that as corrosion propagated a distinct high-pH region occurred around the edge of the droplet and a low-pH region occurred towards the centre where the metal dissolution occurred (Figure 2-6). This preferential location of corrosion was determined to be the consequence of "differential aeration", i.e. a concentration gradient of oxygen in solution [118]. This gradient drives oxygen reduction, the main cathodic reaction, to occur at the edges of the droplet where the easiest supply of oxygen is, leaving the centre prone to metal dissolution. Chen and Mansfeld [119]

showed using a Kelvin probe cathodic potentials around the edge of NaCl droplet on steel, supporting this model.

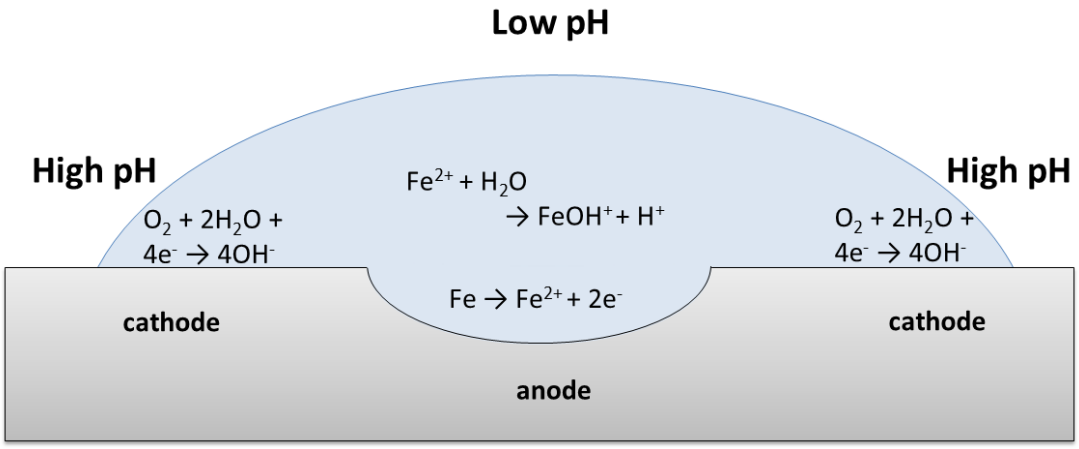

Figure 2-6 Schematic diagram showing reactions occurring in the Evans Droplet Model. The anodic and cathodic regions are spatially distinct, with cathode at the edge of the droplet. Differences in pH are caused by reactions stated.

This behaviour has also been observed in Zn alloys under droplets of salty water [120], with corrosion occurring towards the centre of the droplet, which has been modelled by controlling oxygen diffusion as the dominant reduction reaction [121]. Aluminium dissolution under droplets does not appear to conform to the Evans droplet model as no preferential site is observed [122, 123] . However, when pure DI water was deposited on AA2011 trenching was observed around Cu-rich inclusions around the droplet edge, indicating an alkaline region and thus oxygen reduction, that was not observed near the centre [124].

Stainless steel has not been observed to follow the Evans model, with pitting occurring without noticeable trend when under droplets of $MgCl_2$ [125, 126]. This has been attributed to the very stable passive layer present on stainless steels. Other

alloys, such as Fe and Zn [127], have much less stable passive layers so corrosion is able to migrate as conditions change, which was observed by Evans on Fe [116]. Some investigations using wire beam electrodes have noted that in some conditions corrosion of both Fe and 304L stainless steel can occur towards the edge of droplets [128, 129] if droplets are sufficiently large at deposition.

2.5.4. Secondary spreading of droplets

A common occurrence in atmospheric corrosion under droplets is secondary spreading of droplets during corrosion. Secondary spreading is usually a solution layer on the order of monolayers thick and has been observed to participate in corrosion electrochemistry, increasing the cathodic area [119]. The salt species used can heavily influence secondary spreading. NaCl has been shown to promote the secondary spreading of droplets [121, 130], while $MgCl_2$ solutions did not spread. This was suggested to be due to insoluble $Mg(OH)_2$ pinning the boundary of the droplet.

Micro-droplets have been observed to form around deposited droplets during corrosion [131], with external polarisation of droplets has been observed to increase the expansion of secondary spreading and the formation of "micro-droplets" [130]. This result was confirmed on carbon steel and stainless steel using bi-plate samples[132].

Micro-droplets have also been shown to appear above anodic attack, with "filiform-like" corrosion occurring under $MgCl_2$ micro-droplets on 304L [133] and hemispherical pitting on AA7075 [134]. There is evidence that these micro-droplets are caused by anodic dissolution, as the ejection of metal ions into solution has been observed to cause droplets under thin films of solution [135].

2.5.5. Laboratory simulation

2.5.5.1. Laboratory salt deposition

Using droplets of dilute saline solutions is a common method of depositing of salt onto a sample surface, and deposition is usually by micropipette or syringe [114, 136]. Droplets are useful because geometries are often very well defined, making it easy to isolate influences on anodic and cathodic regions. It is also easy to calculate Chloride Deposition Density (CDD), which is the mass of chloride over area, usually written in units of $\mu g/cm^2$ [2, 137]. CDD is an industry standard used to quantify the amount of salt found on structures, so using droplets allows direct comparisons to practical experience.

Using droplets also presents challenges. The deposition of dilute solutions does not necessarily reflect the "deliquescence" processes that occur in practice, where solid salt draws in moisture from the atmosphere and its liquid phase starts at saturation. Other techniques have been attempted to investigate this, such as inkjet printing of salt onto metal surfaces [138-140] or the direct deposition of fine salt particles [141, 142] . High pressure N_2 gas has been used to atomise salt and deposit on metal surfaces through a cascade impactor [143], as has using ethanol as a medium to deposit salt has also been used [144, 145].

2.5.5.2. Electrochemical measurements of atmospheric corrosion

Electrochemical measurements of atmospheric corrosion are technically challenging due to the restricted volume of solution available. The Kelvin Probe (KP) is a non-contact technique pioneered by Stratmann *et al.*[146-148] initially used to investigate Fe and Fe-Cu systems. The vibrating probe is held above the sample and local

potentials can be measured, with anodic and cathodic sites along the surface able to be isolated spatially. Chen and Mansfeld [119] first used a KP to show cathodic regions on steel can extend to outside the droplet perimeter. Neufeld *et al.* [120] also showed this secondary spreading on Zn and monitored its spread over time noting an increasing participation in cathodic current. Tsuru *et al.* [130] used KP to show that micro-droplets that occur in the secondary spread region adjacent to droplets provide cathodic current with the main droplet being anodic.

Other techniques have also been used to investigate the onset of corrosion though they do not possess the ability to isolate anodic sites on the metal surface. Co-planar electrodes connected across a zero-resistance ammeter that allow the moment current begins to flow between the plates to be seen [132, 149, 150]. This has been extended to use 2D arrays of wire to construct wire-beam electrodes [128, 151] to try to collect data on different positions under droplets of solution.

Nam *et al*. [125] used a Ag-wire electrode across the surface of droplets of $MgCl_2$ on 304 and 430 stainless steels to show the effect of humidity on initiation and repassivation. By holding a Ag-wire across a droplet and connecting it and the sample plate to a two-electrode potentiostat, the range where pitting occurred was able to be isolated. On 304 it was shown to be 47-58% RH at 298K, and 48%-68% on 430. Repassivation occurred at higher RH, i.e. lower solution concentration, with 304 repassivating between 56%-70% RH and 430 between 67%-73% RH at 298K

2.5.6. Morphology of pits

The shape of pits in corrosion varies depending on the conditions they are generated under. Pits grown in full immersion conditions under applied potentials often require

occlusion to propagate. Schwenk [91] observed hemispherical pits in the initial stages of growth covered with a porous layer that acted as a diffusion barrier, though these pits sometimes showed faceting if initiated away from the edge of grain boundaries. They then developed into hemispherical shapes and lost their faceted appearance [152]. These porous layers, sometimes described as “lacy covers” [153], were also found in dilute chloride solutions described as Lacy pit covers on stainless steels [153-155] and Fe [156].

Pit morphology is influenced by microstructure, with orientation of inclusions and other phases, such as δ-ferrite bands, affecting propagation in stainless steels [157]. Solution concentration has been seen to affect pit mouth size and modelling has confirmed the influence of solution concentration on repassivation kinetics [8, 158]. Applied potential can also influence pit morphology, with higher potentials often giving smoother pitting surfaces [17, 159]. Sato [160, 161] observed crystallographic etching in pitting of Fe when at low applied potential that smoothed out then potential was increase, and attributed this to the development of a critical concentration inside the pit.

Pits that have grown in atmospheric conditions, and that have developed at OCP, have shown different morphologies than those grown under applied potential. Maier and Frankel [136] showed that pitting of 304L under droplets of $MgCl_2$ often had shallow dish regions, developed by a process called “earing” due to the ear-shaped morphology observed in the early stages of attack. This observation was also reported by Hastuty *et al* [162] on 430SS. The shallow dish regions are interesting in that they are broadly unoccluded. Cruz *et al.* [150] observed “colonies” of smaller pits around a large, flat region of attack. Mi *et al*. [139] saw that the size of these pits

grew with increasing droplet surface area, indicating a cathodically limited attack [163].

2.6. Synchrotron Sources

2.6.1. What is a synchrotron?

A synchrotron is an electron accelerator that is used as a very high quality X-ray source, providing both excellent flux and consistency compared to normal laboratory sources [164] (Figure 2-7).

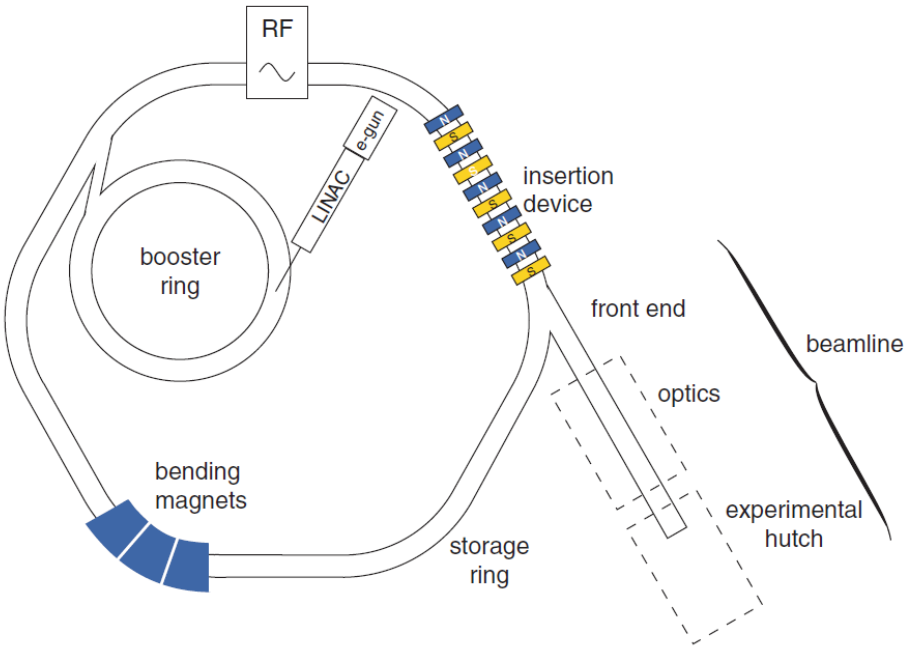

Figure 2-7 Schematic diagram of a third-generation synchrotron [164].

Electrons are generated in a vacuum at an "electron gun" using a process known as "thermiomic emission"[165] that applies an anodic voltage across a cathodic heater, propelling electrons in the synchrotron. Electrons are then fed into a Linear Accelerator (LinAc) to an energy of ~100 MeV. The electrons then enter a booster ring where they are further accelerated before entering the storage ring.

The storage ring is not a "ring" but a polygon that uses bending magnets to deflect the electrons. The storage ring is designed to have a constant current, and is topped up from the boosting periodically as electrons are lost by use or hitting residual gas in the vacuum. Electrons are accessed by "insertion devices" that are used to generate X-rays.

Insertion devices have arrays of magnets lined up with opposite poles. As the electrons move passed these arrays of magnets, they begin to "wiggle" and give off energy in the form of X-radiation as they continually change direction. As the electrons are travelling at relativistic speeds, causes the radiation to be directed forwards, creating an X-ray beam of high flux, brightness (intensity per unit area of source) and spectral brightness (intensity per unit area per unit solid angle per unit energy bandwidth).

The beam that comes out of the insertion device is known as "pink beam" as it has a wide range of wavelengths. It is possible to refine and select the wavelength of the radiation in the "optics" hutch, before experimental use, by using a monochromator. Monochromators use two [166] or four [167] Si (111) crystals to select energy by serial diffraction. By aligning the crystal at specific angles, it is possible to select a single wavelength of radiation by using Bragg's law [168].

2.6.2.X-ray Diffraction on corrosion systems

X-ray diffraction allows the identification of crystalline phases by their diffraction patterns. Crystalline structures are arranged in such a way that their atoms form sheets or layers with fixed spacing. When X-rays interact with these layers, they give

constructive interference and diffract in discrete patterns, which are determined by Bragg's law:

$$n_i\lambda = 2dsin\theta \qquad \textit{Equation 2-16}$$

Where n_i is any integer, λ is the radiation wavelength, d is the layer spacing, and θ is the angle of incidence.

Most salt layers are crystalline (some are molten), and synchrotron X-ray diffraction has been used to observe these salts *in situ*. Rayment *et al*. [7] has used artificial pits of Fe and 316L in 1 M HCl to show a $FeCl_2.4H_2O$ salt exists during dissolution. Information was also able to be found about the morphology of the salt crystals in the pit, with 316L showing significantly more spottiness in the collected diffraction pattern indicating a coarsening of crystal size. Xu [6, 69] also use a similar technique to compare salt layers of Fe in NaCl with and without nitrate additions, finding that nitrate increases anisotropy of salt crystals. Other groups have investigated salt layers on copper [169] and scale in carbon steels [170].

2.6.3. Radiography

X-ray Radiography can be used to view changes in morphology *in situ*. The X-ray beam can pass through a sample and be attenuated, i.e. lose flux due to absorption or deflection. The amount of flux lost due to attenuation is usually quantified in terms of a ratio of the original beam:

$$\frac{Int}{Int_0} = \exp(-\mu x_t) \qquad \textit{Equation 2-17}$$

Where *Int* is the transmitted beam intensity, Int_0 is the original beam intensity, μ is the absorption coefficient of the material and x_t is the thickness of the material. The

transmitted beam hits a detector, either an undeveloped film or a fluorescent screen in more modern instances, and produces a two-dimensional image.

In its raw state, this image may not accurately represent the experiment as it contains distortions due to changes in the beam (flat field) and heterogeneities in the detector (dark field). Radiographs are typically corrected after collection by subtracting any contribution of the dark field and dividing through any contribution of the white field. The flat field is usually an average of several images of the x-ray beam without a sample present.

$$corrected\ data = \frac{transmitted\ data - dark\ field}{flat\ field - dark\ field} \qquad \textit{Equation 2-18}$$

Radiography has been used to investigate the growth of artificial pits *in situ*, with Ghahari *et al*.[8, 10, 171] investigating the dissolution kinetics of 304L to inform their kinetics model. Hammons *et al.* [172] has also used the technique on Ni to characterise consistency in the dissolution of the interface during corrosion.

2.6.4. Effect of X-radiation on electrochemical data

Xu [58] has previous addressed the paucity of work done on the influence of a high flux of radiation on corrosion processes. Nagy and You [173] have reported on the extent of radiolysis found in *in situ* synchrotron experiments involving solutions. Radiolysis will always occur, with the generation of H_2 and H_2O_2 as a consequence. Particular concern is in cells with narrow geometries, as most radiolysed solution will stay at the working interface. The effect is broadly mitigated by attenuating the radiation beam by use of Al filters [7].

3. Experimental procedures

3.1. Materials used

304L and 316L stainless steels were obtained from Goodfellow, Aperam, and Advent. Details are shown in Table 3-1.

Table 3-1 Alloys used in this body of work

Material	Form	Supplier	Thickness	Processing	Composition (wt%)	Experiments
304L	Foil	Goodfellow	25 μm and 50 μm	Annealed	Cr-18%, Ni 10%, C <300 ppm , Fe balance	Synchrotron XRD and radiography
	Sheet	Aperam	3 mm	Cold-rolled, solution annealed at 1040-1100 °C then air cooled	Cr 18-19.5%, Ni 8-10.5%, Mn 2%, S 0.015% max N 0.1% Max, C 0.03% max, P 0.045% max, Fe balance	Atmospheric droplets exp morphology and position, full immersion plate, Ag wire experiment
	Wire	Advent	50 μm	Temper annealed	Cr 17-20%, Ni 8-11%, C<300 ppm, Fe balance	1D pitting
	Wire	Advent	125 μm	Temper Annealed	Cr 17-20%, Ni 8-11%, C<300 ppm, Fe balance	Wire experiments
316L	Wire	Advent	50 μm	Temper annealed	Cr 17-20%, Ni 8-11%, Mn 2% max, C<300 ppm, Fe Balance	1D pitting
	Wire	Advent	125 μm	Temper annealed	Cr 17-20%, Ni 8-11%, Mn 2% max, C<300 ppm, Fe Balance	Wire Experiments

3.1.1 SEM and EDS characterisation of alloys

Plate steel supplied for these droplet tests was electro-arc melted then continuous casted, cold-rolled and annealed. SEM analysis of 304L plate stainless steel is shown in Figure 3-1, where the plate has been mirror polished using OP-S (Struers) for 10 min, leaving a slightly etched surface. The plate is almost entirely populated with equiaxed grains, with a distribution of annealing twins throughout the surface. Sheet steel would be expected to have elongated grain structure as it goes through rolling processes after casting [19], but the foundry note supplied with this plate steel showed that it had been annealed after rolling at 1040 - 1100 °C, allowing recrystallisation of the grains and producing an equiaxed grain structure of austenite.

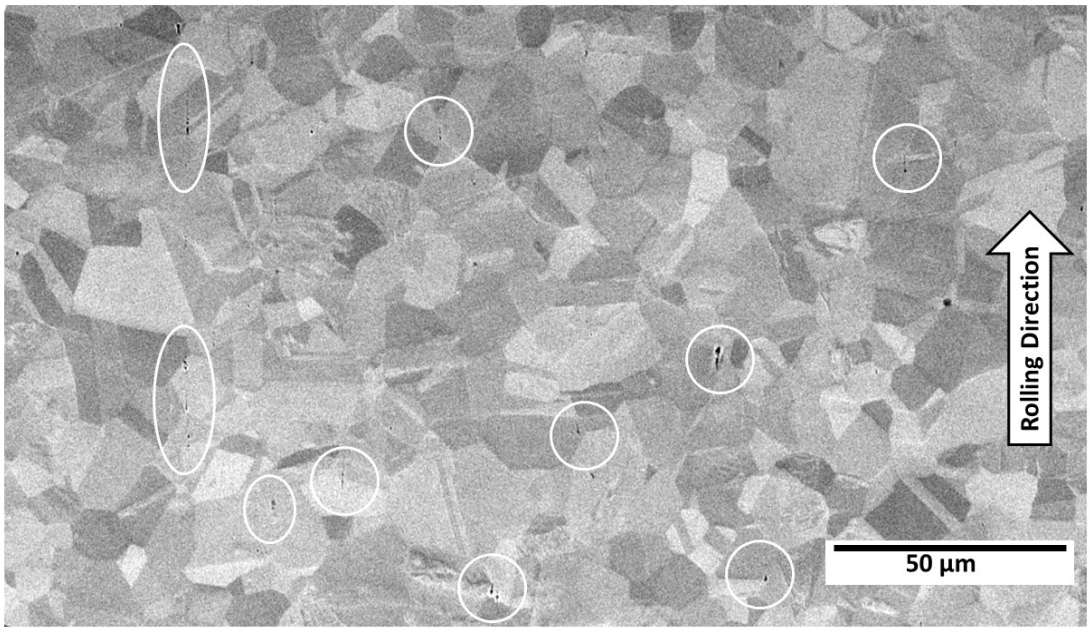

Figure 3-1 Secondary electron Scanning Electron Microscope image of mirror polished 304L plate stainless steel on the longitudinal surface. Surface polished with OP-S 0.04 µm colloidal suspension (Struers) for 10 minutes. Metallography shows equiaxed grains with annealing twins throughout the microstructure. Surface-breaking inclusions (circled) can be observed as stringers elongated along the rolling direction.

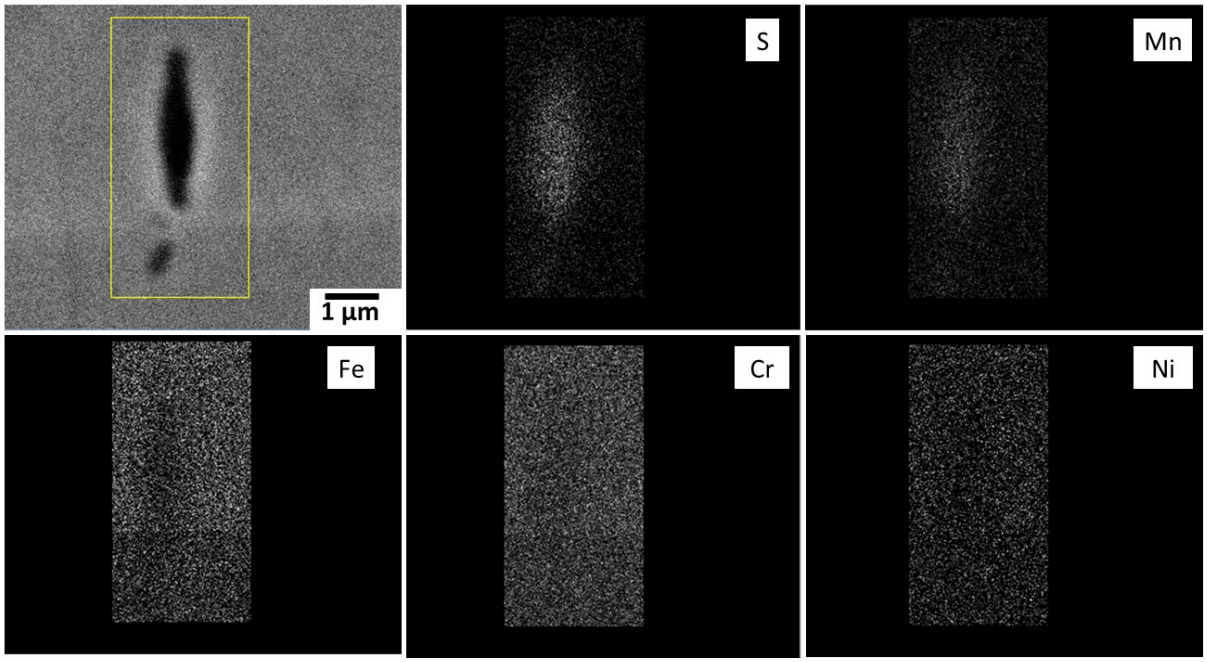

Figure 3-2 Energy Dispersive X-ray Spectroscopy of a surface-breaking inclusion on 304L stainless steel plate. Inclusion shows enrichment of S and Mn.

Table 3-2 Foundry specifications of 304L plate used in atmospheric corrosion experiments and EDS of plate alloy used. EDS of 304L and 316l wires used in electrochemistry experiments also shown

Element (wt %)	**Fe**	**Ni**	**Cr**	**Mn**	**S**	**C**	**Si**	**N**	**P**	**Mo**
304L Plate - Foundry spec. (max)	Bal	8-10.5	18-19.5	2	0.015	0.03	0.75	0.1	0.045	-
304L Plate - Foundry analysis	Bal	8	18.1	1.46	0.0033	0.023	0.44	0.072	0.032	-
304L Plate - EDS (3 point scan avg)	Bal	7.5	18.8	1.6	-	-	0.47	-	-	-
304L wire - EDS (3 point scan avg)	Bal	9.8	19.8	0.7	-	-	0.46	-	-	-
316L wire - EDS (3 point scan avg)	Bal	10.5	17.9	1.6	-	-	0.23	-	-	1.6

EDS analysis of these inclusions (Figure 3-2) showed that these were rich in Mn and S. The composition of the plate alloy can be seen in Table 3-2. Composition of 304L and 316L wires used in electrochemistry are also shown in Table 3-2.

3.2. Salt solutions

$NaCl + NaNO_3$ and $MgCl_2$ solutions were used in these experiments. For synchrotron experiments, 1 M $NaCl + NaNO_3$ solutions were used, where $NaNO_3$ concentration ranged between 0 and 75 mM. For atmospheric corrosion experiments using droplets, $MgCl_2$ concentrations ranging from 0.03 M to 5 M were used. For full immersion experiments, $MgCl_2$ solution concentrations ranging from 1 M to 5 M $MgCl_2$ were used. All $MgCl_2$ solutions were made using $MgCl_2.6H_2O$ (Sigma Aldrich or Fisher Scientific) and deionised water (Millipore, >15 MΩ cm). NaCl solutions were made using NaCl (Sigma Aldrich), $NaNO_3$ (Sigma Aldrich) and deionised water (Millipore, >15 MΩ cm).

3.3. Synchrotron Experiments

3.3.1. Synchrotron sample preparation

The same 2D foil samples were constructed for synchrotron XRD and radiography experiments, as described by Rayment *et al*.[7]. Approx. 3 mm wide strips of 50 μm thick (for XRD) and 25 μm thick (for radiography) 304L stainless steel (Goodfellow) was cut and degreased in methanol for 15 minutes before air-drying. These foils were then embedded in Araldite epoxy resin (3M). Once dry, the foil was cut in two and the freshly cut surface became the pit mouth and was attached to a reservoir using Kapton tape (3M) (Figure 3-3).

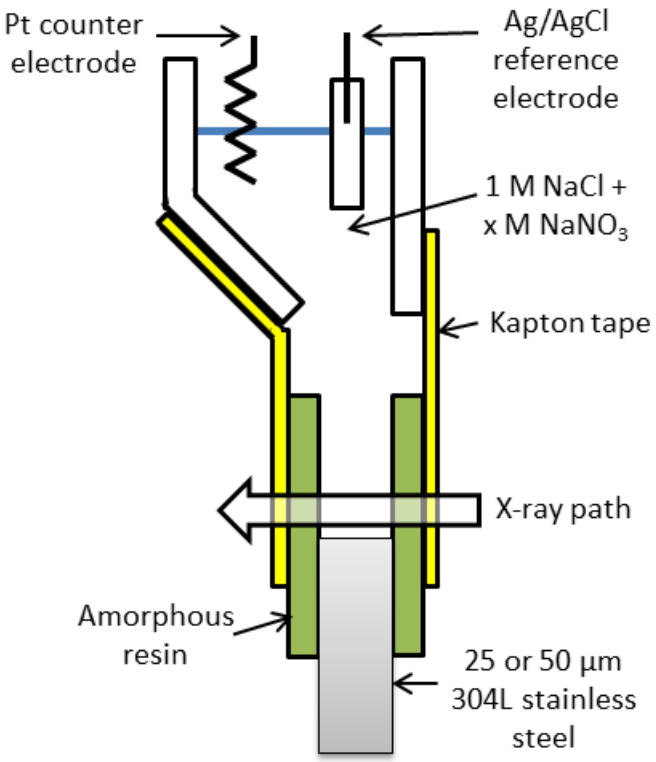

Figure 3-3 Schematic diagram of foil cells used in synchrotron experiments. 50 µm and 25 µm thick foils were used in XRD and radiography experiments respectively [56]

3.3.2.Synchrotron XRD experiments

The cell reservoir was filled with 20 ml of 1 M NaCl, then connected to a Ag/AgCl reference electrode and a Pt counter electrode (all potentials are quoted on the Ag/AgCl scale). The pit was held at 1 V for 6 hours to grow a pit of approx. 1 mm deep. This allowed sufficient depth to allow one-dimensional diffusion. All electrochemistry was controlled by an Ivium Compactstat potentiostat.

XRD experiments were conducted *in situ* using the microfocus spectroscopy beamline I18 at the Diamond Light Source [174]. The X-ray beam had a spot size of 2.5 µm (h) x 20 µm (w) and beam energy of 12.00 keV. Image resolution of the scans had a pixel size of 26 µm x 26 µm using a CCD detector. Beam damage [173] was reduced by the use of a 0.75 mm Al-foil to reduce the intensity of the incoming

beam. Scan time was limited to 15 seconds to also limit beam damage. The sample was positioned below the incident beam so the initial scans were in the solution above the corrosion front and salt layer. The sample was then raised in 2 μm increments, with a pattern collected at each increment until only austenitic stainless steel pattern was observed, as shown in Figure 3-4. Three sweeps, from bulk solution through the salt layer into the metal, were conducted for each solution used. X-ray diffraction patterns were analysed and integrated using XRDUA [175].

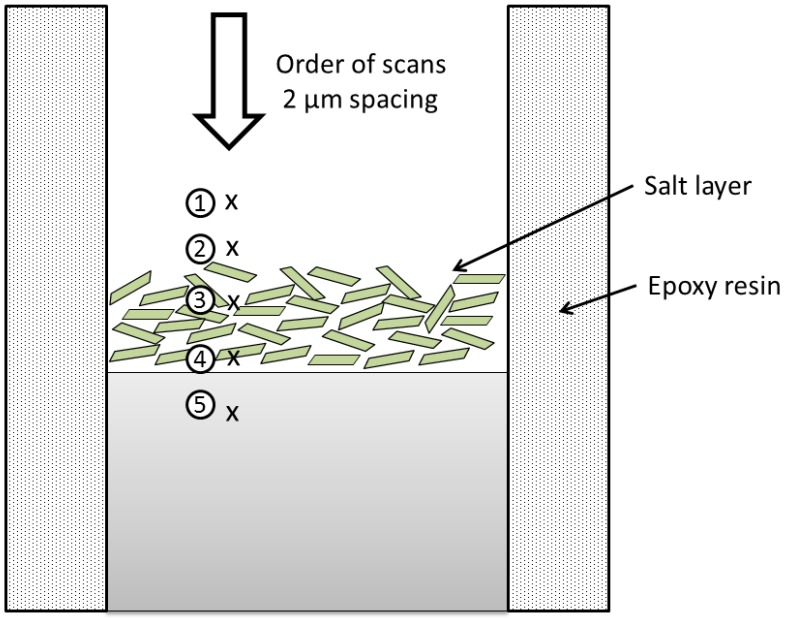

Figure 3-4 Schematic diagram of XRD diffraction collection therough the salt layer of a one-dimensional pit. Numbers indicate order or scans [56].

The pit was held at potentials from 0.3 V to 0.7 V, as summarised in Table 3-3. The cell solution composition was then changed to 40 mM $NaNO_3$/1 M NaCl, 50 mM $NaNO_3$/1 M NaCl, then finally up to 75 mM $NaNO_3$/1 M NaCl at the potentials shown in Table 3-3. The current was observed during each experiment to ensure the pit did not passivate.

Table 3-3 Solution conditions of XRD scans on 304L and potential that each scan was held under [56].

$NaNO_3$ concentration in 1 M NaCl (mM)	Applied Voltage (V, Ag/AgCl)					
	0.3	0.4	0.5	0.55	0.6	0.7
0	X	X	X		X	X
40			X		X	X
50	X	X	X	X		
75	X	X	X			

3.3.3.Synchrotron Radiography experiments

Radiography experiments were conducted *in situ* at the Diamond-Manchester imaging branchline I13-2 at Diamond Light Source [176]. Cells were made with the same procedure as in the diffraction experiments, but with 25 μm thick foils of 304L (Goodfellow). The X-ray beam was produced using an undulator insertion device and the full X-ray energy undulator spectrum, known as pink beam, was used. The beam was attenuated using a combination of 0.2 mm pyrolytic graphite and 2.2 mm of aluminium filters before impinging on the sample. This gave an energy spectrum of a series of discrete intensity peaks comprising photon energies from 15.0 to 25.0 keV. The undulator gap was adjusted to values ranging from 8 to 10 mm to vary the photon flux.

An optical microscope system made using Mitutoyo optics collected the visible light produced by the X-ray beam impinging on a 150-μm-thick scintillating $CdWO_4$ crystal and high-speed CMOS PCO Dimax HS camera (2016 x 2026 pixels). The camera chip pixel size of 11 μm x11 μm combined with a 10x optical magnification gave an effective pixel size of 1.1 μm. The total field of view was ~ 2.2 x 2.2 mm. A radiograph was collected approximately every 1.1 s. Radiation exposure time was limited to 40 ms to reduce beam damage, which was controlled by a fast shutter. 30

dark field and 30 flat field images were taken before each set of scans and used to correct images for beam and detector fluctuations. Data was analysed using DAWN 1.6 program package [177].

The pits were grown in 20 ml of 1 M NaCl in a back lab away from the X-ray exposure for approximately 1 hour to generate a pit of depth 700 μm, ensuring one-dimensional diffusion. The cell was placed in the beam nitrate solution was added to the reservoir to make up a solution concentration of 75 mM $NaNO_3$/1 M NaCl. Potential was held at 0.4 V for 1800 s to allow time for nitrate solution to diffuse through the cell, as preliminary experiments showed that 1800 s was sufficient to time for nitrate additions to diffuse to the bottom of the pit and passivate the corroding surface. The potential of the cell was then increased by 50 mV increments and held for 600 s at each potential until passivation was observed.

3.4. Atmospheric corrosion droplet experiments

3.4.1. Sample preparation

304L plate of 3 mm thickness was used (Aperam, France). The plate was cut into 75 mm x 25 mm samples and ground using 800 grit SiC paper (Struers), and cleaned in deionised water in an ultrasonic bath for 15 minutes. Samples were then rinsed with DI water and cold-air dried and left in a covered container for 24 hours before droplet deposition.

3.4.2. Atmospheric Experiments

When investigating the effect of changes in relative humidity, 2 μl droplets of 0.27 M $MgCl_2$ were deposited, giving a CDD of approx. 750 $\mu g/cm^2$. When investigating the influence of CDD, droplets of 0.03 M and 3 M $MgCl_2$ were also deposited giving a CDD of 80 and 5400 $\mu g/cm^2$. Droplets were deposited with a Multiprobe II liquid

handling system (Perkin-Elmer Life Sciences) at 5 mm intervals, in arrays of 4 x 14 or 4 x 15 (56-60 droplets) with a deposit rate of 10 µl/s (Figure 3-5). Each solution array was deposited within 8 minutes. Temperature at deposition was between 20-23 °C with a humidity of 25-44 %RH during deposition. The experimental conditions used are reported in Table 3-4.

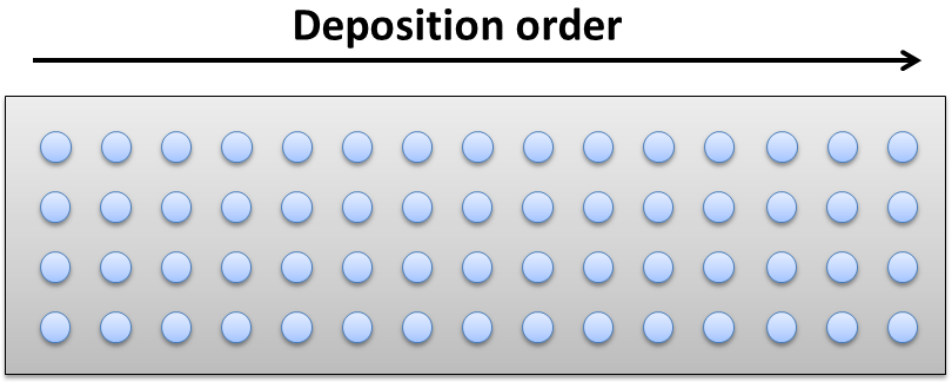

Figure 3-5 Schematic of atmospheric corrosion plates with 2 µl droplets deposited in 4 x 15 array. Droplets are deposited in rows. Entire plate is deposited within 8 minutes.

Table 3-4 Chloride deposition density (CDD) for as-deposited droplets of $MgCl_2$ deposited on 304L stainless steel plate. Samples sizes are 56-60, with standard deviation given for data set in each case. Droplets deposited at 20-23 °C in ambient relative humidity (25-44 %RH). Samples were put into controlled experimental humidity within 8 minutes of first deposition [126].

Humidity ± S.D. (%RH)	**Average Droplet CDD ± S.D. (µg/cm^2)**			**Droplet area on deposition (cm^2)**		
	"80"	**"750"**	**"5400"**	**"80"**	**"750"**	**"5400"**
33±2	80±3	670±40	5400±300	0.048±0.001	0.057±0.003	0.051±0.001
38±2	-	820±20	-	-	0.047±0.001	-
43±2	-	790±40	-	-	0.048±0.002	-
48±2	-	670±40	-	-	0.057±0.003	-
56±2	-	730±40	-	-	0.052±0.002	-

After deposition, the plates were held in an ECO135 atmospheric chamber (TAS Ltd) at 30±1 °C and at a controlled humidity between 33-56% ±2 RH for 24 hours [114] . After 24 hours optical images were collected for each droplet using a microscope. The plate was washed with DI and methanol.

3.4.3. Time-lapse experiments

Samples of 304L stainless steel for time-lapse experiments were prepared as above. 2 µl droplets of 0.5 M $MgCl_2$ were deposited in a sealed container with relative humidity controlled by saturated salt solution. The container was heated externally to 30±3 °C and held under a microscope. Once pitting was observed to have started the magnification was increased and images were taken once a minute.

3.4.4. Droplet Ag wire experiments

Electrochemistry experiments were conducted using Ag wire electrodes following the method of Nam *et al*. [125]. Ag wire of 50 µm diameter was suspended above a 304L stainless steel plate that was prepared as described above Figure 3-6. The wire was clamped and held under tension on top of PTFE tape to separate it approximately 40 µm above the sample surface. 4 wires were held across the sample to test different concentrations.

The sample was then placed in an atmospheric chamber (ECO135, TAS Ltd) and held at 30 ± 1 °C and 33 ± 2 %RH. The Ag wire was connected to a two-electrode Compactstat potentiostat (Ivium), with the sample acting as the working electrode with a time resolution of 1 s. A droplet of 1 M $MgCl_2$ was deposited on the sample, touching one wire. This was repeated with 2 M, 3 M, and 4 M $MgCl_2$ on separate wires.

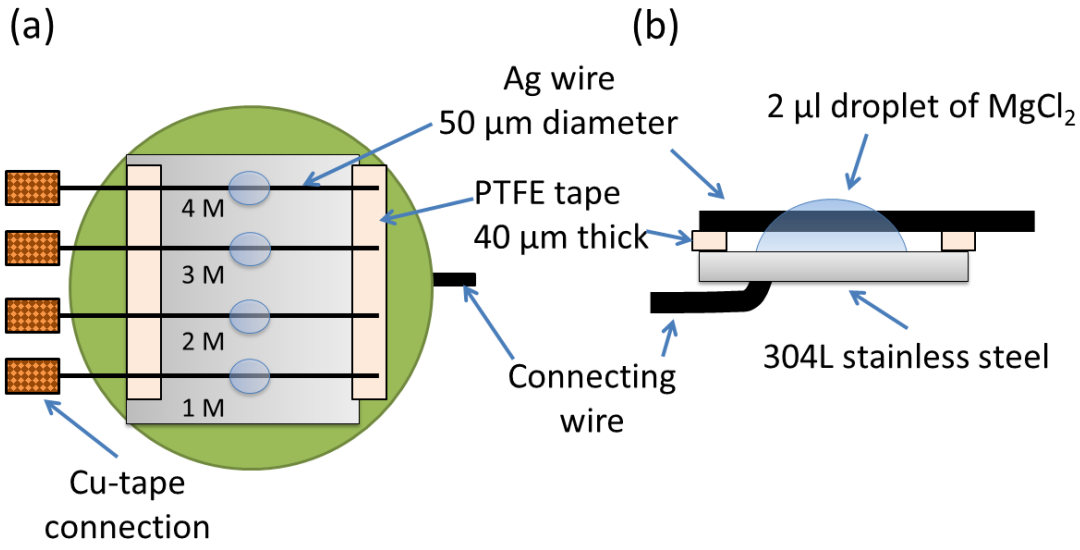

Figure 3-6 Ag Wire cell used to detect corrosion initiation under droplets of $MgCl_2$. a) 2 µl Droplets of $MgCl_2$ with concentrations indicated were deposited on 304L stainless steel at 30 °C in 33% RH atmospheric inside an atmospheric chamber. Droplets were deposited and measured using a Compactstat potentiostat. b) Ag wire suspended approx. 40 µm above sample by being clamped under tension on PTFE tape.

Unanodised Ag wire was used for these experiments. As discussed by Nam *et al.* (12), the AgCl film generated by anodising dissolves after a short time in concentrated $MgCl_2$ solutions, creating variation in readings over time. Unanodised Ag is more controlled in these conditions. One must recognise, however, that the potentials measured as not a true potential as E_{Ag}, i.e. the potential at the silver interface, does change with solution concentration during the experiment.

3.5. One-dimensional pitting experiments

3.5.1. Sample preparation

One-dimensional artificial pits were prepared using wires (Figure 3-7). 304L and 316L wires (50 µm diameter, Advent) were degreased in methanol then attached to electrical wire with copper tape to ensure a strong electrical connection. The

connection was then wrapped with PTFE tape (RS components) and enclosed in a heat-shrunk tube. The stainless steel wire was then placed inside an acrylic tube (6 mm outer diameter, Alternative plastics Ltd. UK) with the base of the tube sealed with PTFE tape. EpoFix (Struers), an epoxy resin, was mixed and poured into the tube and left to cure for at least 24 hours. The top of the tube was then ground with 800 grit SiC paper when used.

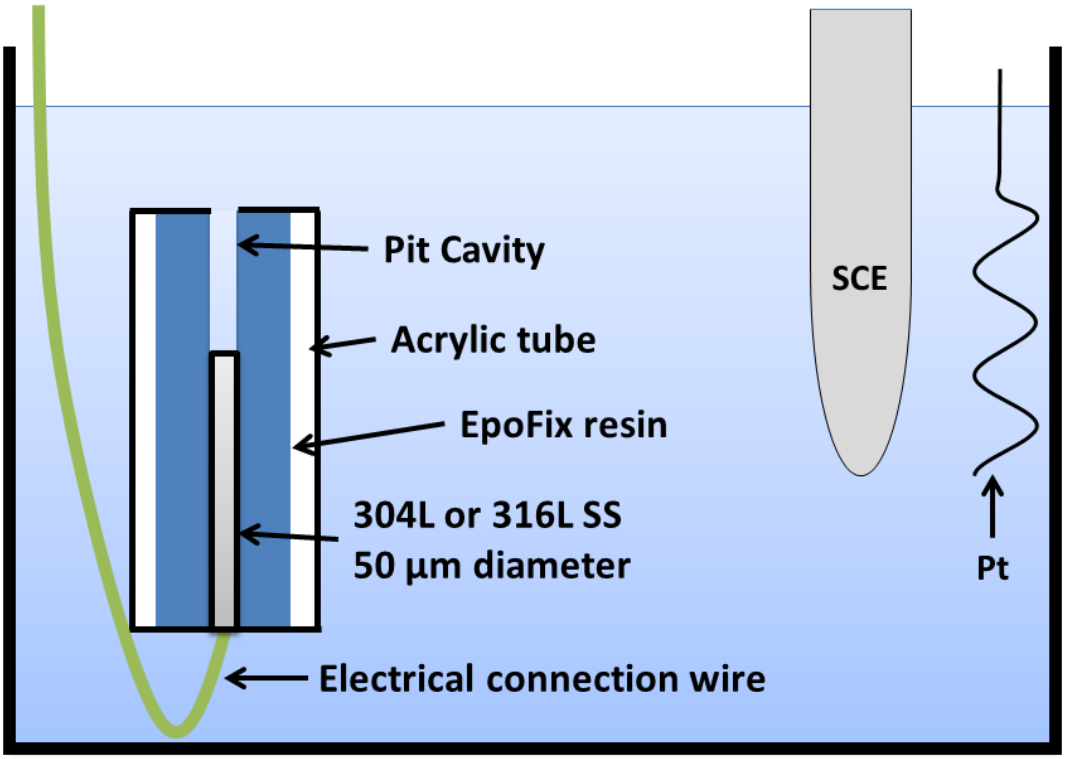

Figure 3-7 Schematic diagram of One Dimensional artificial pit used in zig-zag experiments

3.5.2. Electrochemical measurements

3.5.3. Zig-zag pitting

1D artificial pits were immersed in approx. 200 ml of solutions of between 1 – 4 M $MgCl_2$ with pits held vertically. The potential program applied to the pits is shown in Figure 3-8 was controlled by an Ivium CompactStat potentiostat. Saturated Calomel Electrode (SCE) was used with a Pt counter electrode. Potential was started at 1.2 V

and swept down to 0.04 V at a rate of 5 mV/s to grow the pit to a depth that allows one-dimensional diffusion. Then the potential was swept up 20 mV and down 30 mV at 0.2 mV/s until -0.4 V or passivation occurred. 5 mV perturbations were applied during sweeps to allow use of Electrochemical impedance spectroscopy (EIS) analysis and record solution resistance.

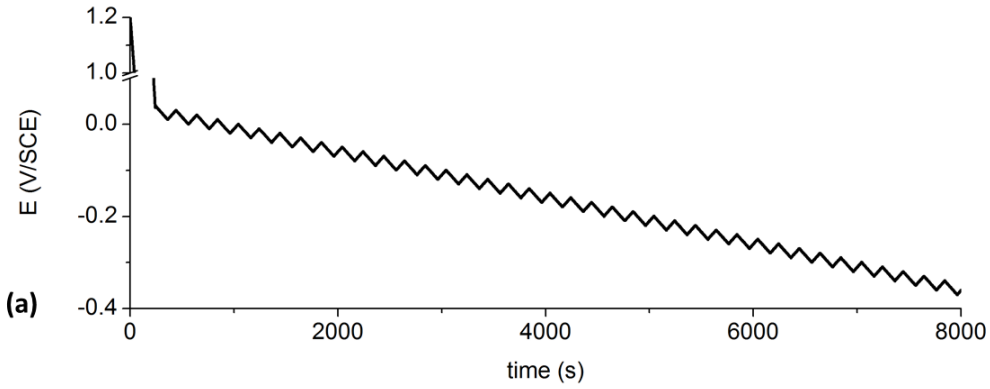

Figure 3-8 Potential difference program applied to one-dimensional pits in zig-zag pattern to allow the isolation of E_T and E_{rp} values.

3.6. Wire experiments

Wires of 304L and 316L (125 µm diameter, Advent) were ground with 1200 grit SiC paper and washed with DI water and methanol. Wires were cut to approximately 10 cm in length and photographed with a scale. Wires were then connected to an Ivium CompactStat potentiostat with a SCE reference electrode and Pt counter electrode. The wires were immersed in solutions of between 1- 5 M $MgCl_2$ were made and held at -100 mV below OCP for 15 minutes. A photo was taken to observe how much of the wire was immersed. Care was taken to ensure the cut edges of the wires were not immersed. The potential was then swept up at 5 mV/s until current reached 1 mA (the onset of pitting) then swept back until into the cathodic region. Current density was then calculated. Ambient temperature was 23±2 °.

3.7. Full immersion plate experiment

304L plate was cut to 25 x25 mm square. An electrical cable was attached to the back of the plate by copper tape (Figure 3-9). Epoxy resin (EpoFix, Struers) was then poured on to the plate and left to cure for 24 hours. It was then ground with 800 grit SiC paper and cleaned with DI water. The plate was then immersed in either 1 M or 4 M $MgCl_2$ and held at -100 mV for 15 minutes using an Ivium CompactStat potentiostat. Potential was then swept forwards at 5 mV/s. Once pitting was observed, potential was swept back until cathodic current was generated.

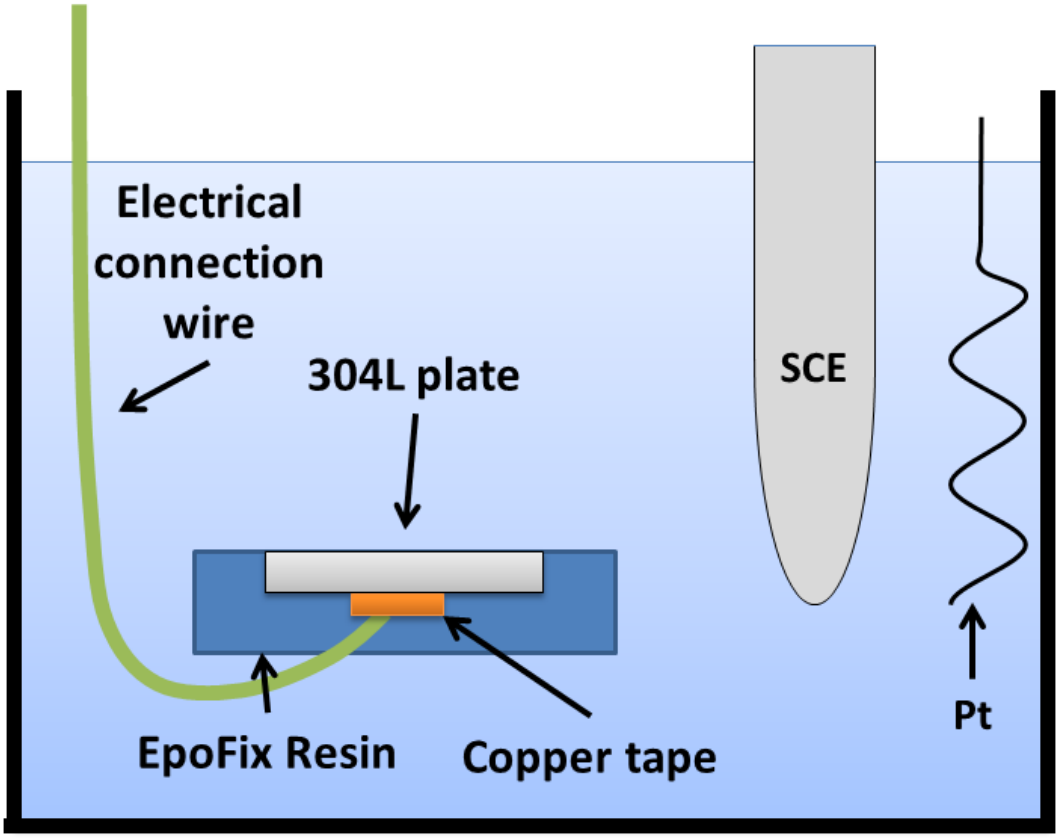

Figure 3-9 Schematic diagram of 304L plate used in full immersion experiments. Plate was set in EpoFix with an electrical connection attached to the back.

4. Effect of nitrate on the salt layers in artificial pitting corrosion of 304L stainless steel

4.1. Introduction

The dual nature of nitrate on steels has been observed for over two centuries, with concentrated nitrate solutions passivating steel surfaces but dilute nitrate solutions exacerbating corrosion [75]. Investigations into the passivating effect of nitrate in chloride solutions have shown the presence of passivation potentials, E_{pass}, above which corroding sites are passivated [14]. Particular attention has been paid to the influence of NO_3^-:Cl^- ratio on the intensity of E_{pass}, with increasing nitrate moving E_{pass} to less noble values. At potentials just below the E_{pass}, current oscillations occur [6, 14].

The nature of the salt layer that forms in nitrate/chloride solutions has been under discussion. It has been suggested that current oscillations may arise from competition between chloride salts and nitrate-rich salts [94]. Amorphous molten salts have also been observed in concentrated nitrate solutions on Fe [98] which may cause heterogeneity in current.

This chapter aims to investigate the species and nature of the salt layer in one-dimensional pits of 304L stainless steel when corroding in NaCl solutions with trace amounts of $NaNO_3$. Synchrotron-based XRD and radiography will be used to correlate electrochemistry, salt layer species, and dissolution kinetics to develop a mechanism for current oscillations.

4.2. Results

4.2.1. Electrochemistry

Cyclic voltammograms typical of an artificial pit in 304L stainless steel are shown in Figure 4-1. Pits were initially grown in 1 M NaCl at 1 V (Ag/AgCl), then maintained at a potential of 1.2 V until a stable salt layer had been formed. Figure 4-1a shows a potentiodynamic sweep starting at 1.2 V and decreasing at 2 mV/s. As the applied potential decreases, the current remains constant as the salt layer thickness, and its resistance, reduces to regulate the surface interfacial potential. These diffusion-limited conditions continue until point (B) where the salt layer is lost. This coincides with a slight increase in current as this resistive layer dissolves away. After this, there is an ohmic relationship between current and voltage until the end of the sweep at -0.1 V (C). The forward sweep, at 2 mV/s, showed an approximately ohmic relationship initially, but was not exactly linear and did show a curve in its plot as potential increased. This may be due to the slow sweep rate up, allowing diffusion away from the corrosion interface and thus extending the time needed to saturate. In this region (D), the pit was able to achieve a current much higher than the diffusion limited current due to the supersaturation of the solution above the salt layer, approximately 2 times higher than when at diffusion limited current. Once the solution has been supersaturated, the salt layer precipitates and settles on the surface, dramatically reduces the current (E). This supersaturated solution precipitates a particularly thick salt layer, as seen elsewhere [72], but this rapidly reaches an equilibrium with the interfacial solution and diffusion limited current is maintained until the end of the sweep (F). The current at this point is slightly lower than at the beginning of the sweep at (A) due to the deepening of the

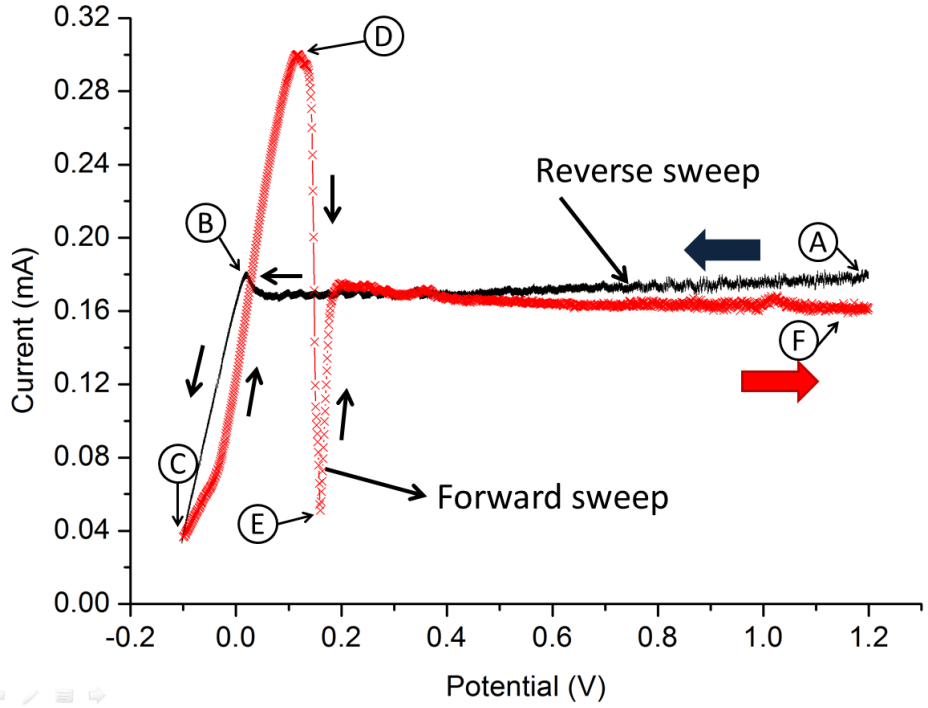

(a)

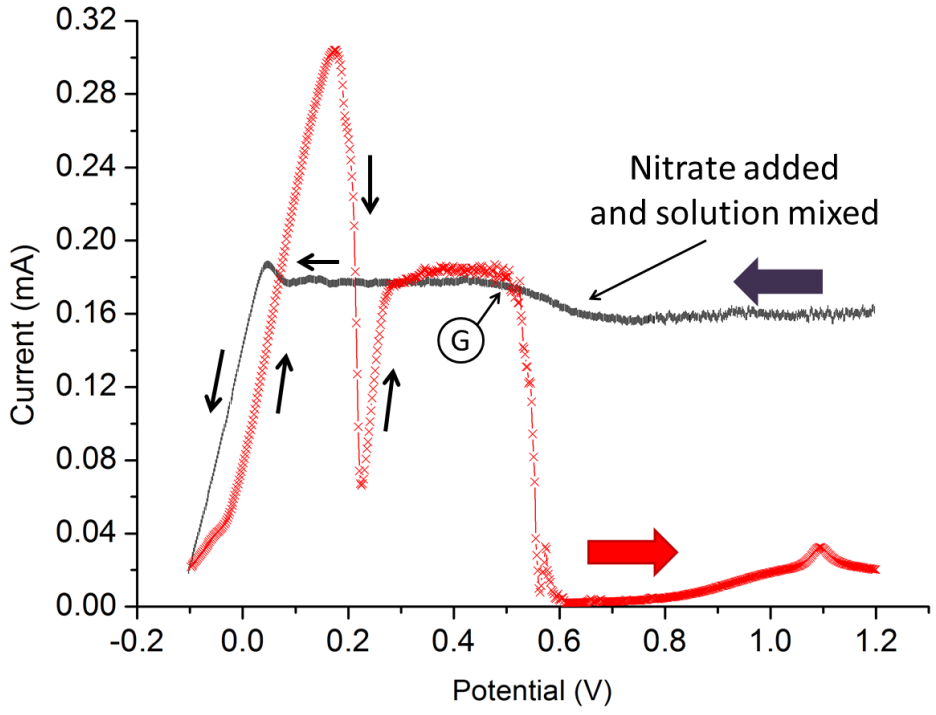

(b)

Figure 4-1 (a) current in 304L artificial pit when potential is swept from 1.2 V to -0.1 V at 2 mV/s in 1 M NaCl, (b) sweep repeated in same cell after solution changed to 75mM $NaNO_3$ + 1 M NaCl [56].

pit increasing diffusion pathway length and therefore increasing the IR drop of the solution. At the end of the potential sweep in Figure 4-1a, sodium nitrate ($NaNO_3$) was added to the solution and mixed in to give a final solution concentration of 75 mM $NaNO_3$ +1 M NaCl (Figure 4-1b). The reverse sweep looked very similar to that seen when no nitrate was present, i.e. a diffusion limited current until the salt layer was lost, resulting in a small bump in current followed by an ohmic relationship between current and applied potential. The forward sweep initially also looked similar, with the supersaturation of the solution at the interface resulting in a thick salt layer being precipitated, which then found equilibrium with the surrounding environment and diffusion limited current being maintained. However, at approximately 0.5 V (G) the current begins to reduce and drops rapidly until fully passivating by 0.6 V. These data are consistent with Figure 4 found in Newman and Ajjawi [14] for the same nitrate/chloride ratio.

Figure 4-2 shows a series of experiments in which the potential was held at 0.3 V, 0.4 V, and 0.5 V in 75 mM $NaNO_3$ + 1 M NaCl solution whilst simultaneously making XRD measurements on the salt layer that formed at the interface. Figure 4-2a shows that once the potential is applied the current quickly peaks and falls off, indicating the supersaturation of the interfacial solution and formation of the salt layer. Thus this gives a diffusion limited current of approximately 0.08 mA for the range of the experiment. At 0.4 V (Figure 4-2b) the initial supersaturation and precipitation of the salt layer is also seen. After approx. 400 s however, slight perturbations are observed in the current. At 0.5 V (Figure 4-2c) large current oscillations occur once the salt layer is formed. The oscillations appear to be of the

same scale as the limiting current with a period of between 80 - 100 s, continuing for the duration of the experiment (over 1200 s).

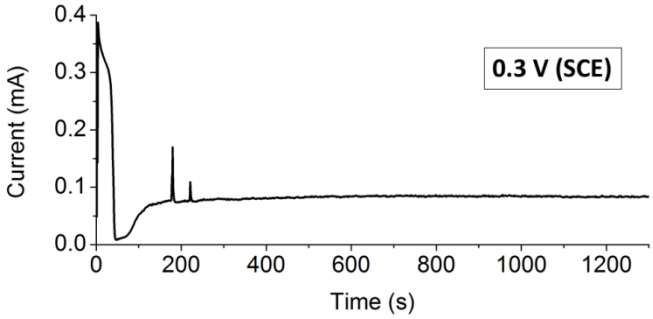

(a)

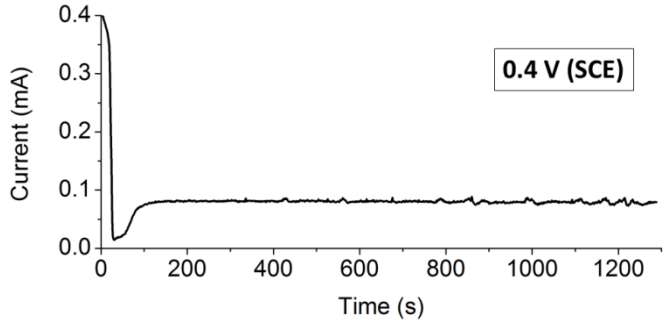

(b)

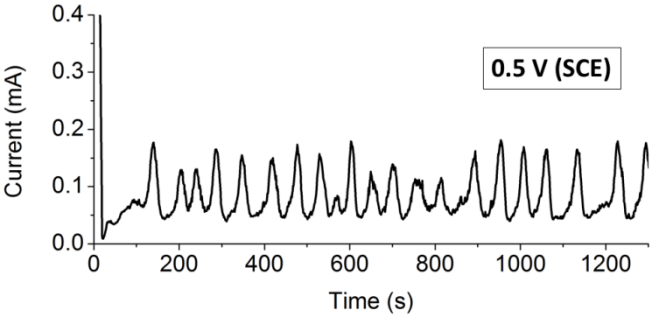

(c)

Figure 4-2 Current recorded in 304L one-dimensional pits in 75 mM $NaNO_3$ +1M NaCl at different potentials (a) 0.3 V, (b) 0.4 V, and (c) 0.5 V (Ag/AgCl) during XRD measurement of the salt layer.[56]

4.2.2.SEM Results

The electrochemical behaviour observed in 75 mM $NaNO_3$ + 1 M NaCl were reproduced away from the X-ray source in separate cells and SEM images were taken of their pitting surfaces. When the pit was grown for 4 hours in 1 M NaCl, the

corroded surface was consistently rough with the same texture covering the entire surface (Figure 4-3a). When a pit was grown in 75 mM $NaNO_3$ + 1 M NaCl and produced a current similar to that in Figure 4-2c, secondary pitting was observed on the pit surface (Figure 4-3b)

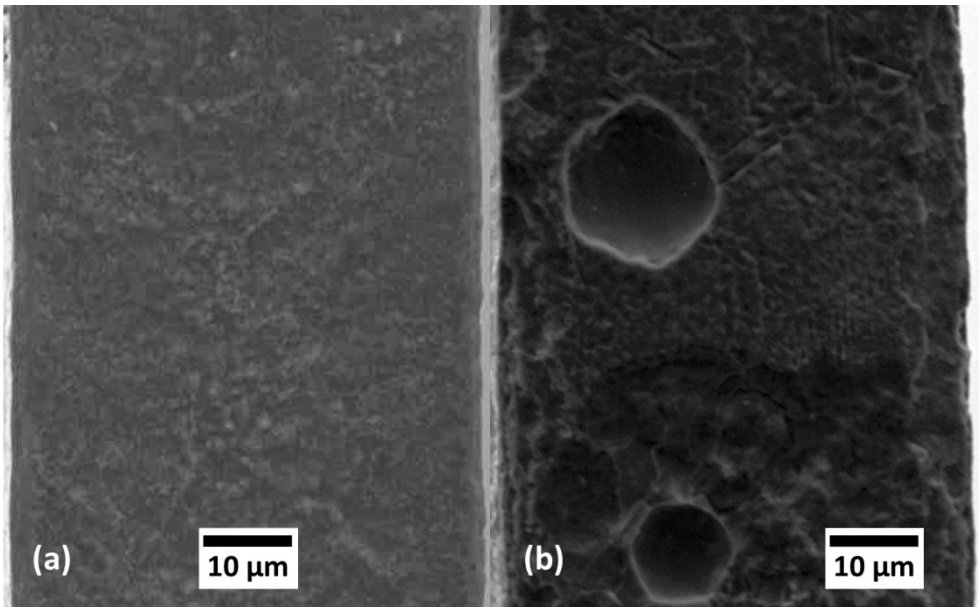

Figure 4-3 SEM of the corroded surface of 304 L stainless steel one-dimensional pits (a) after 4 hours in 1 M NaCl with no current oscillations, (b) after 4 Hours in 1 M NaCl then 4 hours in 75 mM $NaNO_3$ + 1 M NaCl after current oscillations were observed.[56]

4.2.3. Diffraction results

XRD patterns were taken of the salt layers generated during corrosion of 304L stainless steel one-dimensional pits in 1 M NaCl with varying concentrations of $NaNO_3$. Pits were made from 50 µm thick foils and results are shown in Figure 4-4. Regardless of nitrate concentration in solution or the electrochemical behaviour, the same diffraction peaks were observed (Figure 4-4a). All the peaks observed appear on the $FeCl_2.4H_2O$ diffraction pattern described by Verbist *et al.*[178] However, several minor peaks that are present in standard $FeCl_2.4H_2O$ patterns do not appear in these results, indicating a change in space group or symmetry. The intensity of

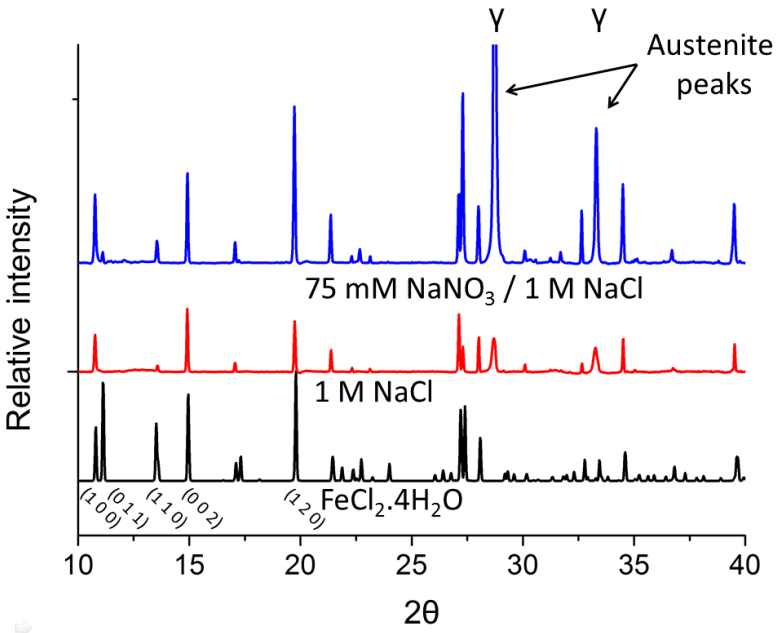

(a)

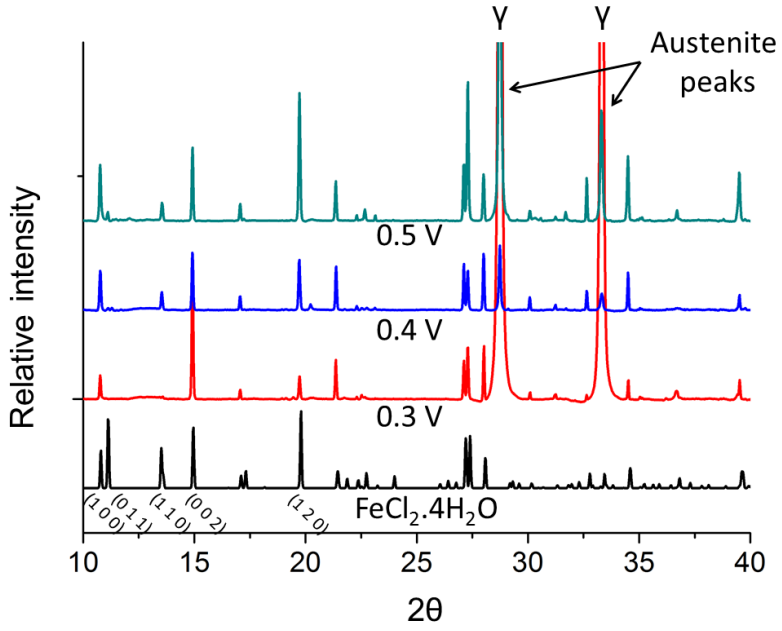

(b)

Figure 4-4 Diffraction patterns of salt layers in one-dimensional pits of 304 L (a) in 1 M NaCl at 0.5 V (Ag/AgCl) with varying $NaNO_3$ concentration, and (b) in 75 mM $NaNO_3$ + 1 M NaCl with varying applied potentials. The standard diffraction pattern for $FeCl_2.4H_2O$ also shown [56].

major peaks also differs from the standard, which may be a consequence of the limited amount of salt crystals participating in diffraction of X-rays over such a thin foil sample. No change was observed in diffraction pattern in nitrate-rich solutions,

indicating the salt species is not a nitrate salt. No change in salt species was observed in when the potential was increased in nitrate solutions between 0.3 V and 0.5 V despite significant differences in electrochemical behaviour (Figure 4-4b).

From Figure 4-3b it is clear that the size of the secondary pitting has a diameter significantly smaller than 50 μm (the thickness of the foil that is corroding). As such, we would be difficult to detect where these pits are occurring using diffraction as the pattern is summed over the entire thickness of the cell. This is also true of the electrochemical data, which is in practice the sum of current across the entire interface and cannot be easily used to discuss coexisting regimes. To interpret regimes that are subtly different other techniques, such as electrochemical impedance spectroscopy, could be used.

Although the salt species didn't change as a result of the nitrate concentration, there were noticeable changes in the intensity and completeness of the diffraction rings with increasing nitrate concentration. This indicates a change in crystallite size and morphology. Nitrate-free diffraction patterns showed anisotropy (Figure 4-5a), with the (100) ring having strongest pattern on the left- and right-sides of the ring and the (002) ring having strongest signal at the top and bottom of the ring. This is consistent with plate-like crystallites settling on the bottom of the pit with the (002) plane horizontal, producing a crystalline anisotropy. In nitrate-rich solutions (Figure 4-5b) there is much less anisotropy and the signal is spread more evenly around the rings. However, there are larger spots of intensity around the rings, indicating a coarsening of crystallite size. This is most pronounced in the (120) plane.

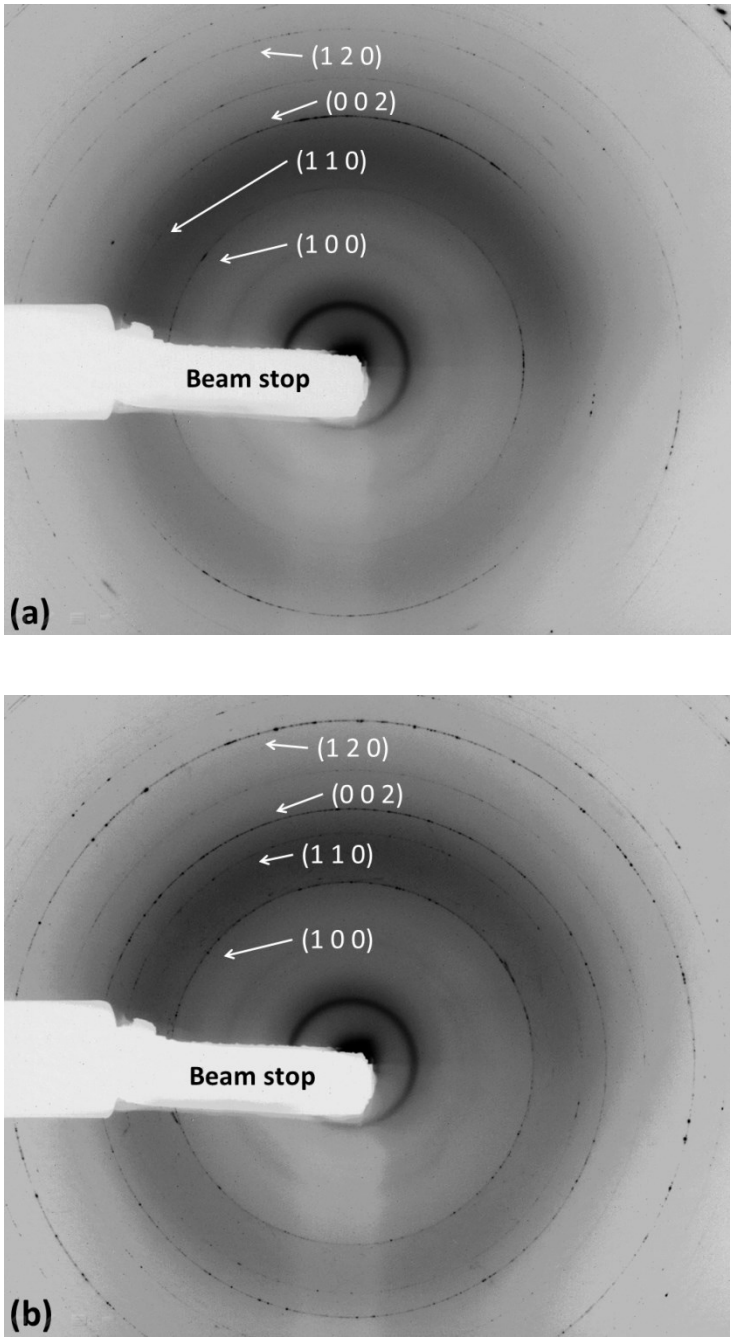

Figure 4-5 X-ray diffraction patterns of salt layer at 0.5 V (Ag/AgCl) in (a) 1 M NaCl with stable limiting current, and (b) 75 mM $NaNO_3$ + 1 M NaCl with oscillating current. Electrochemical data shown in Figure 4-2 [56].

4.2.4. Radiography results

Radiography results are shown in Figure 4-6, where a 25 μm thick foil is grown in 1 M NaCl for approximately 500 s before the solution is changed to 75 mM $NaNO_3$ + 1 M NaCl. The current was largely unchanged after the nitrate concentration

increase until 775 s (Figure 4-6a) when the current was seen to drop significantly. Radiographs were taken at 1 s intervals (Figure 4-6b). Edge detection was used to isolate the corrosion front which was plotted ever 100 s (Figure 4-6c), which showed fairly consistent material loss up until 800 s with only minor variations in speed of dissolution. After 800 s, the edges began to fall on top of each other, indicating passivation of the pit surface. The exception is the right-hand side of the pit, where a crevice initiates and continues to grow through the experiment. This coincides with a significant loss in current. Surges in current that occur after 900 s (Figure 4-6d) can be linked to bursts in dissolution that occur on the creviced site (Figure 4-6e). The elevated current observed on the downward sweep on Figure 4-1b may be a result of a crevice like this as the salt layer is lost. The voltage was held at 0.4 V for 1800 s, and then raised to 0.45 V where surges in current became more pronounced. When the potential was raised to 0.5 V current was reduced to zero and the pit surface was fully passivated. This passivation potential was significantly lower than that observed for diffractions (0.6V) which had a much thicker foil (50 μm).

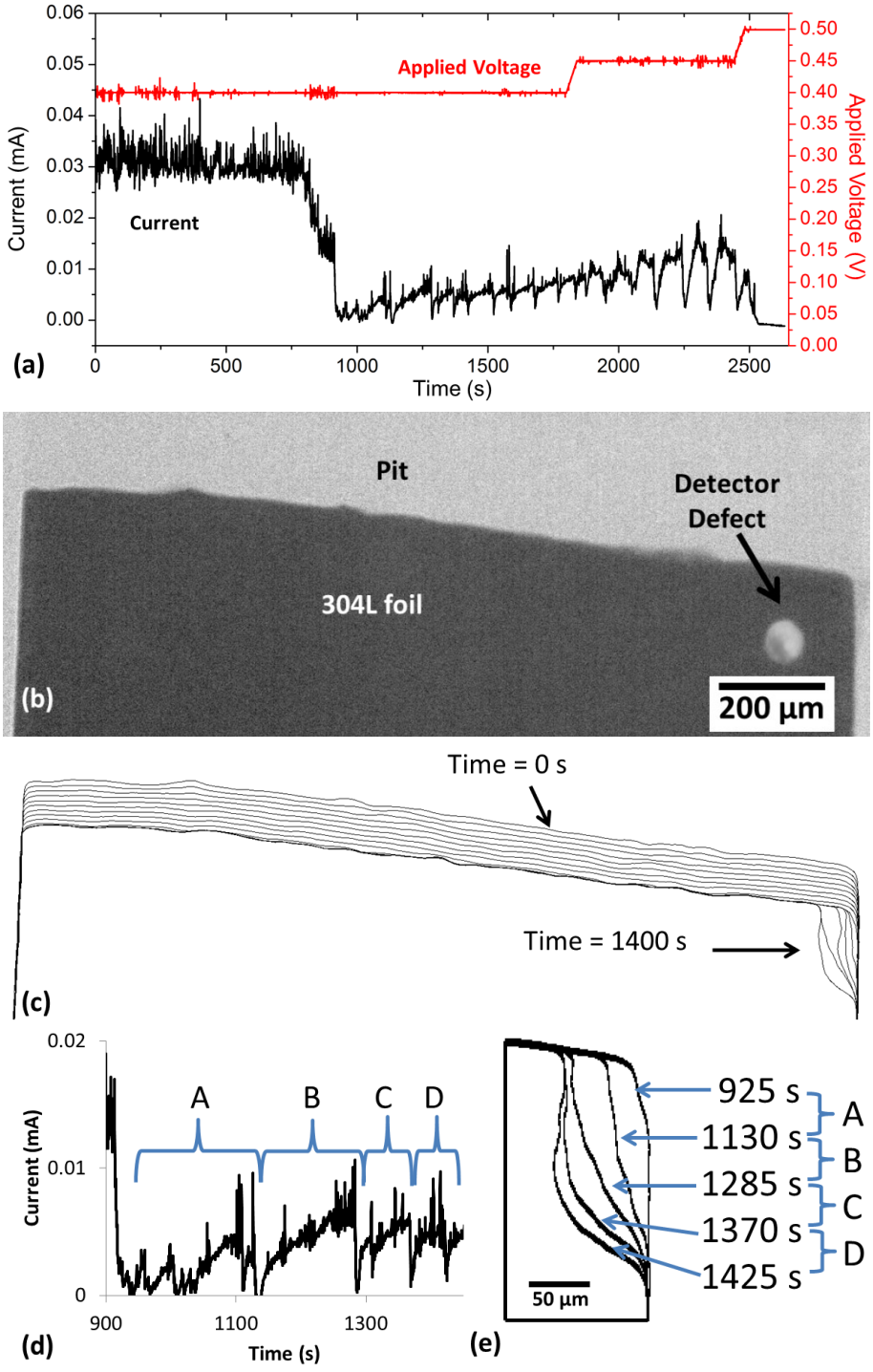

Figure 4-6 (a) Electrochemistry of 25 µm thick 304 L artificial pit in 1 M NaCl, then changed to 75 mM $NaNO_3$ + 1 M NaCl at approximately 500 s. (b) Radiograph of artificial pit at 0 s, (c) Edges of the corrosion front at 100 s intervals using edge-detection algorithm, (d) detail of electrochemical data between 900 s and 1425 s, showing surges in current, (e) details of radiograph edges at the crevice on the right-hand side of the foil between surges in current [56].

4.2.5.Corrosion front roughness results

The variations in foil height as the pit corrodes under a salt layer can be quantified in terms of roughness using standard techniques[179]. The edge from each radiograph had its background extracted by taking the average value of the height of each pixel from 50 pixels either side (101 pixels in total) and subtracting this to get a background corrected scan (Figure 4-7a). The roughness of this scan was then calculated using the *Root Mean Square* method [179]:

$$R_{SD} = \sqrt{\frac{1}{M}\sum_j \left(R_j - R_a\right)^2} \qquad \textit{Equation 4-1}$$

Where R_{SD} is the roughness index, M is the number of points, R_j is the height at point j, and R_a is the average height. While corrosion is proceeding under a salt layer there is no trend in roughness. Once the process of passivation begins (approx. 775 s) the roughness increases until 1000 s where the bulk of the surface is passivated, where the roughness remains high.

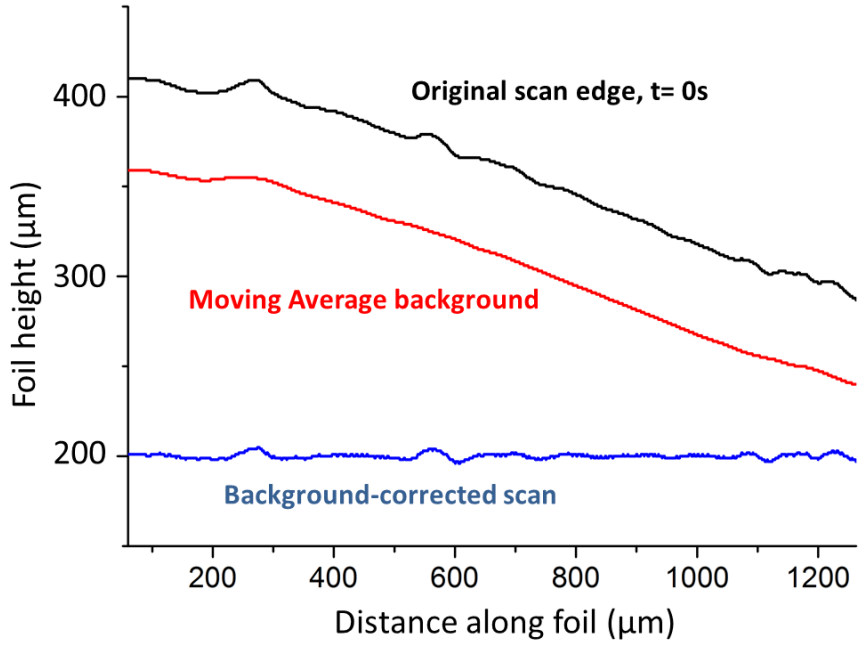

(a)

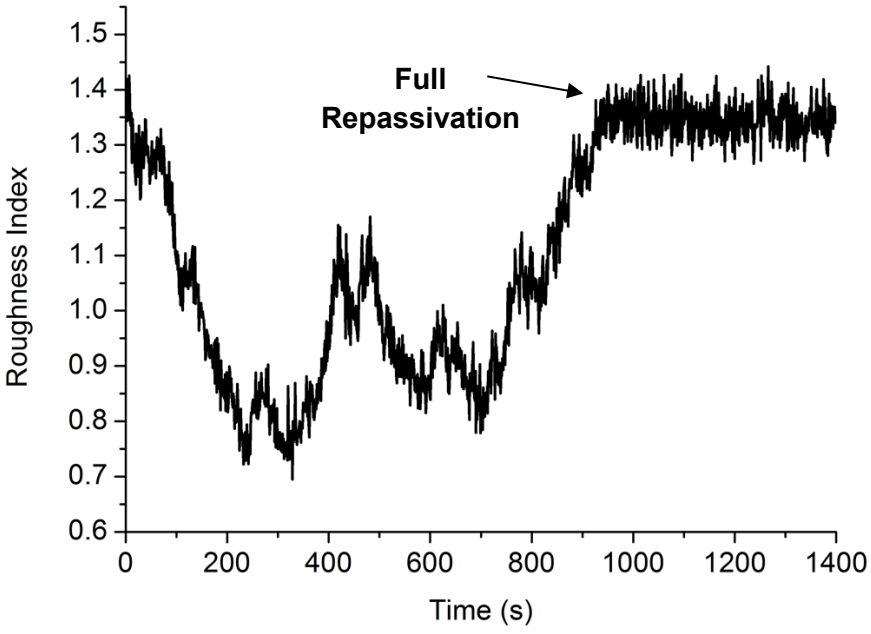

(b)

Figure 4-7 (a) The corrosion front of 25 µm 304 L stainless steel foil at time 0 s. A moving average was obtained and subtracted from the original data to give the background corrected surface. Lines have been displaced to improve visibility, (b) Roughness values of the corrosion front calculated from the background-corrected scan during dissolution [56].

Figure 4-8a shows the height of the background corrected scans as time increases. It can be seen that the location of peaks and troughs on the corrosion interface changes during dissolution, indicating local variation in current density and interfacial potential. In Figure 4-8b, which shows the rate of change in the pit height over a 10 s period, at approx. 775 s a point at ~1200 µm passivates. This passivation propagates along the pit surface until 1000 s where the entire pit is passivated. Once this occurs, the pit growth is effectively zero. This shows that the passivation process begins locally and spreads rather than a uniform transition over the whole corroding surface.

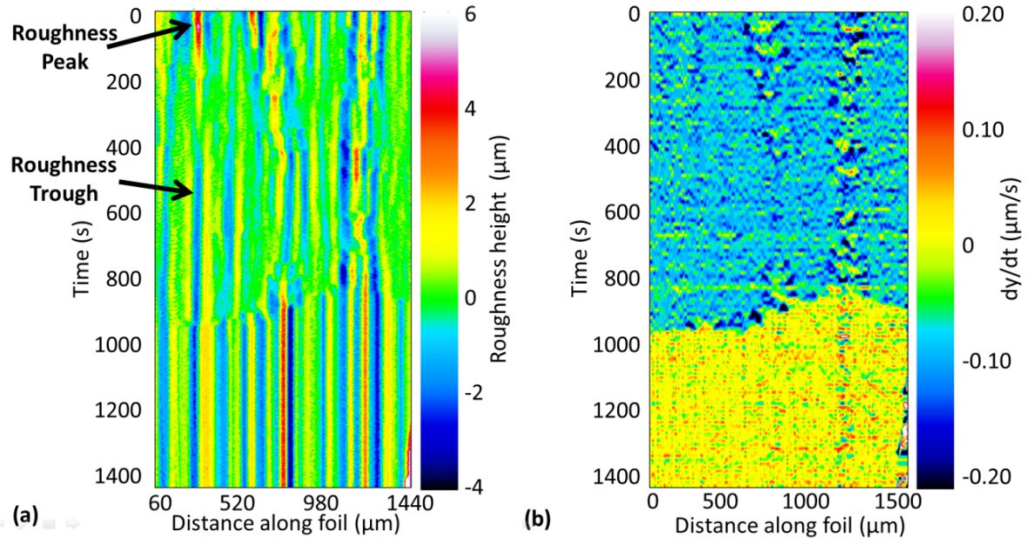

Figure 4-8 Corrosion front of 304L stainless steel over time, initially in 1 M NaCl then in 75 mM $NaNO_3$ + 1 M NaCl at approximately 500 s. (a) background-corrected edges over time, with 60 µm cropped from each side. (b) Difference between original scans every 10 s [56].

4.3. Discussion

In all conditions tested, a single diffraction pattern was observed that matches closely to Verbist's $FeCl_2.4H_2O$, but with minor peaks missing in all cases and a wide variation in peak intensities between scans. The absence of minor peaks implies a subtle change in space group or unit cell, possibly the existence of a super cell as postulated where minor reflection planes are removed. This is consistent with results

found in experiments on Fe in nitrate/chloride solutions [6, 69]. While the species detected has yet to be satisfactorily modelled, it can be stated that its presence in nitrate-free solutions indicates that it is not a nitrate salt, and therefore electrochemical oscillations cannot be the result of a competition between two or more salt crystals forming at different potentials [100]. Newman and Ajjawi [14] suggest the presence of a "nitrate-rich salt film" that passivates the corroding surface by going through a series of redox reactions or electrochemical reduction in the salt layer that raises local pH, promoting oxide stability. While these data suggest there is no crystalline nitrate salt present, the pores between the crystallites in the salt layer could have an elevated concentration of nitrate in solution. This increase in local nitrate concentration could cause a decrease in E_{pass} locally, making it easier to passivate. Newman and Ajjawi also noted that during active dissolution and supersaturation there was no passivation, but as soon as a salt formed during an upward sweep of potential the pit surface passivated. The precipitation of the salt layer, which is significantly thicker before equilibrium is reached, would affect solution concentrations at the interface. The salt formed would consume large amounts of chloride ions, raising the relative concentration of nitrate ions in the vicinity of the corrosion interface in comparison to before precipitation. This would increase the likelihood of local regions of passivation on the corroding interface.Another factor is the speed of oxide layer formation, with oxide layers in nitrate solutions forming more quickly than in chloride solutions with higher electric field strengths [90, 96]. There is no evidence of nitrate reducing current density at the corrosion interface or interrupting transport in the bulk [94].

Uhlig and Leckie's competitive adsorption model [88], where chloride ions are preferentially adsorbed below E_{pass} and nitrate above, was one of the first mechanisms proposed to explain this phenomenon. The model does not necessarily account for current understanding of interfacial potentials of one-dimensional pits under salt layers [13]. As current density is independent of applied potential when under one-dimensional diffusion, the interfacial potential is broadly constant even as potential is swept upwards. The electric field experienced by atoms at the corrosion interface is thus constant. This challenges the competitive adsorption model when under salt layer.

Rodriguez [87] uses Beck's [60] observation that, if salt behaves as an ohmic conductor, thick ohmic salt layers are less acidic than thinner ones because of the balance of electromigration and diffusion of ions and protons through the pit. This increase of pH may also account for Newman and Ajjawi's observation of passivation immediately after salt layer precipitation. By raising pH, Rodriguez suggests water becomes the passivating agent. However, he does not address any effects of reduced water activity at the highly concentrated interface, which have been observed previously [6].

The anisotropy observed in Figure 4-5 with the addition of nitrate shows that although nitrate may not affect the salt species formed but there is an influence of the morphology on the salt crystals. The monoclinic nature of $FeCl_2.4H_2O$ allows certain planes of crystallites to grow preferentially, which could allow the creation of elongated crystallites. The addition of nitrate may have interrupted the growth along certain planes, creating more regular crystallites and decreasing anisotropy. There is also evidence in the nitrate-rich sample (Figure 4-5b) of increased diffraction spot

size, indicating a coarsening of crystallite size [168]. In carbon steel, the addition of nitrate affected the diffraction pattern also but in the opposite trend, i.e. anisotropy increased with addition of nitrate [6]. This difference has not yet been explained but it may be attributed to the influence of chromium.

While SEM images of the corroding surface without nitrate shows evidence of uniform corrosion whilst under a salt layer (Figure 4-3a), the secondary pitting seen after nitrate additions and current oscillation (Figure 4-3b) appears to be the result of two corrosion processes occurring simultaneously. This is evidence of local passivation events occurring on the pit surface, which could lead to variations in electrochemical behaviour and the oscillations.

There appear to be some inconsistencies in E_{pass} between the diffraction data (0.6 V) and the radiography data (0.5 V). Both have the same solution chemistry and ratio between NO_3^-:Cl^-, which has been observed to be crucial in determining passivation potential [14, 88]. It is conceivable that radiolytic effects may have been more pronounced in the radiography data due to the high flux of X-rays entering the system, but this would have instead lowered local pH and made any passive oxide layer less stable. The most likely cause of difference in passivation potential is the dimensions of the pit cell. XRD pits were 50 μm thick, whereas radiography pits were 25 μm thick. At 0.4 V, slight current oscillations were observed in the XRD results which were much more pronounced in the radiography results. This may be due to partial passivation of the corroding surface: in the radiography results, a greater fraction of the surface area will be affected by partially passivated regions, especially if these regions butt up against the cell wall. Regions of the same size will

be able to be undercut more readily in the XRD experiments, so make it possible for critical chemistry to be maintained at more passivating conditions.

Radiography (Figure 4-8a) shows that even in the absence of nitrate the corrosion front has a roughened texture when grown under a salt layer. This roughened texture is also observed in SEM (Figure 4-3a). This is a result of local variations in current giving slightly different dissolution rates. The texture is not necessarily constant and changes during dissolution with new peaks being formed over time. As a peak is formed, the *IR* drop the interface experiences at that peak is slightly lower so allows slightly greater dissolution. This is the mechanism that keeps salt-covered dissolution flat [54, 63]. Passivation begins on the surface of the pit, but only locally (Figure 4-8b) at 800s. At this point, the roughness increases until the whole surface passivates, as shown in Figure 4-7b. This increased roughness is due to the reduction in solution concentration above the passivated region. This allows corroding regions adjacent to the passivated region to lose the salt layer and experience active dissolution. As active dissolution does not have the self-regulating properties that diffusion-limited dissolution under a salt layer has, roughness increases. In these highly concentrated solutions, a decrease in local concentration also leads to an increase in conductivity and diffusivity. This results in a higher interfacial potential and higher dissolution rate in the regions directly adjacent to the passive region. As the passivity propagates across the corrosion surface the roughness of that surface increases with it.

Figure 4-9 illustrates how the combination of these effects may give electrochemical oscillations. The salt covered surface before oscillations has a salt layer and experiences mostly uniform corrosion (Figure 4-9a). Local variations in the current

allow passivation to occur at a point on the surface, stopping dissolution above that region (Figure 4-9b). This decreases concentration above this region, increasing conductivity and solubility and allows corrosion directly adjacent to these regions to be increased. This increased dissolution continues and undercuts the passivated region (Figure 4-9c). This continues until the passivated region is fully undercut, lifts off and allows a surge of dissolution. This surge will increase current momentarily, but quickly supersaturate and precipitate on the surface (Figure 4-9d), bring the

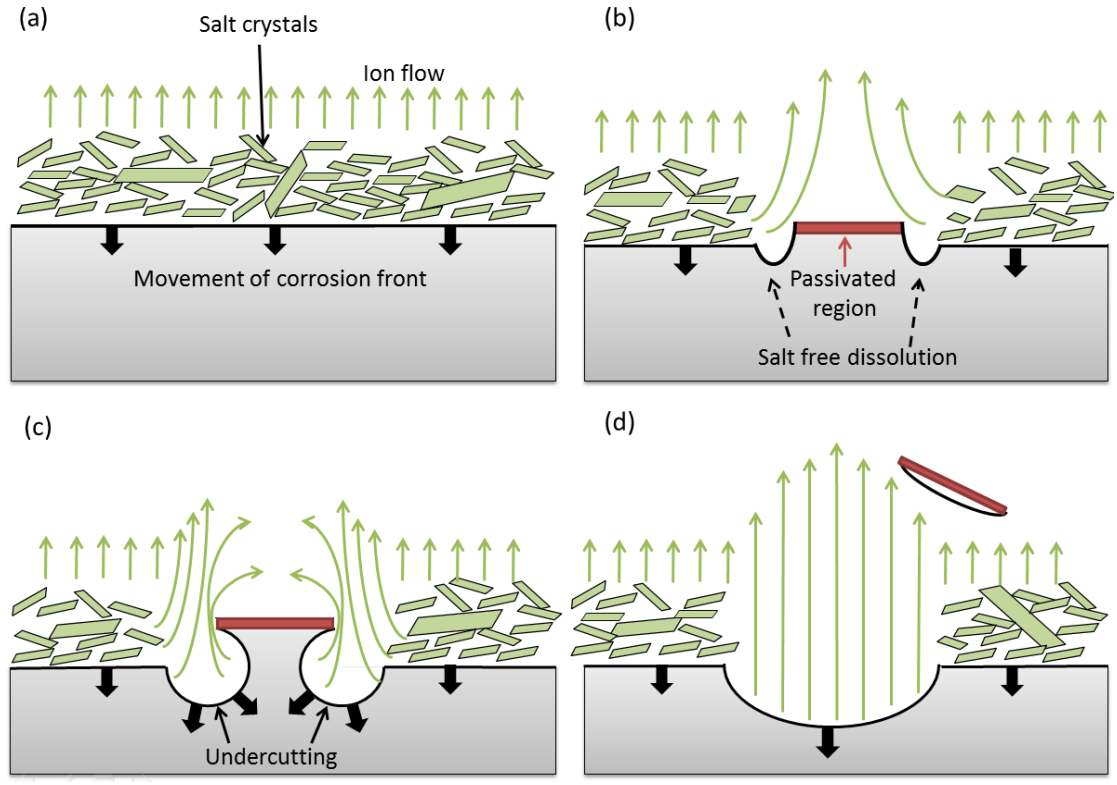

Figure 4-9 Suggested mechanism that results in current oscillation in pits. (a) Normal corrosion under a salt layer before oscillation, (b) localised passivation blocks some of the current, but allows diffusion-limited current to continue, (c) this continued corrosion undercuts the passivated regions, (d) these undercut regions experience surge in current before supersaturating in a salt layer [56].

current down again. It is proposed that the secondary pitting seen in Figure 4-3b is a consequence of this process. This theory is similar to that proposed by Okada, who suggested islands of passive region nucleate on the corrosion interface under halide solutions near the passivation potential [86]. Alternative theories as to what cause this oscillatory behaviour involve homogeneous processes occurring simultaneously over the corrosion surface. For example [100], it has been suggested that the generation of H^+ by hydrolysis is repelled by the electromagnetic field present across the salt layer, which raises local pH and passivates the corroding interface. This then lowers the field strength, allowing the return of H^+ ions and continues the cycle again. This mechanism is not likely to occur in these experiments as it would be difficult for passivated surfaces to begin active dissolution again, and does not explain the secondary pitting observed by SEM or the proximity of the oscillations to the passivation potential.

The propagation of passivation we have observed in the radiography experiments can be considered using the same mechanism as described in Figure 4-9. If the partially passivated region is too large, the passivated region can propagate at a rate too great to allow it to be undercut by the advancement of the corrosion front.

4.4. Conclusions

- For 304L stainless steel artificial pits in $NaCl/NaNO_3$ solutions, there exists a passivation potential above which the corroding surface of the alloy passivates. At potentials approaching this value, current oscillations are observed.
- The crystal species of the salt layer on the corrosion surface appears the same regardless of nitrate concentration or electrochemical behaviour. This salt

pattern most closely resembles $FeCl.4H_2O$ as described by Verbist *et al*.[178] with some minor peaks missing from the pattern.

- The diffraction patterns collected showed anisotropy in NaCl solutions, possibly caused by elongated crystallite morphology. A decrease in anisotropy occurred as nitrate concentration increased, indicating a disruption in the preferential growth planes of the crystallites. The diffraction patterns also had larger spots on them, indicating some larger crystallite sizes.
- *Ex Situ* SEM images showed that on the surface of pits that had no nitrate, there was a consistent surface roughness. In pits that showed electrochemical oscillations, secondary pitting was observed.
- Radiography data were obtained simultaneously with electrochemical data. Slight variations in surface roughness were observed during dissolution, indicating a constant variation in local interfacial potential across the interface. When nitrate was added to NaCl solutions, passivation began locally and propagated outwards.
- A model was proposed where local regions of partial passivation are undercut and made active again, accounting for the large oscillations in current.

5. Atmospheric corrosion of 304L stainless steel under droplets of $MgCl_2$

5.1. Introduction

Atmospheric corrosion differs from full-immersion corrosion in several important ways. Atmospheric corrosion typically has limited volumes of electrolyte which are in highly concentrated solutions, as the water activity of the solution tends to reach equilibrium with the surrounding humidity. Droplets of saline solutions have long been used to simulate the effects of atmospheric corrosion. However, a consensus on the key factors dictating the location of this corrosion has yet to be reached.

The first major discussion of corrosion under droplets was by U.R. Evans [116, 117] who used NaCl with a phenolphthalein/potassium ferrocyanide addition as pH indicators on freshly-ground mild steel to show a strong trend for anodic dissolution in the centre of corroding droplets and cathodic reactions occurring around the droplet edge. This was explained by "differential aeration", with oxygen supply to the surface of the metal being significantly easier to access under the thinner layer at the edge of the droplet. Evans also observed that where corrosion initiated at the edge of the droplet it slowly migrated towards the centre, inferring that the passive layer was less stable there.

Some evidence has accumulated which suggests that corrosion under a droplet does not always appear to be well explained by the Evans model. Wire beam electrode arrays constructed with carbon steel [151] and 304 stainless steel [128] have been used to show a strong trend in corrosion at the droplet edge under large droplets of between 15 and 200 μl at deposition.

A wide range of pitting initiation sites has been observed on 304L stainless steel within large sets of droplets, with pit position in the droplet often influencing the pit morphology [126]. Some examples of wet/dry cycling of $MgCl_2$ droplets on 430 and 304 stainless steels have shown no strong trend in initiation site when cycled up to 6 times [125]. It has been suggested that this lack of trend in initiation site may be due to a reduced rate of oxygen consumption due to changes in the passive layer of oxide, removing the differential aeration in the solution [180].

Pit morphologies have been explored in full immersion conditions [158, 181]but little work has been done on atmospheric corrosion at OCP . Vera Cruz *et al.* [150] described "colonies" of pits occurring in stainless steel with a single large pit surrounded by several smaller ones when under thin solute layers. Morphology is also influenced by microstructure [139, 157], solution concentration at the pit mouth [10, 153, 158] and pit potential [159]. Instances have been recorded where these morphologies have had implications in failure under SCC and fatigue regimes [182].

This work will look at the effects of droplet deposition conditions and experimental relative humidities on the pit morphology and pit position under droplets of $MgCl_2$.

5.2. Results

OLI Analyzer 9 [183] was used to generate values of the relationships between $MgCl_2$ solution concentration and equilibrium relative humidity (Figure 5-1a), electrical conductivity (Figure 5-1b), and Fe^{2+} self-diffusivity (Figure 5-1c) at 30 °C . The deliquescence humidity of $MgCl_2$ is 33% RH at this temperature yielding a saturated solution of 5 M $MgCl_2$, as is shown elsewhere [114]. Conductivity of the solution is zero at 0 M and increases until it peaks at about 2.4 M $MgCl_2$, or 77% RH.

It then drops again until saturation. Self-diffusivity decreases as solution concentration increases.

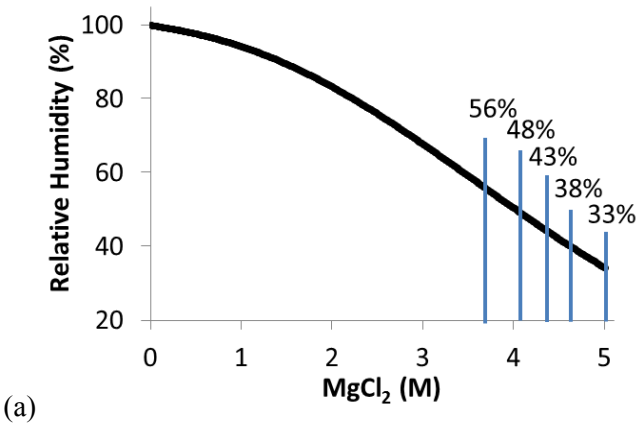

(a)

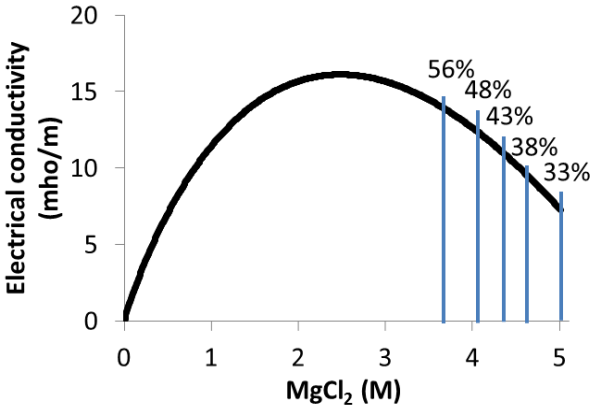

(b)

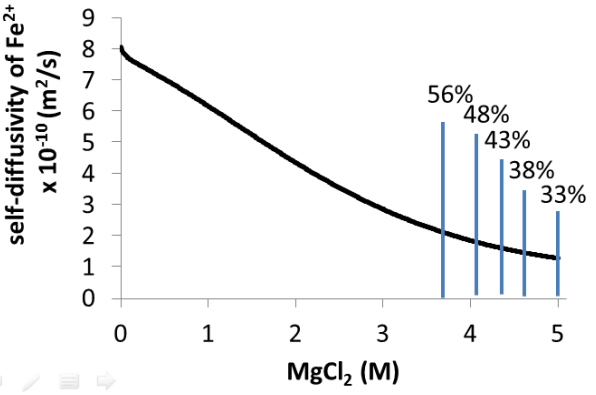

(c)

Figure 5-1 Relationship between solution concentration of $MgCl_2$ (M) and (a) relative humidity (%) , (b) electrical conductivity (mho/m), and (c) self-diffusivity of Fe^{2+} (m^2/s) in $MgCl_2$ solutions at 30 °C, calculated using OLI Analyzer 9 [183].

Figure 5-2 shows optical micrographs of droplets for CDDs of 80 μg/cm^2, 750 μg/cm^2, and 5400 μg/cm^2 after 24 hours of exposure to 33% RH at 30 °C. In general droplets contain one pit, but in some cases two were observed. 80 μg/cm^2 CDD droplets often had crystals growing across the surface with a needle-like morphology.

Droplets with 5400 μg/cm^2 CDD experienced an increase in surface area during 24 hours to an average value of 0.078 cm^2, a surface area increase of 53% (Table 3-4). However, all pits appeared in the region covered by the initial deposit. Droplets at lower CDD did not change perimeter during experiment noticeably.

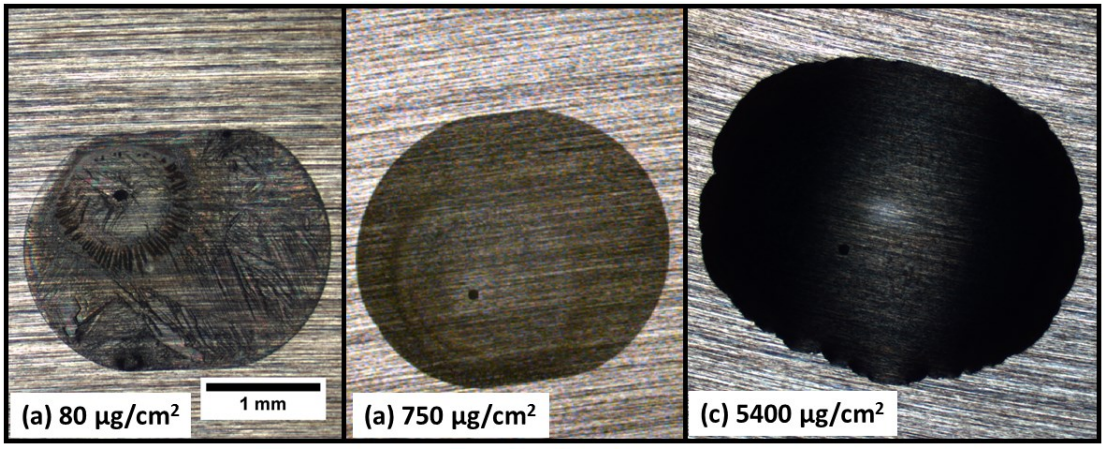

Figure 5-2 Optical images of droplets 24 hours after deposition when held at 33% RH and 30 °C. Chloride deposition densities of droplets are (a) 80 μg/cm^2, (b) 750 μg/cm^2 CDD and (c) 5400 μg/cm^2. A single pit is observed under each droplet which can be seen as a dark spot in the images [126].

Pitting in 80 μg/cm^2 CDD droplets all showed a similar pitting morphology. Pits had a shallow dish-shaped region that had deeper attack on one side, and outside the shallow dish region there were several satellite pits (Figure 5-3a). Satellite pits never occurred within the shallow dish region, though Mohammed-Ali did see instances of this [131]. Crystallographic etching was a common feature of the shallow dish

region. Out of 56 droplets, 43 pitted (77%) and of these, 36 showed this morphology, which is shown schematically in Figure 5-4. The remaining 7 droplets that pitted showed no distinct pitting morphology. 18 of the 43 pitted droplets had needle-like crystals growing across the droplet surface (e.g. Figure 5-2a). Crystal-growth was only observed on droplets that had pitted, and was not present on any of the 13 droplets that did not pit.

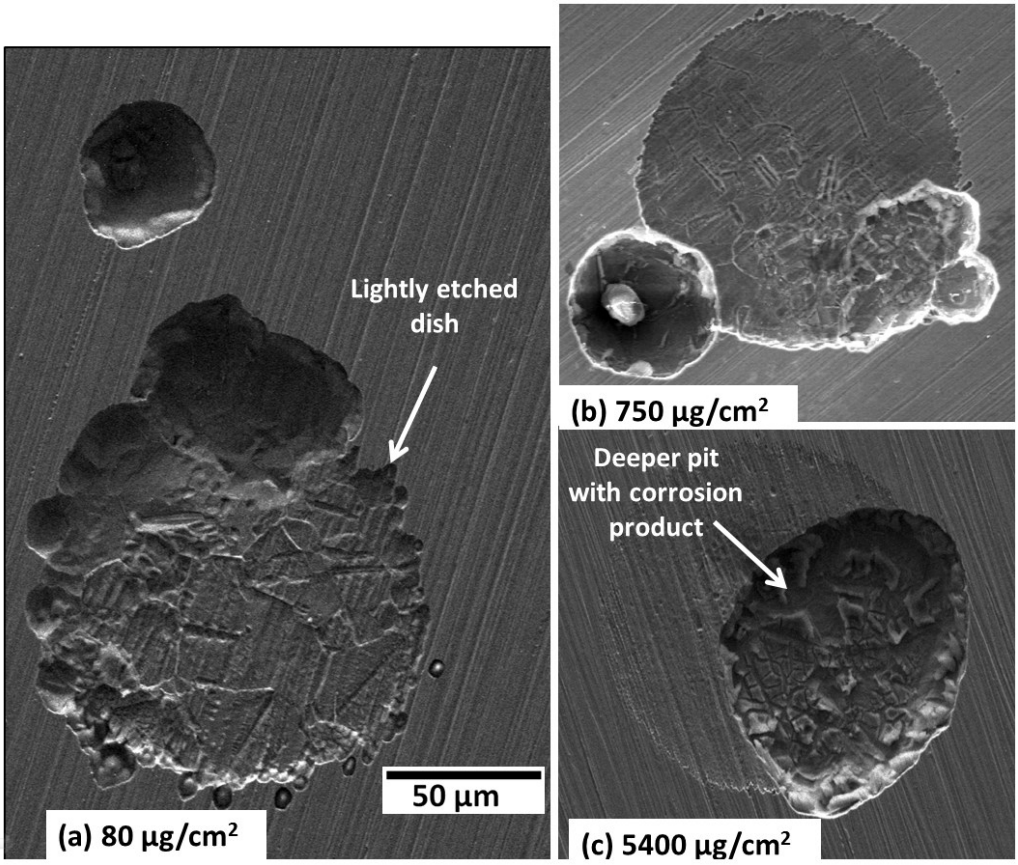

Figure 5-3 Secondary electron SEM images of pits grown under a $MgCl_2$ droplet at 33% RH and 30 °C for 24 hours. Chloride deposition density of droplets was a) 80 µg/cm² CDD, b) 750 µg/cm² CDD and c) 5400 µg/cm² [126].

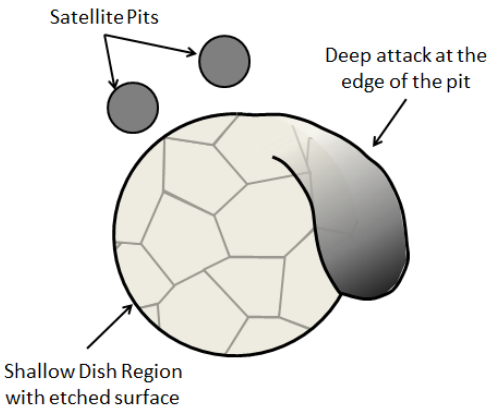

Figure 5-4 Schematic diagram describing features shown in Figure 5-3.

In droplets with 750 μg/cm^2 CDD, the same etched shallow dish region with satellite pits was observed, again usually with one side showing more corrosion (Figure 5-3b). The circumference of the shallow dish region at this CDD was usually smoother than at a CDD of 80 μg/cm^2. 52 out of 56 droplets pitted under these conditions, with 49 of those that pitted showing this morphology.

In droplets with 5400 μg/cm^2, all 56 droplets pitted. 33 out of 56 droplets showed shallow dish regions with less pronounced etching than that observed at lower CDDs (Figure 5-3c). The pit was much larger than in lower CDDs. Only 1 out of 56 pits had a satellite pit. Those that did not show a shallow dish had very large pits with pit mouths ≥100 μm in diameter. It is possible that these pits may have overgrown and consumed any shallow dish region that had previously formed.

5.2.1. Time-lapse growth

Figure 5-5 show time-lapse images of pits growing under 1400 μg/cm^2 CDD droplets of $MgCl_2$ taken by optical microscope at 30 °C ± 3 under various relative humidities. Humidities were controlled with saturated salt solutions.

In 33%RH (Figure 5-5a) pitting started within 20 minutes of deposition of the droplet. A shallow dish region developed by radial growth from the original initiation site, and had grown to its full area by 70 minutes. After this, attack continued on one edge of the shallow dish region, which has been referred to as "earing" in the literature [136] that develops into a spiral morphology. Simultaneously, a small pit develops above the shallow dish region and continues to grow over time. By 990 minutes, the attack inside the shallow dish region has stopped but the satellite pit has continued to grow.

In 43%RH (Figure 5-5b) pitting started within 28 minutes. This pitting developed into a shallow dish region which continued to attack on one side, much like 33% RH. However, no satellite pits were formed and this attack continued in to develop a spiral-shaped morphology within the bounds of the shallow dish region.

In 52%RH (Figure 5-5c) pitting started later, by 40 minutes after deposition. This pit developed much like the pit at 43%RH, with a shallow dish region developing into a spiral-shaped pit, but with the final pit growing to a larger size more quickly.

In 56%RH (Figure 5-5d), pitting started much more slowly than at lower humidities. A shallow dish region did not appear to develop and instead a more hemispherical pit morphology is observed.

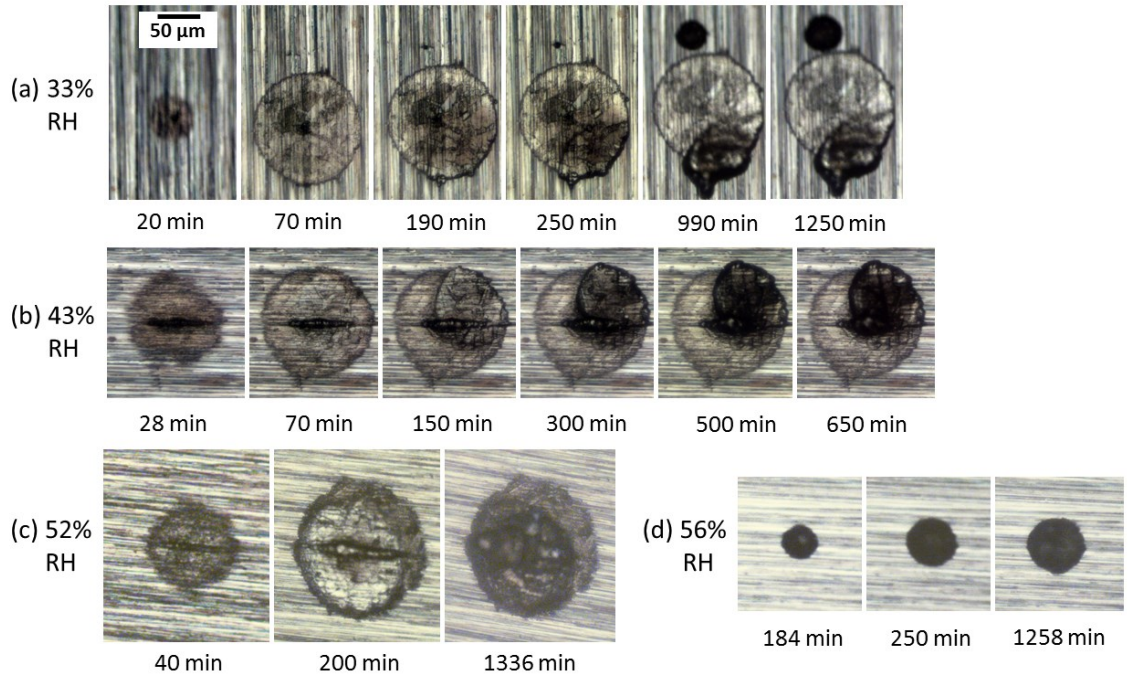

Figure 5-5 Optical time-lapse images of pits under droplets held of $MgCl_2$ in constant humidity at 30 °C with CDD of 1400 µg/cm^2. Droplet was 2 µl of 0.5 M $MgCl_2$ at deposition in each case, with typical droplet diameter approx. 2.5 mm. Relative humidity held at (a) 33%, (b) 43%, (c) 52% and (d) 56%. Humidity controlled by saturated salt solutions in each case: 33% by $MgCl_2$, 43% by K_2CO_3, 52% by $MgNO_3$ and 56% by NaBr.

5.2.2. Pit Morphologies

Typical morphologies of pits grown under droplets of 750 µg/cm^2 CDD are shown in Figure 5-6. At 33% RH, 49 out of 52 droplets that pitted showed a shallow dish region with crystallographic etching , with deeper attack on one side, and satellite pitting at or near the perimeter of the shallow dish (Figure 5-6a). Satellite pits appeared to have caps that showed grinding marks that lined up with those of the metal surface (Figure 5-7). Dissolution inside the satellite pits appears to show crystallographic etching, as observed by Mohammed-Ali [131], which could indicate active dissolution rather than salt covered dissolution . EDS analysis of the pit caps gave typical compositions of ~40% Cr, ~45% O, ~5% S, and ~10% Cl.

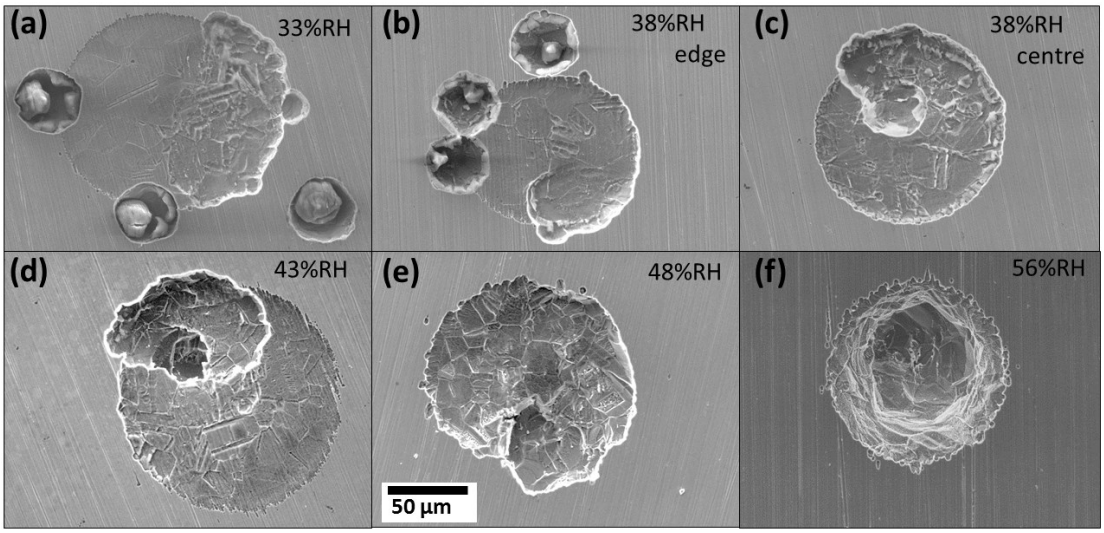

Figure 5-6 Typical morphologies of pit grown under $MgCl_2$ droplets with 750 µg/cm_2 CDD at for 24 hours at 30 °C on 304L stainless steel. Pits observed in (a) 33% RH, (b) 38% RH near droplet edge, (c) 38% RH near droplet centre, (d) 43% RH, (e) 48% RH and (f) 56% RH [126].

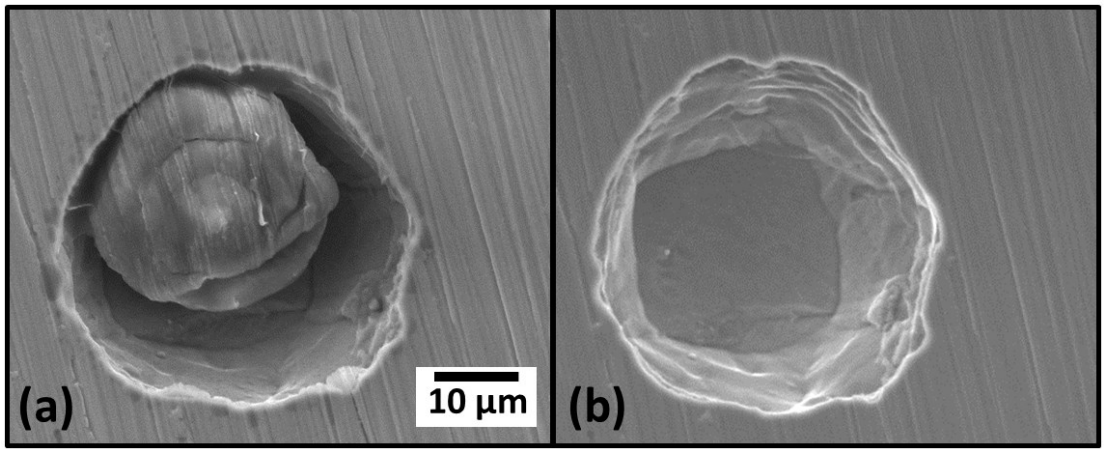

Figure 5-7 Satellite pit from 33% RH in Figure 5-6 (a) before and (b) after ultrasonic cleaning in DI water for 30 seconds. Pit caps of the type seen in (a) showed typical EDX compositions of ~40% Cr, ~45% O, ~5% S, and ~10% Cl [126].

At 38% RH, all 56 droplets pitted. However, two dominant pit morphologies occurred. 37 pits showed the "satellite" morphology described above (Figure 5-6b) and 16 pits showed pits that had developed into a spiral morphology within the shallow dish region (Figure 5-6c).

At 43% RH, 56 out of 60 droplets pitted. Of these, 54 pits showed a spiral morphology (Figure 5-6d). The shallow dish region again was crystallographically etched and more strongly attacked at one side. One pit showed the "satellite" pit morphology, and one pit had grown to propagate outside the droplet region and had developed an irregular morphology.

At 48% RH, 55 out of 56 droplets pitted and 53 showed pits with the spiral morphology. (Figure 5-6e). Two droplets contained pits that showed growth along the rolling direction of the steel, indicating a susceptibility to microstructural features.

At 56% RH, all 56 droplets had pits but none of them had a shallow dish region (Figure 5-6f). Instead they showed more classical pitting morphology with narrow circular mouths. 24 droplets (43% of the total) showed at least two pits that were more than 500 μm apart.

5.2.3. Effect of pit location on morphology

The relationship between shallow dish region size and location under the droplet was analysed. The diameter of the shallow dish region was determined by drawing a circle around the dish region that had formed in the initial stages of pitting (Figure 5-8). assuming growth was essentially under diffusion control and propagated radially from an initiation site at the centre of the shallow dish region. Those pits that did not have visible shallow dish regions were not included in this analysis. Plots of the diameter of the shallow dish as a function of distance from the droplet edge are shown in Figure 5-9.

For droplets with a CDD of 750 $\mu g/cm^2$, the size of the shallow dish region appeared to be affected by pit location. At 33% RH, the dish diameters showed a high degree

of scatter. Despite this wide variation, there is a broad trend for shallow dish regions to have larger diameters towards the centre of the droplet than those found towards the edge (Figure 5-9). This trend is also true at all higher relative humidities tested in this study, with less scatter at 38% RH and 48% RH. From 38% RH to 48% RH, pits that occurred near the edge of the droplet were not only generally smaller than those towards the centre but had less variation in diameter.

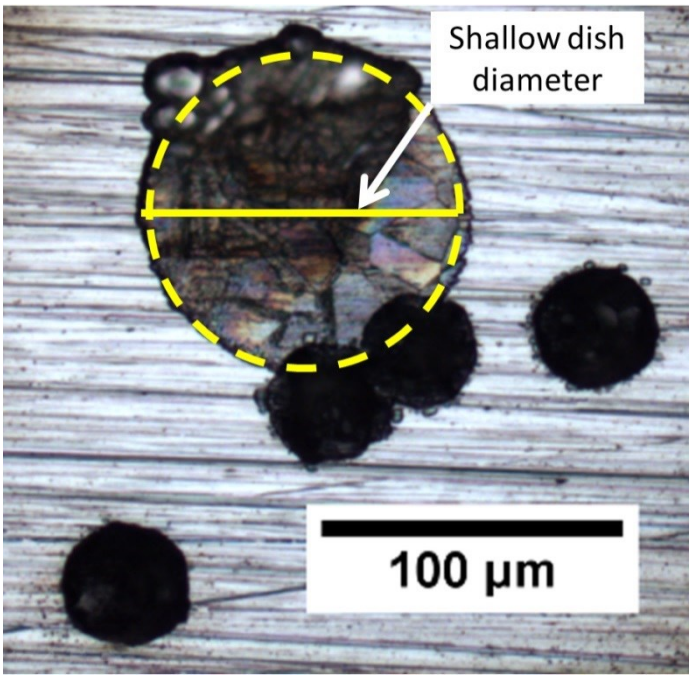

Figure 5-8 Diagram showing method used for measuring shallow dish region seen during pitting. Circumference of etched part of SDR is traced and extended over deeply attacked region. Diameter is then calculated from this circle [126].

At 38% RH, there appears to be a transition in pit morphology between satellite pits and spiral pits. Towards the edge of the droplets satellite pits form and spiral pits form towards the centre. As it can be assumed that the bulk solution is the same concentration across the entire droplet, the thickness of the solution above these pits appears to influence pit development.

Satellite pits occur more towards the edge of the droplet, whereas spiral pits more towards the centre. At higher humidities the majority of pits were spiral, and there were fewer dish regions smaller than 80 µm diameter. In general, shallow dish region appears to increase as the humidity increases, as can be seen from the average value of these datasets (Table 5-1). As the dataset from 56% RH did not show any shallow dish region in any of the pits, it could not be included in this analysis.

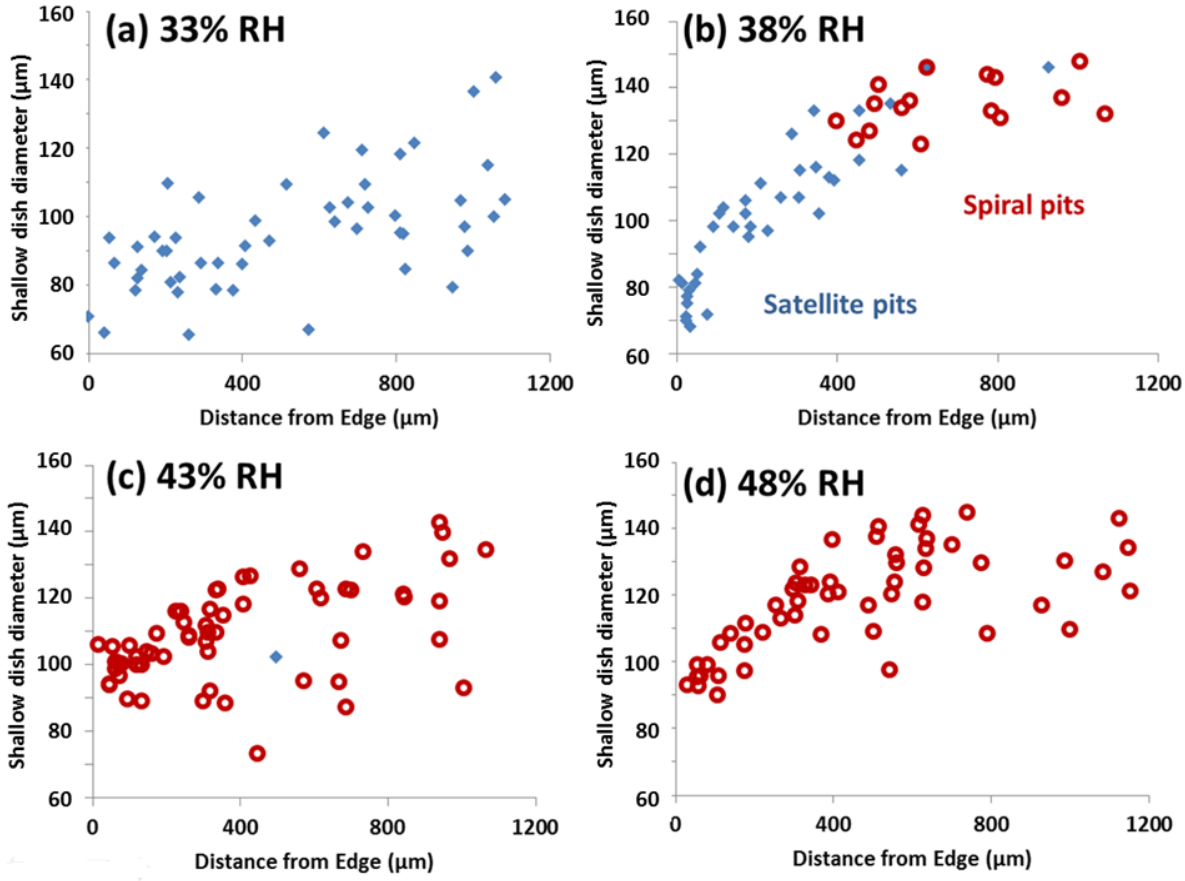

Figure 5-9 Diameter of shallow dish regions against distance from droplet edge in $MgCl_2$ droplets with a CDD of 750 µg/cm^2 after 24 hours at 30 °C. Satellite pits are shown as blue diamonds and spiral pits are shown as red circles [126].

Table 5-1 Average diameters and standard deviations of pits formed in $MgCl_2$ droplets with a CDD of 750 µg/cm^2 after 24 hours at 30 °C

RH (%)	Diameter average (µm)
33	95±17
38	110±23
43	110±14
48	120±15

5.2.4.Statistical analysis of the effect of RH and CDD on Pit Location

The previous results prompt a question as to whether there are any explicit trends in the initiation position of pits under droplets with varying pitting conditions. There have been suggestions that "differential aeration" can influence which regions under a droplet undergo the oxygen reduction reaction, making these regions immune from attack [116, 184]. To investigate this two sets of experiments were conducted, (1) droplets with the same initial concentration (0.27 M $MgCl_2$) were deposited under various humidities, and (2) sets of droplets with different initial concentrations (0.14 – 5 M $MgCl_2$) were deposited at 33% RH.

Employing the use of the chi-squared (χ^2) test and binomial standard deviation, it is possible to determine if there is a preference in pitting position by dividing the droplet into two areas of equal size, one towards the centre and one towards the edge, and counting how many pits occur in each region.

5.2.5.Measuring inner and outer droplet areas

Droplets were of an approximately elliptical shape at and after deposition (Figure 5-10a) and elongated along the grinding lines of the plate. The major, *2a*, and minor,*2b*, axes of each droplet were measured using the initial droplet area, allowing

the construction of an elliptical perimeter. The distance and angle of the pit centre from the centre of the ellipse were measured. Pit centre was determined to be the centre of the shallow dish region, which is the morphological feature that appears during initiation of pitting under atmospheric conditions on stainless steels (Figure 5-8) [126, 136, 162].

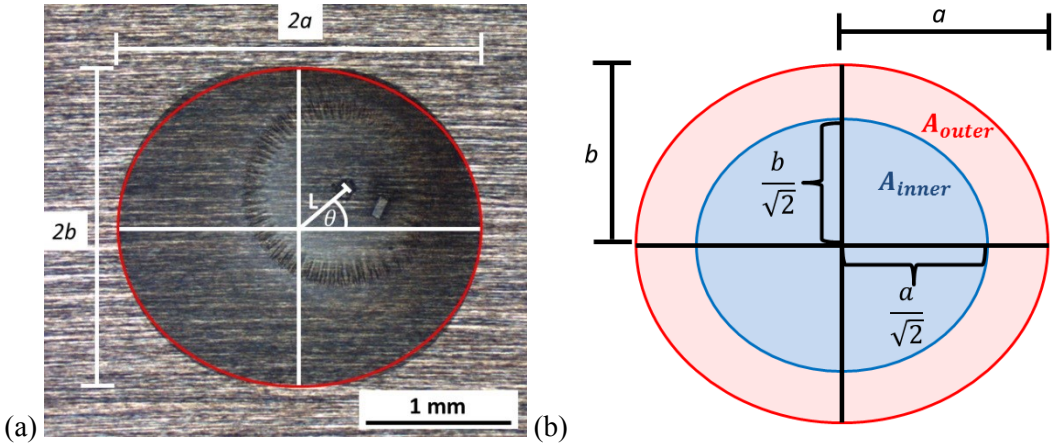

Figure 5-10 (a) Measurement of semi-major axis, a, and semi-minor axis, b, of the ellipse formed by droplet deposition. Ellipse outline was calculated using general equation of an ellipse. Angle, θ, and distance of pit, L, measured from ellipse centre. 2 µl droplet was 0.27 M $MgCl_2$ solution held at 30 °C and 33% RH on 304L stainless steel for 24 hours, (b) calculation of equal A_{inner} and A_{outer} regions using measured a and b values for each droplet.

The ellipse was then divided into two regions of equal area: an internal ellipse that has a semi-major axis of $\frac{a}{\sqrt{2}}$ and a semi-minor axis of $\frac{b}{\sqrt{2}}$ (inner region), and an outer annulus of equal area (outer region) (Figure 5-10b). Using the measured distance, *L*, and angle, θ, of the pit from the centre of the droplet, the position of the pit can be determined algebraically to see if it is in the inner or outer region, i.e if the pit is in the inner region, then the following is satisfied:

$$\frac{(Lcos\theta)^2}{\left(\frac{a}{\sqrt{2}}\right)^2} + \frac{(Lsin\theta)^2}{\left(\frac{b}{\sqrt{2}}\right)^2} \leq 1 \qquad \text{Equation 5-1}$$

Otherwise, the pit is considered to be in the outer region. This accommodates samples where the actual droplet perimeter extends outside the calculated droplet perimeter.

5.2.6.Statistical Analysis

This analysis generates data that is considered "categorical" i.e. results will fall into discrete categories, in this case "inner" or "outer" regions. This allows for statistical techniques that employ categorial data to be used to interpret the pitting position. A "null hypothesis" approach was used where it was assumed that there is no relationship between a pit's initiation site and its position under the droplet. By defining the equally sized regions to be at the edge (outer) and at the centre (inner) of the droplet, the influence of droplet thickness and "differential aeration" caused by oxygen diffusion limitation can be investigated. A bias of results in favour of either region would indicate a relationship between pitting and position. Two statistical methods were used to analyse the validity of the null hypothesis: Chi-squared test and binomial standard deviation.

5.2.6.1. Chi-squared (χ2) distribution test

A chi-squared test can be used to give a probability of the null hypothesis being valid. As the number of pits in the inner region, n_i, and outer region, n_o, would be equal given a dataset of size n, a chi-squared value can be calculated:

$$\chi^2 = \frac{\left(n_i - \frac{n}{2}\right)^2}{\frac{n}{2}} + \frac{\left(n_o - \frac{n}{2}\right)^2}{\frac{n}{2}} \qquad \text{Equation 5-2}$$

This value is then used to calculate the cumulative distribution function using the *chi2cdf* function in MatLab [185], with a degree of freedom df=1. This gives H_0, the probability of these data agreeing with the null hypothesis. ***H_0* values of greater**

than 5% are generally considered to show no significant statistical variation from the null hypothesis, meaning no trend in pitting position.

5.2.6.2. Binomial standard deviation.

A binomial distribution can be used to analyse the deviation of the dataset from the mean. Assuming the null hypothesis is correct, the standard deviation, σ_{H_0}, of this data set can be written as the square root of the variance of a binomial distribution:

$$\sigma_{H_0} = \sqrt{np(1-p)} \qquad \text{Equation 5-3}$$

Where n is data set size, and p is the probability of pitting occurring in the inner region, i.e. 0.5 for the null hypothesis.

5.2.7.Effect of changes in Relative Humidity (RH) on pitting position

The results of different exposure humidities on 2 µl droplets of 0.27 M $MgCl_2$ are summarised inTable 5-2. Figure 5-11 shows the results of pitting for droplets exposed to humidities between 33% RH and 59% RH. Between 33% RH and 53% RH, the variation between the null hypothesis and the recorded results falls within σ_{H_0}, or one binomial standard deviation.. At 59% RH, results lies within $2\sigma_{H_0}$ showing a slight trend for edge initiation. Figure 5-12 shows a strong probability for satisfying the null hypothesis when relative humidity is held at or below 53% RH. At 59% RH, the probability of satisfying H_0 is only 14%, but this is still above the 5% threshold usually considered for determining statistical relevance in χ^2 tests, so can still be considered to have a low probability of a trend in data.

Table 5-2 Quantitative results of pitting position of 2 µl droplets of 0.27 M $MgCl_2$ held at 30 °C on 304L stainless steel at 30 °C in different RH. Exposure time is 24 hours in each case. Degrees of freedom (df) of H_0 is 1.

RH	**33%**	**38%**	**43%**	**48%**	**53%**	**59%**
Number of droplets	56	56	60	56	56	56
Total pitted (n)	52	56	55	55	56	55
Outer region	25	29	25	30	25	33
Inner region	27	27	30	25	31	22
Chi squared (χ^2)	0.077	0.071	0.45	0.45	0.64	2.2
H_0 Probability (%),df=1	78	79	50	50	42	14
H_0 Standard Deviation (σ_{H_0})	3.5	3.7	3.8	3.7	3.7	3.6

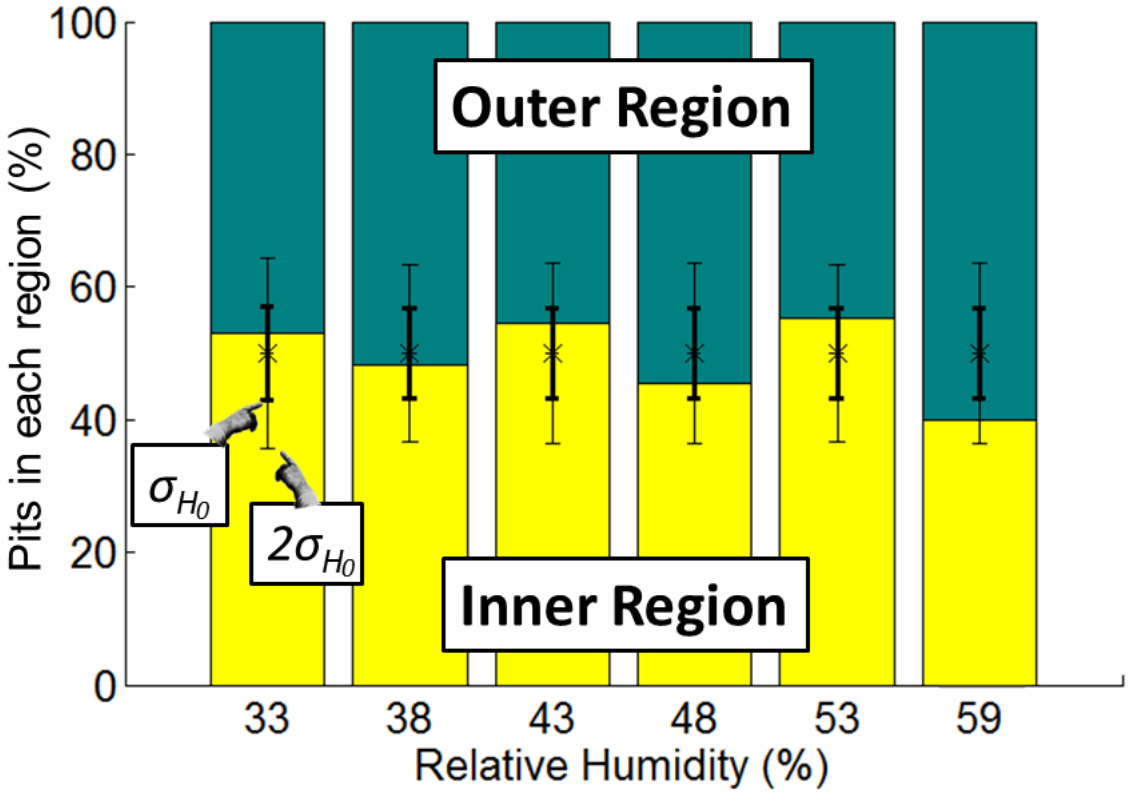

Figure 5-11 Percentage of pits that occurred in each region under 2 µl droplets of 0.27 M $MgCl_2$ on 304L stainless steel at 30 °C in different RH. Error bars are binomial standard deviation, σ_{H0}, expected of each set assuming the null hypothesis

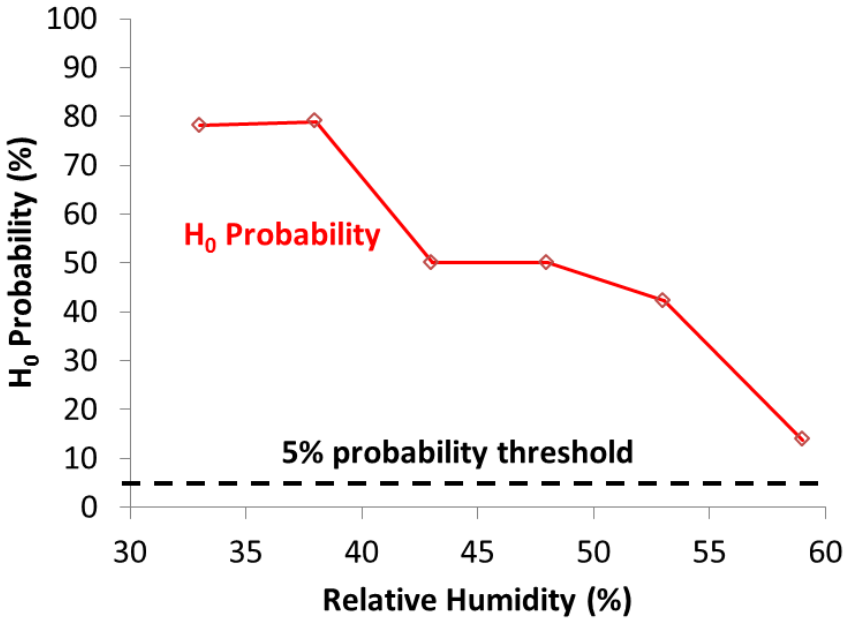

Figure 5-12 Probability that the null hypothesis (H_0) is satisfied of datasets of 2 µl droplets of 0.27 M $MgCl_2$ on 304L stainless steel at 30 °C in different RH. 5% probability threshold shown, above which datasets can be considered to satisfy the null hypothesis. Degrees of freedom, df=1

5.2.8. Effect of solution concentration

The results of different solution concentrations of $MgCl_2$ at deposition of 2 µl droplets are summarised in Table 5-3. Results in Figure 5-13 show that at low initial concentrations, between 0.14 M and 1 M $MgCl_2$, all data falls well within σ_{H_0} of 50%. The probability of satisfying the null hypothesis (H_0) at these concentrations is high (Figure 5-14), which supports this observation. When deposition concentration increases and is between 1.5 M and 3 M $MgCl_2$ a distinct trend develops for more pits to be initiated in the outer region of the droplet, i.e. towards the edge. In highly concentrated solutions between 4 M and 5 M $MgCl_2$ this trend reverses, and pitting occurs most often in the inner region, i.e. towards the centre of the pit. The H_0 probability (Figure 5-14) for concentrations 1.5 M to 5 M $MgCl_2$ is less than 1 % in all cases, making the null hypothesis unlikely.

Table 5-3 Quantitative results of pitting position of 2 µl droplets with varying concentration $MgCl_2$ held at 30 °C on 304L stainless steel at 30 °C in 33% RH. Exposure time of 24 hours in each case

Deposition Concentration (M)	**0.14**	**0.27**	**1**	**1.5**	**2.25**	**3**	**4**	**4.5**	**5**
Number of droplets	40	56	45	100	46	86	45	44	66
Total pitted (n)	35	52	42	99	46	86	43	44	66
Outer region	19	25	22	64	33	57	13	12	2
Inner region	16	27	20	35	13	29	30	32	64
Chi squared (χ^2)	0.26	0.08	0.10	8.5	8.7	9.1	6.7	9.1	58
H_0 Probability (%), df=1	61	78	76	0.35	0.31	0.25	0.94	0.25	0
Standard Deviation (σ_{H_0})	2.9	3.6	3.2	4.8	3.1	4.4	3.0	3.0	1.4

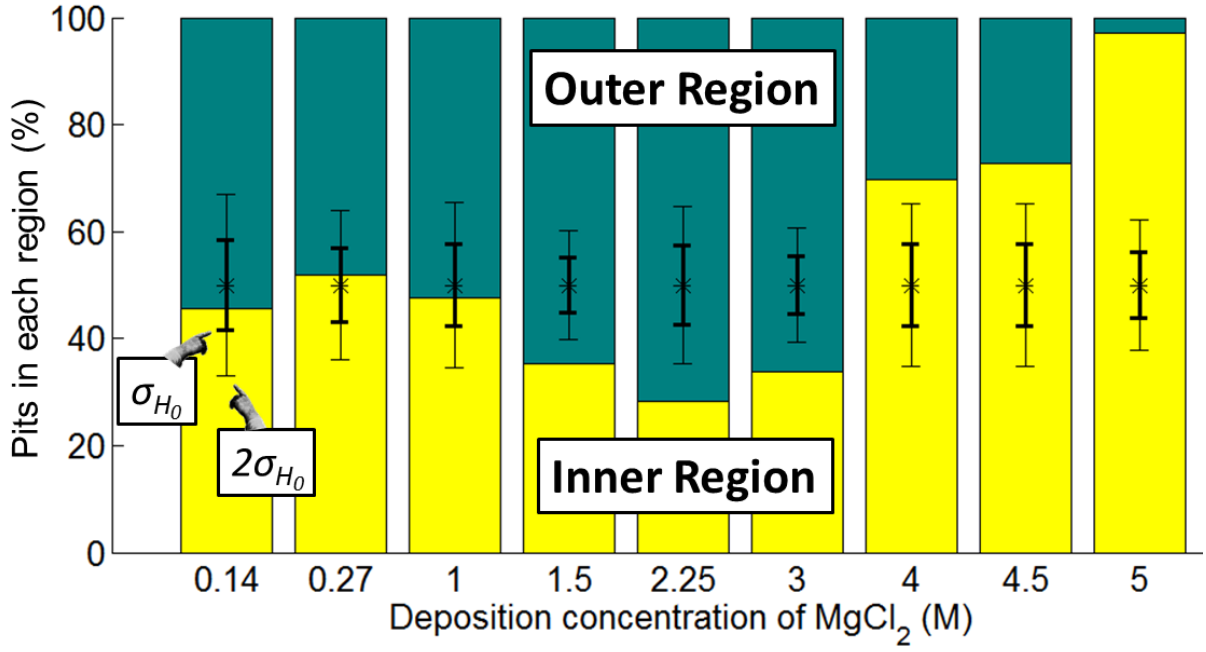

Figure 5-13 Percentage of pits that occurred in each region under 2 µl droplets of $MgCl_2$ at 33% RH on 304L stainless steel at 30 °C at different deposition concentrations. Error bars are the binomial standard deviation, σ_{H0}, expected of each set assuming the null hypothesis

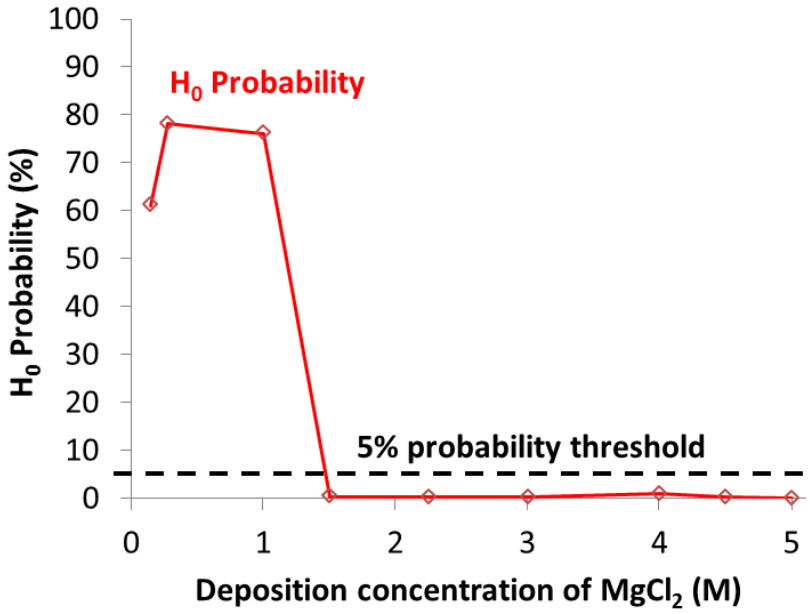

Figure 5-14 Probability that the null hypothesis (H_0) is satisfied of datasets of 2 µl droplets of varying $MgCl_2$ concentration on 304L stainless steel at 30 °C in 33% RH. 5% probability threshold shown, above which datasets can be considered to satisfy the null hypothesis. Degrees of freedom, df=1

5.2.9. Ag wire electrochemistry

Ag wires have been used to study the initiation times after deposition of droplets and to inform analysis of time-lapse data shown in Figure 5-5. Figure 5-15 shows a 2 µl droplet of 0.5 M $MgCl_2$ immediately after deposition on freshly ground 304L plate. The Ag wire can be seen on the right-hand side of the droplet. By measuring changes in potentials between the Ag wire and the steel plate initiation processes can be detected (Figure 5-16). Immediately after deposition, no pitting is observed and the potential can be seen to drop slightly before rising again, most likely due to a thickening of the passive oxide layer. Some metastable pitting events can be seen with potential dropping sharply before eventually recovering. At 1215 s the potential drops sharply and stays low for the duration of the experiment. This coincides with the development of a pit under the droplet shown in Figure 5-16.

Differences in behaviour of different solution concentrations at deposition have also been investigated (Figure 5-17), with time starting at the deposition of the droplet in each case. One droplet of each solution was tested in each case. When 4 M $MgCl_2$ was deposited, pitting began virtually immediately with only a momentary rise in potential before initiation. 2 M and 3 M $MgCl_2$ droplets showed momentary drops in potential before pitting finally initiated, with 3 M droplet pitting after 50 s and 2 M droplet after 180 s. 1 M $MgCl_2$ droplet pitted after 320 s. The fluctuations in potential did not occur at this concentration, and indeed potential was seen to reduce initially then increase until pitting initiated.

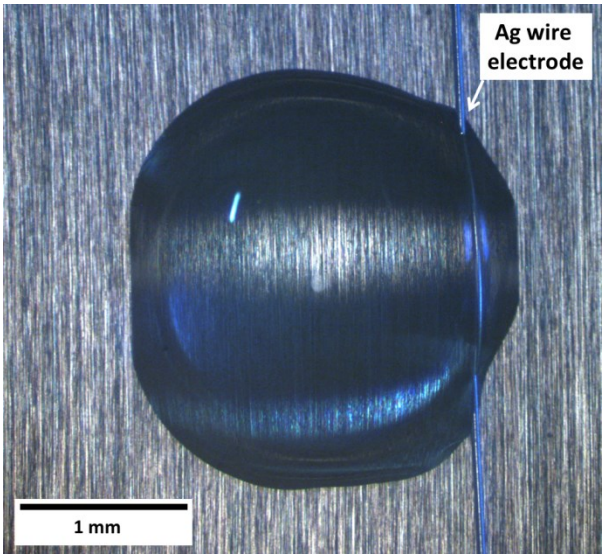

Figure 5-15 2 µl droplet of 0.5 M $MgCl_2$ after deposition on 304L stainless steel. Ag wire electrode is seen running top-to-bottom on right hand side of droplet. The wire is connected to steel plate via a two-electrode potentiostat that measures the potential difference between the two electrodes.

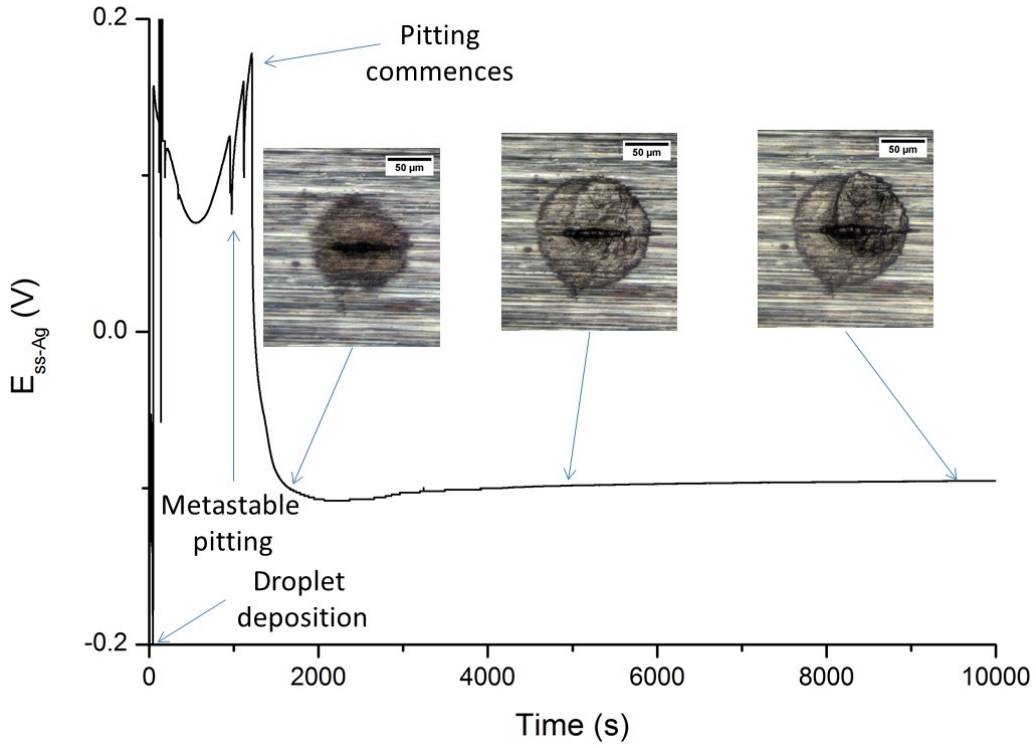

Figure 5-16 Results from silver wire electrode experiment shown in Figure 5-5. 2 µl droplet of 0.5 M $MgCl_2$ deposited and held at 43% RH and 30 °C on 304L stainless steel. Chloride deposition density was 1400 µg/cm^2. Wire was held 40 µm above steel surface.

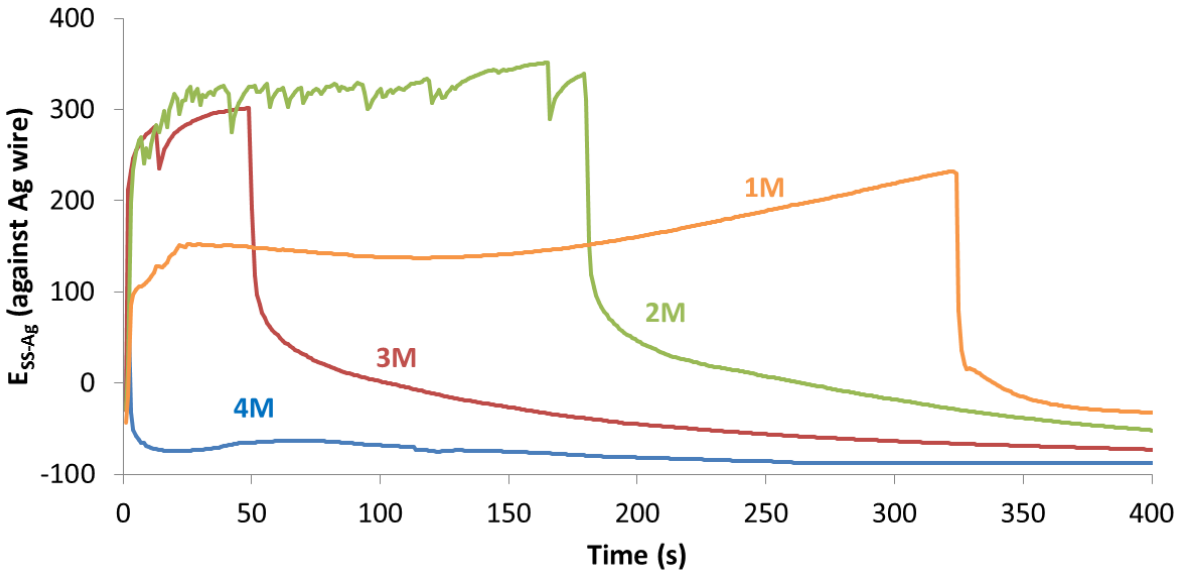

Figure 5-17 Potential difference data of Ag wire electrodes of 2 µl droplets of $MgCl_2$ on 304L stainless steel plates. Droplets deposited at 30 °C in 33% RH atmospheric chamber (TES). Different droplet concentrations at deposition are labelled. Time of deposition is at 0 s in each case

.

5.3. Discussion

5.3.1. Pit Morphology

Atmospheric corrosion is caused by the presence of a saline electrolyte that is of limited volume and highly concentrated. These factors combine to cause a general reduction in conductivity and ion diffusivity when compared with more dilute solutions and must be considered to understand how pit morphology is affected by humidity.

At 52% RH and below, localised corrosion begins with a shallow dish region [136, 150, 162]. This shallow dish starts at a single point, most likely a sulphide inclusion [28], and propagates out radially as seen in the time-lapse figures (Figure 5-5). The crystallographic etching observed in the shallow dish region (Figure 5-3) is evidence of either activation controlled dissolution or passive dissolution, as the presence of a salt layer is likely to create a roughened surface [53, 58]. It has been suggested that

the increased passive current density observed in highly concentrated solutions [12, 126] may cause these shallow dishes, which will be discussed in the following chapter..

Maier and Frankel [136] suggested the adsorption of elemental S to the passive surface around the pit, caused the attack to grow in a radial fashion. Hastuty *et al.* [162] also proposed a mechanism for shallow dish growth, based on hydrolysis of metal ions after the dissolution of sulphur-rich inclusions. However, the influence of initiation concentration on pit position under these droplets shows that the inclusion chemistry is not the only factor that determines pit morphology.

Atmospheric corrosion is considered to be cathodically limited [163, 186], as the rate of corrosion is determined by the access of oxygen on the metal surface. While the shallow dish grows, it requires a sufficient current density to maintain an aggressive solution to allow corrosion to propagate along the unoccluded steel surface. Once the shallow dish region reaches a critical size, the cathodic current supplied to it can no longer support further growth and the pit ceases to grow outwards. The spiral attack then develops as a smaller region and is able to maintain a critical chemistry more easily. In these very thin droplet solutions, the conductance through the electrolyte is limited, providing a large IR-drop between the anodic and cathodic regions.

Pits occurring at the edge of droplets have smaller shallow dish region diameters (Figure 5-9). The limited conductance through narrow solution pathways will create a high IR drop between the anode and the far edges of the droplet. As such, there will be more limited access to cathodic current, resulting in smaller shallow dish regions.

5.3.1.1. Satellite versus spiral morphology

Time-lapse images showed that for all pits that had shallow dish regions, attack continued on one side of the shallow dish and developed into "spiral" morphology (Figure 5-5). However, those that also formed satellite pits showed that the spiral eventual stopped growing whilst the satellite pit continued to develop (Figure 5-5a). This was seen to happen mostly in 33% RH droplets and towards the edge of 38% RH droplets (Figure 5-6a and b) with CDD of 750 $\mu g/cm^2$ or lower. The satellite pits were protected by pit caps (Figure 5-7). Pits grown at 33% RH with CDD of 5400 $\mu g/cm^2$ and pits grown at 43% RH and above rarely showed evidence of satellite pits.

Once the growth of the shallow dish region stops, pitting continues as both satellite and spiral pits grow. The stability of the satellite pit during its initiation depends upon its ability to prevent repassivation . Having highly concentrated solutions, such as those found at 33% RH, would not only make the already acidified solution around the shallow dish region more acidic but it would also reduce ion diffusivity. This would make it easier for the satellite pit to maintain an aggressive solution. The thickness of the solution layer also has an influence, as a thin solution layer would have a more difficult diffusion pathway away from the initiation site. This would allow satellite pitting sites to overcome the transition from metastability [49]. The satellite pit caps allow pits that grow to remain more stable than the spiral attack that is occurring in the shallow dish region as they are less occluded. The competition for the limited cathodic current is inevitably won by the satellite pits which continue to grow after the spiral has died.

At high RH and under thick solutions spiral pits grow, although IR drop is still significant and only part of the shallow dish region can continue to be attacked. In

very high CDD, such as in 5400 μg/cm^2 droplets being held at 33% RH, the absence of satellite pits is likely due to the combined effect of reduced IR-drop through the solution, allowing continuous attack after the shallow dish region growth had stopped, and the increased diffusion pathway away from any possible satellite initiation sites due to the thickness of the solution.

5.3.2. Pit Position

Three distinct trends are observed in pitting, relating to the deposition concentration of the droplet (Figure 5-18).

1. At low deposition concentrations, pits are evenly distributed throughout the droplet.
2. At higher concentrations but where initiation is not immediate, pitting is more likely to occur near the droplet edge.
3. At the highest concentrations, where initiation can begin immediately, pitting is more likely to occur near the centre of the droplet.

The thickness of the droplet at the moment of initiation is important to understanding the three trends in behaviour observed as deposition concentration increases. To support pitting in the crucial early moments of attack, a sufficiently high potential and current are required to sustain active chemistry. Under droplets this translates to having a sufficiently large cathode area, as these systems are generally considered to be cathodically limited [163, 187], and a sufficiently conductive pathway (reduced IR drop) between the anode and cathode regions.

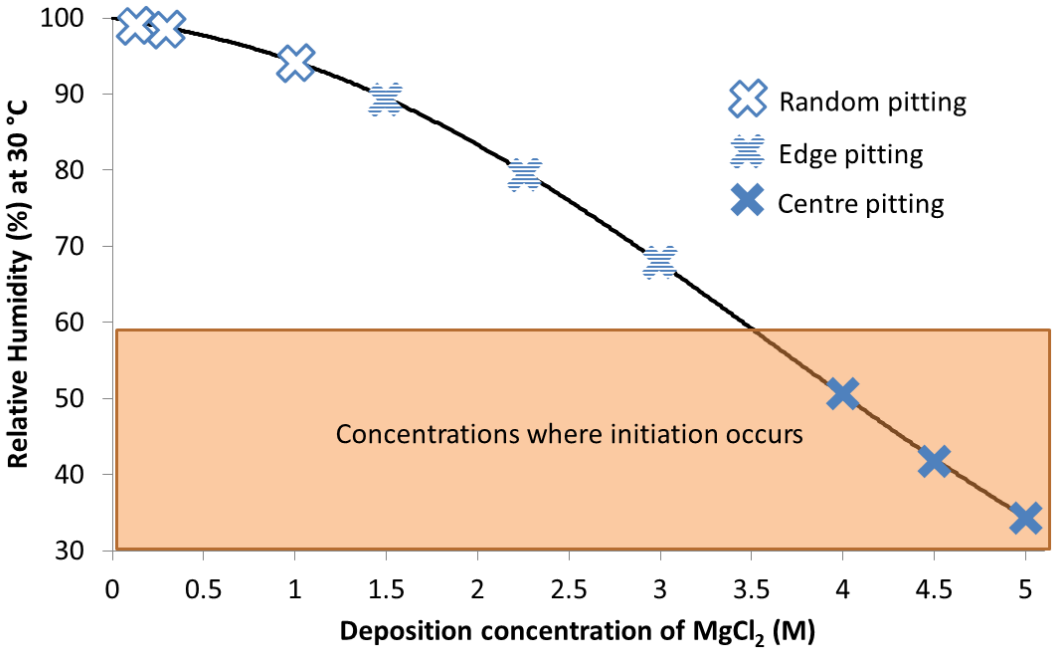

Figure 5-18 Pitting position trends of 2µl droplets of $MgCl_2$ as a function of deposition solution concentration and equivalent relative humidity. Data on 'concentrations where initiation occurs' taken from Nam et al.[125]. Droplets with low initial solution concentration (and CDD) showed no trend in pitting position. Those with initial solution concentrations between 1.5 and 3 M $MgCl_2$ showed a trend in pitting initiation at the edge of droplets. Those droplets of 4 M $MgCl_2$ and higher showed a trend to pit towards the centre of the droplet.

5.3.2.1. Trend 1: random pitting site

Droplets with deposition concentrations of 0.14 M – 1 M in 33% RH show no trend in pitting position. Those with deposition concentration of 0.27 M in RH between 33%-53% also show no trend. All sets are within σ_{H_0} of the null hypothesis, that there is no preference in pitting location (Figure 5-11 and Figure 5-13), and H_0 probability is high in all cases (Figure 5-12 and Figure 5-14), indicating that the null hypothesis is valid. Initiation is known to start at 47%-58% RH on 304L under $MgCl_2$ droplets at 25 °C [125], which is equivalent to 3.5 M to 4.1 M $MgCl_2$, so these droplets must lose a significant volume of water before initiation can begin. This creates thin droplets that allow oxygen access all over the metal surface, allowing strongly cathodic regions anywhere on the metal surface. However, the thin

droplets cause a large *IR*-drop meaning pitting must be proximal to strongly cathodic region.. Thus, pitting can occur anywhere on the droplet surface, and is determined metallurgically, not by differential oxygenation.

5.3.2.2. Trend 2: Edge pitting

Droplets with deposition concentrations of 1.5 M – 3 M $MgCl_2$ show a strong trend towards pitting at the edge of the droplet. Probability of pitting in the outside region was more than 2σ away from expected probability. H_0 is less than 1% in each case, indicating very weak adherence to the null hypothesis. Competition between pitting sites exists, as seen by metastable pitting on Ag wire (Figure 5-17). The concentrations of these droplets are not aggressive enough to initiate immediately, so need to lose water volume before pit initiation. When initiation does begin, droplets are thick enough to reduce availability of oxygen to the centre of the droplet compared to the edge, making strong cathodes appear towards the edge. The droplets still have a large *IR* drop, so pitting must initiate near a strong cathode, i.e. at the edge. Droplets with 0.27 M deposition concentration in 59% RH also show a slight trend towards edge initiation. Probability falls between σ and 2σ of expected probability, and H_0 probability is reduced to 14%, which is still significant but not as high as other data of the same deposition concentration. This initiation time may be longer as this is on the cusp of the initiation regime. It is possible that differential oxygenation may be generated by way of increased passive current density under high concentrations, which will be discussed further in the next chapter [126].

5.3.2.3. Trend 3: Centre pitting

Droplets of deposition concentration of 4 M – 5 M $MgCl_2$ show a strong trend for pitting towards the centre (Figure 5-13), a similar pattern to the Evans' model [116]. Pitting begins quickly in these concentrations, as shown by Ag wire experiments

(Figure 5-17). As these solutions are deposited at a concentration above that required for initiation to occur, all possible initiation sites will compete at deposition, consuming oxygen rapidly. Combined with the increased passive current density, this may result in a rapid consumption of all available oxygen in the solution, creating an oxygen concentration gradient inside the droplet.

Oxygen diffusivity is also slower at these high concentrations, so it would be more difficult to replenish solution near the surface once oxygen is consumed. This competition is not seen in the Ag wire experiments, possibly due to the low temporal resolution (1 s) which limits the ability to observe these events as they can be seen more clearly on shorter timescales [94]. Although conductivity is reduced at high concentration, conductance is increased due to the thick droplet layer, allowing easier access to the cathodic areas. This would allow large amount of cathodic current to be accessed towards the centre of the droplet.

5.3.2.4. Evans Droplet Model

Evans stated that, under NaCl droplets, "in the case of iron and steel, the distribution of anodic and cathodic areas is determined almost entirely by the oxygen-distribution in the liquid, and only to a small extent on the composition or physical character of the different portions of the metal"[116]. He further refined these observations [117], describing small localised anodic and cathodic areas initially dispersed all over the metal surface under the droplet, but once the dissolved oxygen was consumed and an oxygen concentration gradient had developed in the droplet, the anodic sites converged at the centre and the edge of the droplet acted as the cathode. This mechanism also provided an explanation of the death of anode sites near the edge,

with any iron ions released near the edge being deposited as solid hydroxides or oxides at the surface and “healing” the anodic sites.

Stainless steels, however, have very stable passive layers and the pitting location cannot migrate around the metal surface during growth. Initiation has been strongly linked with metallurgy and local inclusion chemistry, particularly with sulphides [28, 188], and propagation with occluding morphologies to maintain a critical chemistry [27]. This, in concert with the drop in potential preventing other sites from initiating and the cathodic protection of the rest of the pit surface, makes the drifting of pit location difficult. As observing more than one pitting site is rare after 24 hours, it can be assumed that the stability of pits under the conditions tested is sufficient to overcome other factors that would drive pitting to occur towards the centre of the droplet. As such, competition that generates a trend in location must occur early during the initiation stages of pitting, not during continual corrosion such as Evans witnessed on Fe.

5.3.2.5. Aerosol vs Splash zone

These results show a difference in pitting behaviour depending on whether droplets are deposited as concentrated or as dilute solutions. This is in essence simulating the difference between aerosol deliquescence conditions, where deposited particulate salts draw in moisture to form concentrated solutions, and “splash zone” conditions, where salt water splashes onto surfaces and dries out as it reaches equilibrium with the atmosphere.

Aerosol conditions, where droplets start at or near saturation, have very small initiation times and show evidence of rapid consumption of saturated oxygen. Pit initiation is determined not only by metallurgy but also by oxygen gradients inside

the solution. Splash zone conditions, where dilute solutions are deposited, have their pitting position determined entirely through metallurgy. Evidence for variation in corrosion behaviour has been observed when comparing droplets and salt particles of NaCl, $MgCl_2$, and ASTM standard sea water [113, 115, 189] with corrosion observed under salt crystals at humidities well below deliquescence RH, indicating the importance of an adsorbed water layer. Recent literature has shown instances where dilute droplets have been used to investigate corrosion regimes known to be caused by aerosol contamination, e.g. nuclear waste storage [126, 190, 191]. The current work further emphasises the need to appreciate the difference in application of the two models of atmospheric corrosion particularly in the early stages of corrosion.

5.3.2.6. High Throughput Methods

In both morphology and position analysis, the considerable scatter in measurements show that there is a need for large data sets when using droplets as atmospheric corrosion models on commercial alloys. Trends in corrosion behaviour only make themselves apparent when using high throughput techniques. Pitting behaviour also appears to be sensitive to local variations in solution chemistry and geometry that affects conductivity and diffusivity.

5.4. Conclusions

- Atmospheric pitting corrosion of 304L stainless steel was analysed using droplets of $MgCl_2$ after 24 hours of pitting at 30 °C. It was found that the pit morphology and pit position are sensitive to RH and CDD.

- Pits grown at RH values ≤52% grow initially as crystallographically-etched shallow dishes, then develop into different morphologies depending on solution thickness and concentration.
- At low RH (33%), the shallow dishes develop small satellite pits that grow under caps rich in Cr, S, O and Cl. At higher RH (43% and 48%), attack into the shallow region continues, but only in a small region, developing spiral attack with a roughened surface. At 56% RH, shallow dishes are not observed, and deeper and rougher pits are observed. For 38% RH, pits close to the droplet edge form satellites, whereas pits that form towards the centre of the droplet, where it is higher, show spiral attack.
- The change in pit morphology is attributed to changes in the IR drop between anode and cathode, and changes in solution conductivity and diffusivity with RH. Deeper spiral attack is observed for higher droplets (higher CDD at fixed RH or higher RH at fixed CDD). Higher RH values not only increase droplet height, but also increase the ionic conductivity and diffusivity of these highly concentrated solutions.
- Pit position is determined by the combined effects of the proximity to a strong cathode and *IR* drop through solution.
- When pitting initiates while droplets are very thin, oxygen diffusion is easy over the entire metal surface so there is no trend in cathode site or initiation position.
- In thicker droplets, oxygen depletion occurs towards the centre of the droplet which drives pitting towards the edge of the droplet to be near to the cathodic region as there is substantial *IR* drop.

- When droplets are deposited at high concentrations (i.e. that immediately allow pitting) oxygen depletion occurs in the centre of the droplet very quickly due to a combination of elevated passive current density, reduction of both concentration and diffusivity of oxygen in concentrated $MgCl_2$ solutions, and the immediate activation of all possible initiation sites consuming saturated oxygen. The *IR* drop is reduced so pitting is able to occur towards the droplet centre as this gives access to a larger cathodic region. This can be considered an Evans-like attack.
- Understanding differences in initiation conditions is significant as it allows a distinction to be made between 'aerosol' conditions, which begin with concentrated solutions, and "splash zone" conditions, which begin dilute and concentrate over time.
- High throughput methods are particularly important for providing statistically significant data on corrosion behaviour of commercial alloys.

6. Electrochemical studies on 304L and 316L in highly concentrated $MgCl_2$ solutions using 1D artificial pits and wire electrodes

6.1. Introduction

Atmospheric corrosion takes place in highly concentrated solutions, as the electrolyte is driven to maintain equilibrium with the water activity of the surrounding humidity [114]. The vast majority of electrochemical studies of corrosion in the literature use dilute solutions, so there is a need to further study atmospheric systems both qualitatively and quantitatively. Modelling of localised corrosion requires data, such as interfacial potentials, that is difficult to isolate experimentally due to the resistance contributions of the cell in which the work is conducted.

Solution concentration is dictated by relative humidity when at equilibrium. Saturated solutions correspond to the deliquescence humidity, i.e. the humidity that solid salt begins to take up water. In $MgCl_2$, 33% RH yields a saturated solution of 5 M $MgCl_2$ [114] in ambient temperatures. In order to understand atmospheric corrosion better, it is useful to look at electrochemical sweeps in highly concentrated solutions, as these are the concentrations experienced during corrosion.

Mo is a common alloying element in austenitic stainless steels that improves the corrosion resistance of stainless steels. It has been shown to affect the behaviour of both the initiation of pitting and propagation of pitting. There is significant, long-standing and ongoing debate over which effect is the more dominant contributor to its increased corrosion resistance [180]. Electrochemical sweeps using wire electrodes allow the investigation of initiation and passive current effects as well as giving details on repassivation. One-dimensional (1D) artificial pits allow

propagation and repassivation events to be isolated due to the well-defined geometry of the pit.

In this chapter, wires loops and 1D pits will be used to discuss the kinetics of initiation, propagation, and repassivation of 304L and 316L stainless steels in a range of $MgCl_2$ concentrations.

6.2. Results

6.2.1. One-Dimensional pitting

Figure 6-1 shows dissolution of both 304L and 316L pits undergoing dissolution in 2 M $MgCl_2$ from 1 V (SCE) in a downward sweep at 0.5 mV/s (Figure 6-1a). The initial transient period is brief for both alloys, with a salt layer precipitating after approximately 10 s (Figure 6-1b). Both pits reach stable pit stability, *ix,* values by 200 s (Figure 6-1c), approximately 190 s after the salt layer is first formed. One-dimensional pitting is achieved at a pit depth of approximately 70 μm, as calculated from Faraday's law, described in Chapter 2.

Once a salt layer has been precipitated the current densities, $i_{lim,}$ for both 304L and 316L are similar. This indicates that Mo does not have a significant effect on transport properties through the pit, and as such this cannot be considered a relevant mechanism for the increased corrosion resistance in Mo-rich stainless steel alloys[111, 112]. Towards the end of the potential sweep, 316L reaches its transition potential, E_T, before 304L, as shown in Figure 6-2. This indicates a higher interfacial potential in Mo-rich alloys that must be maintained to continue propagation. There does not appear to be a sharp repassivation potential for either alloy, but the linear extrapolation of the active dissolution and repassivation regions of the I-E curve show that the current density, and therefore the solution concentration, within which

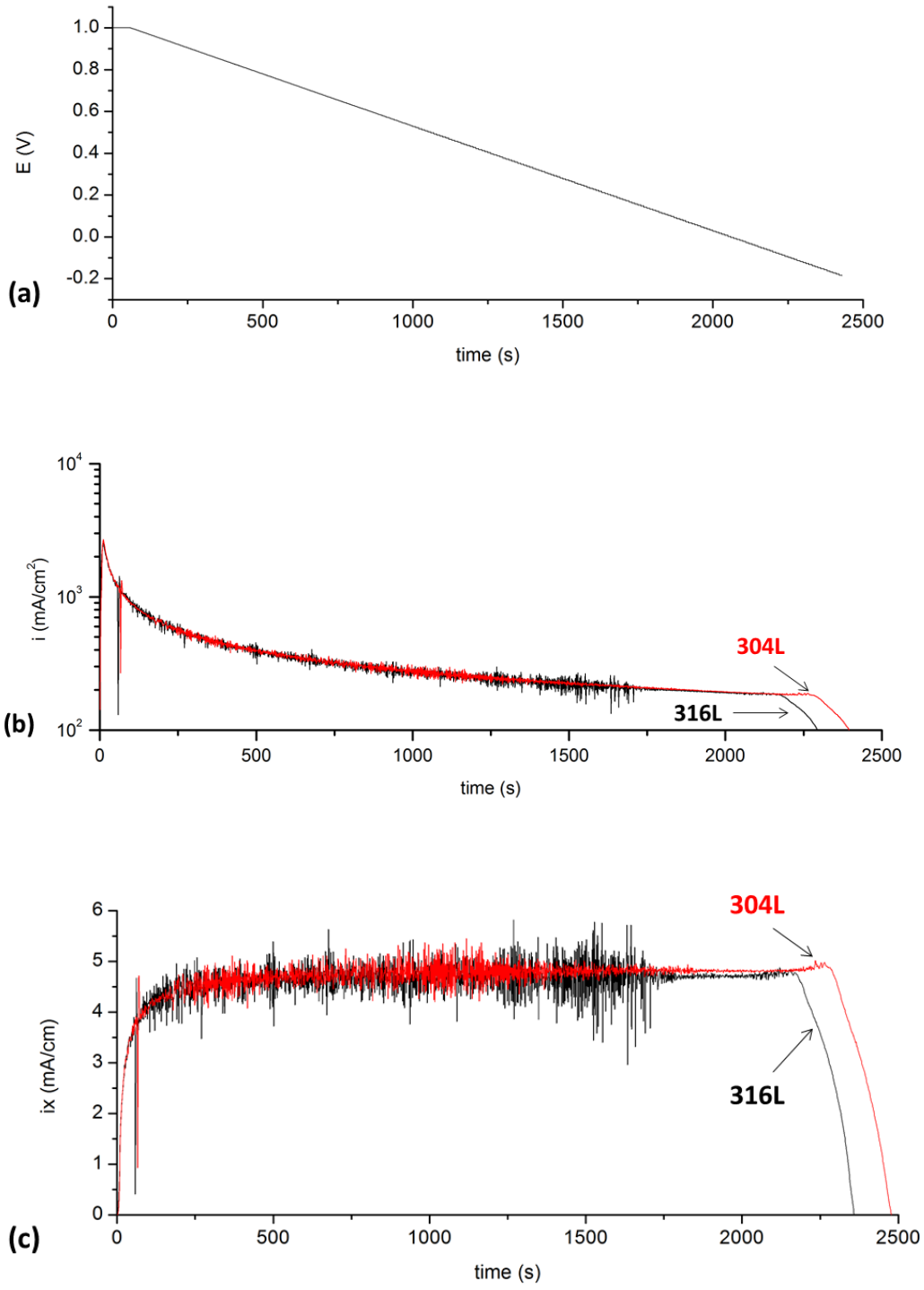

Figure 6-1 Preliminary 1D artificial pit experiments of 304L and 316L stainless steel pits in 2 M $MgCl_2$. (a) Potential sweep applied to pits, with initial growth period of 1 V (SCE) then decreasing at 0.5 mV/s until passivation. (b) Current density of pits of entire sweep until repassivation. (c) Pit stability product during pitting, showing when ix is constant, i.e. one dimensional pitting is attained. Wire diameters are approx. 50 µm.

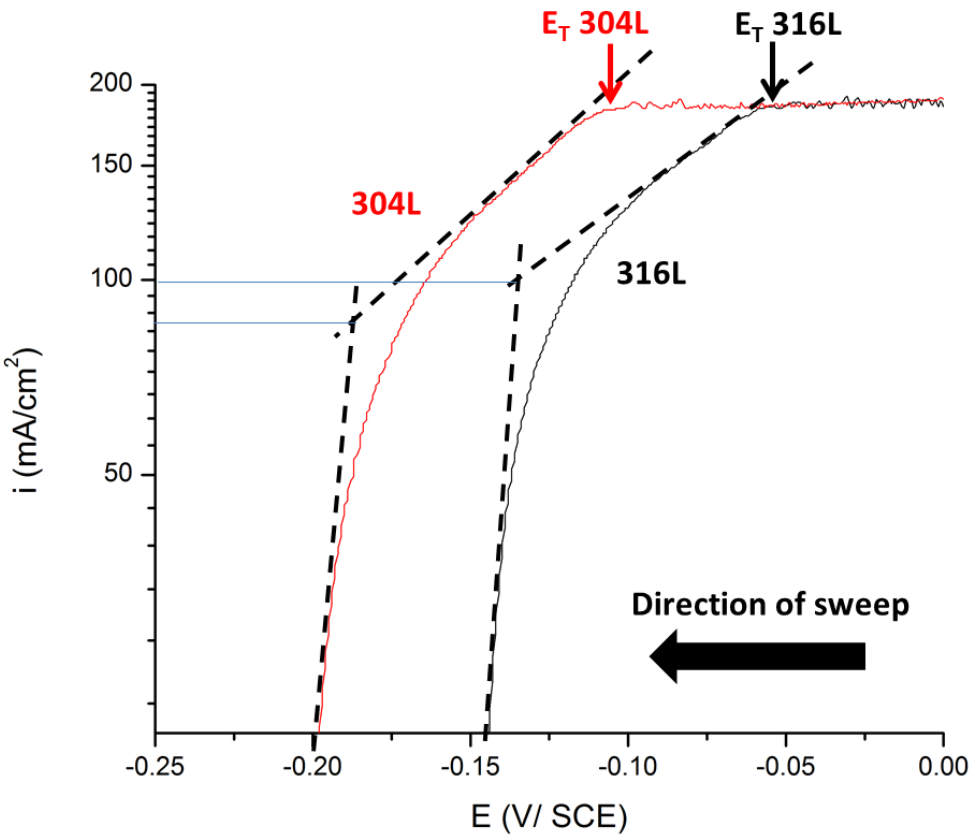

Figure 6-2 Artificial pits of 304L and 316L stainless steels in 2 M $MgCl_2$ being swept down at 0.5 mV/s. Transition potential, E_T, of both alloys is shown. Repassivation potential, E_{rp}, is less well defined in this solution but evidence of repassivation occurring is clear for both.

316L passivated was significantly higher than that of 304L, agreeing with repassivation kinetics literature that assert that 316L repassivates in more aggressive solutions [26, 77, 107, 192].

6.2.2.Zig-zag sweeps

Zig-zag sweeps in applied potential (Figure 6-3a) are used to show evidence of partial passivation on the corroding surface in one-dimensional pits. Slowly sweeping potential up and down during active dissolution should show near-identical current values during the down- and up-sweeps, after accounting for any increase in

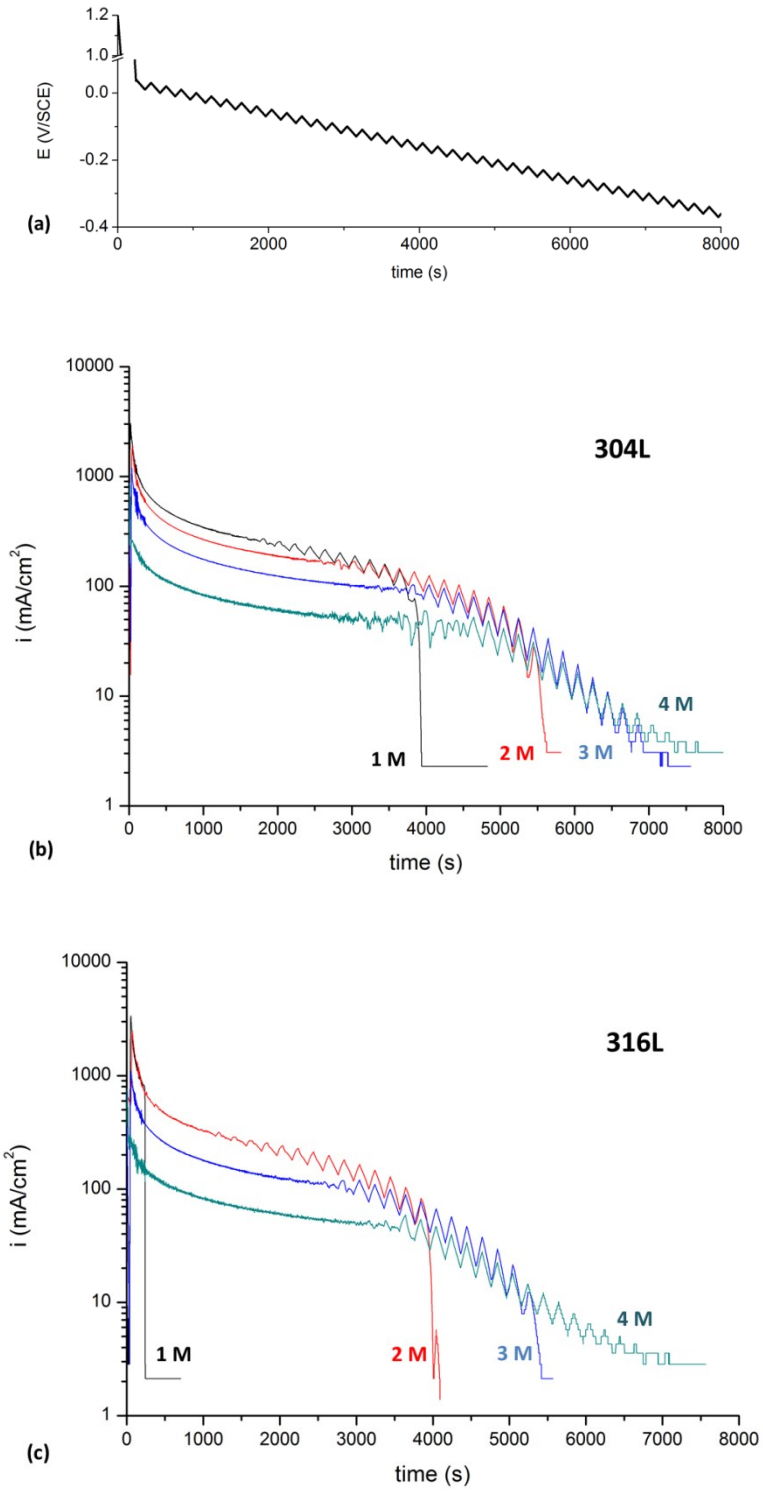

Figure 6-3 Zig-zag potential sweeps of one-dimensional artificial pits of austenitic stainless steels in a range of $MgCl_2$ concentrations. (a) Potential sweep program applied to artificial pits with a break in the y-axis to highlight zig-zag sweeps. (b) Current densities shown of artificial pits in 1 M – 4 M $MgCl_2$ in 304L and (c) 316L pits.

system resistance due to pit growth. If partial passivation occurs, path of the current during the up-sweep will deviate from the current during the down sweep, as less of the surface will be dissolving. Zig-zag sweeps will also isolate the transition potential, E_T, between diffusion-controlled and activation-controlled dissolution as current will not vary with Zig-zag changes in potential when under a salt layer. In short, the technique allows easy observation of both E_T and E_{RP} values.

Zig-zag potentials sweeps (Figure 6-3a) were conducted on one-dimensional pits of 304L (Figure 6-3b) and 316L (Figure 6-3c) stainless steels in 1, 2, 3 and 4 M $MgCl_2$, mimicking a range of atmospheric relative humidities. During dissolution under a salt layer, current density decreased with increasing $MgCl_2$ concentration, which has been observed previously in NaCl solutions [80, 193].

E_T, the potential where currents begin to show zig-zag behaviour, increases as chloride concentration of the bulk solution increases. This indicates an increased pitting stability. Rearranging *Equation 2-12*:

$$D\Delta C = \frac{i_{lim}x}{nF} \qquad \textit{Equation 6-1}$$

It can be deduced that the $D\Delta C$ must decrease as solution concentrations increases, as n and F remain constant. This was observed by Ernst and Newman [80] in NaCl in highly concentrated solutions. Current densities during active dissolution, i.e. between E_T and E_{RP}, converge and are approximately equivalent in different solution concentrations. This is only true if active dissolution is able to be maintained. This is not observed in 1 M $MgCl_2$ using 316L.

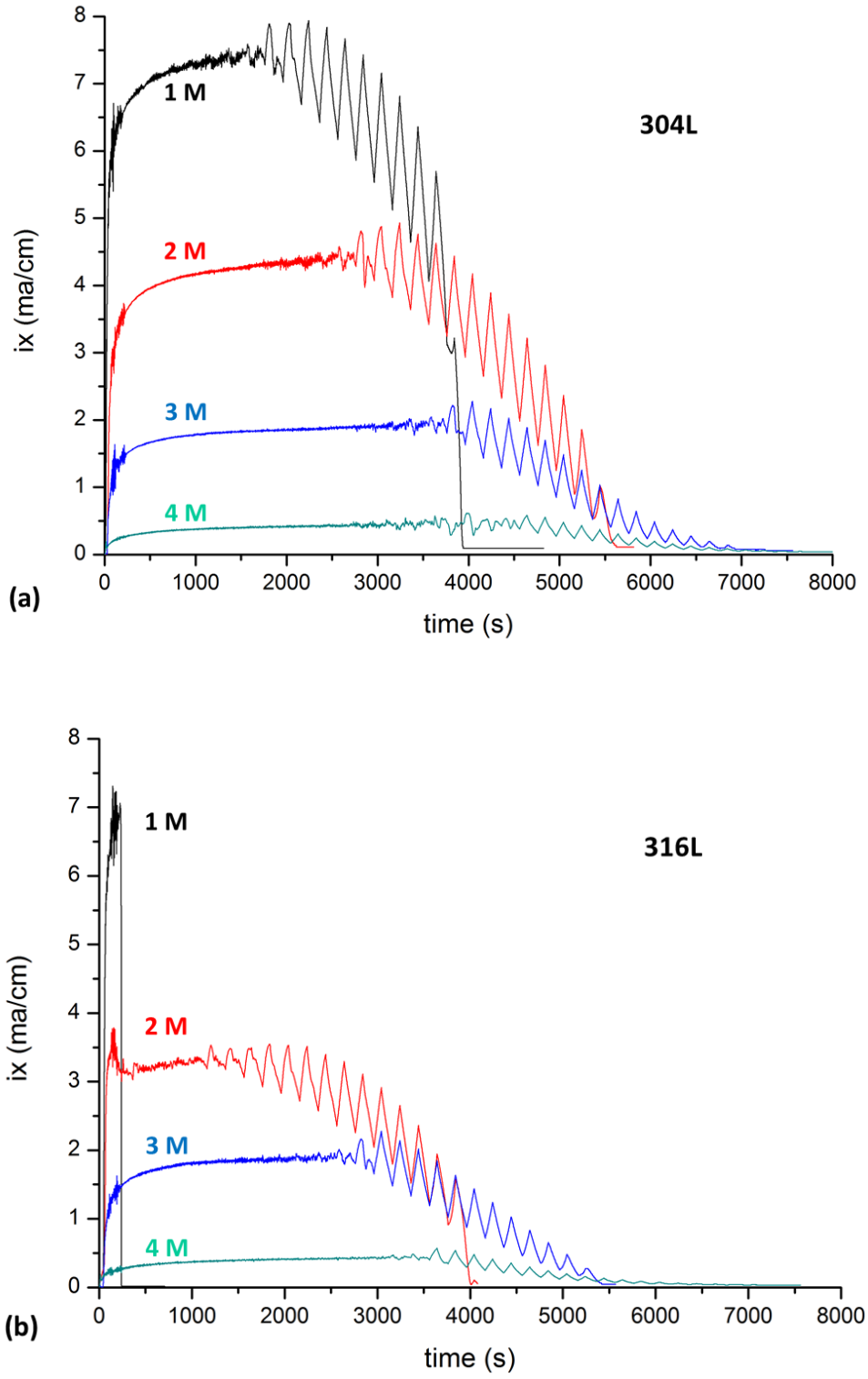

Figure 6-4 Pit stability products (ix) of artificial pits shown in Figure 6-3 made from (a) 304L stainless steel and (b) 316L stainless steel.

The pit stability products in different concentrations reach constant values at differing times, with 4 M $MgCl_2$ solutions requiring longer time to achieve (Figure 6-4a and b). This may be due to the speed at which the pit grows under a salt layer, as the reduced current density will reduce the pit growth and extend time needed to reach sufficient pit depth.

Repassivation behaviour is strongly dependent on solution concentration. In 304L, pits grown in 1 M and 2 M $MgCl_2$ solutions repassivate but those grown in 3 M and 4 M $MgCl_2$ do not and continue to show active dissolution until current approaches zero. 316L pits are more readily repassivated, showing repassivation in 1 M, 2 M and 3 M $MgCl_2$ solutions. However, 4 M $MgCl_2$ solutions show no sign of repassivation.

Comparing 304L and 316L directly as current density against time in 3 M $MgCl_2$ (Figure 6-5a) it can be seen that current density under a salt layer is very similar, again showing that Mo has very little influence on transport kinetics in solution. E_T is found at a much higher potential in 316L than in 304L. E_{RP} is not observed in 304L and the pit continues to show active dissolution at very low potentials. At potentials where both are under active dissolution, 316L has significantly lower current density than 304L. Figure 6-5b shows current density as a function of applied potential in 3 M $MgCl_2$. Dissolution under salt layer again appears to be equal between 304L and 316L in these data. E_T is approximately 100 mV lower in 304L than 316L, indicating an increase in activation potential caused by the addition of Mo. During active dissolution, Tafel slopes appear similar but this cannot be stated with accuracy as these data have not been IR-Drop corrected. 316L artificial pits does not show repassivation instantaneously but partial passivation is observed with

the reverse sweep forming "current loops" where the upward sweep has a lower current density than the downward sweep at the same potential. This occurs at higher current density than in 304L, showing repassivation occurring in much more aggressive solution

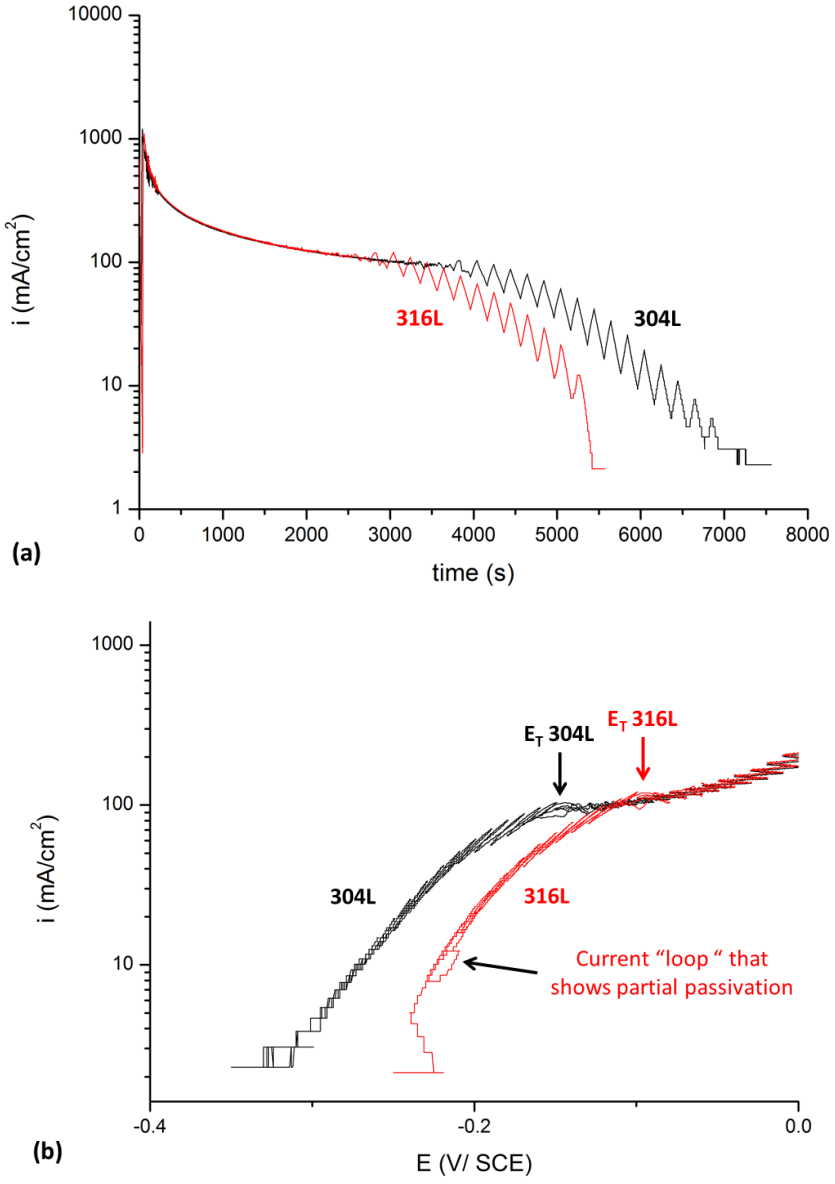

Figure 6-5 Comparison of one-dimensional artificial pits of 304L and 316L stainless steels, (a) current densities against time, and (b) current densities against applied potential

6.2.3. Electrochemical Impedance spectroscopy (EIS)

In electrochemical dissolution of metals, the key parameter that affects the rate of dissolution during corrosion is the interfacial potential, as this determines which reactions occur at the corroding interface. Determining the interfacial potential requires an investigation of sources of IR-drop, i.e. the sum of the loss of applied potential. This is a non-trivial task as direct measurement of sources of IR-drop is difficult. EIS is a technique that allows sources of IR-drop to be modelled and used to calculate the interfacial potential.

The challenge of using EIS in one-dimensional pits is the dynamic nature of pit growth. EIS is most commonly used on stable passive surfaces with fixed diffusion pathway lengths and surfaces. The continual growth of the pit during scans will affect how the electrochemical response is modelled. EIS often assumes a homogeneous surface whereas pitting corrosion is known to be heterogeneous with constant salt layer growth and dissolution, and transitioning between diffusion-limited, active dissolution and passive surfaces.

Acknowledging this, an attempt was made to isolate the *IR*-drop of the one-dimensional pit, and thus the interfacial corrosion to show the influence of solution concentration and molybdenum content on one-dimensional pitting of austenitic stainless steel.

6.2.4. Effect of pit depth growth

Figure 6-6a shows Nyquist plots of 304L stainless steel in 3 M $MgCl_2$ held at 0.1 V (SCE). 10 frequency sweeps were conducted, from 1 M Hz to 10 Hz with 10 frequencies used per decade for a total of 51 frequencies. Each sweep took 43 s and the pit was grown for 60 s between sweeps. It can be seen that the pit is not in

equilibrium, as is expected. Each plot shows a capacitance loop at high frequencies, an inductance loop at mid frequencies and another capacitance loop at low frequencies. As pit depth increases the radius of the capacitance loops increase, indicating an increased polarisation resistance in the pit and a higher corrosion resistance as the pit grows. This is confirmed by Figure 6-6b where Bode plots show increased absolute impedance values as pit depth increases indicating higher polarisation resistance. The negative gradient observed at low frequencies in the Bode plots, between 10^1 and 10^2 Hz, indicates a significant influence of diffusional processes occurring during this part of the sweep.

Frequency sweeps were also held in pits of the same depth with different applied potentials to investigate the effect different corrosion surfaces will have on EIS measurements. Figure 6-7a shows the influence of reducing applied potential at the same pit depth and transitioning from salt covered surfaces (0.1 V to -0.1 V SCE) to active dissolution (-0.15 V SCE) to repassivation (-0.2 V SCE). While under a salt layer, the Nyquist plot holds the same basic shape but with a reduction in polarisation resistance as applied potential reduces, coinciding with a reduction of the thickness of the salt layer. This is true in the Bode plots also (Figure 6-7b). In the cell held at -0.1 V, there appears to be a transition between the salt-covered regime and the active dissolution regime. This manifests in the loss of the second capacitance loop as low frequency in the Nyquist plot, and the reduction polarisation which can be best observed in the Bode plot. The region of negative gradient in the Bode plot between 10^1 and 10^2 Hz is now also linear. Nyquist and Bode plots for the

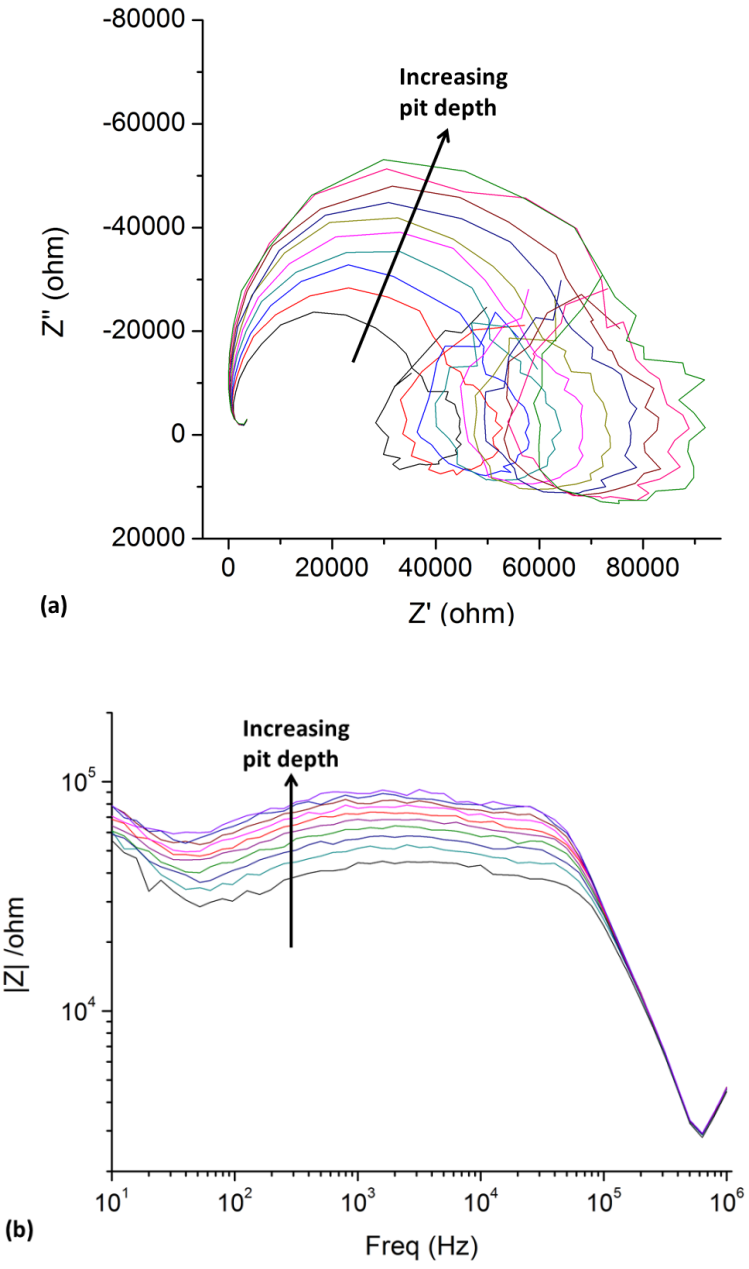

Figure 6-6 (a) Nyquist plots and (b) Bode plots of frequency sweeps of 304L stainless steel in 3 M $MgCl_2$ held at 0.1 V (SCE). Frequency Swept from 1 M Hz to 10 Hz, 10 frequencies per decade with 51 frequencies in total at 10 mV perturbation. First sweep conducted at depth of 40 µm. Sweeps each took 43 s and the pit was grown for 60 s between sweeps.

passivated pits when held at -0.2 V (SCE) are significantly different than both active- and salt-covered dissolution.

Figure 6-6 and Figure 6-7 show that both continuing pit growth and changes in applied potential affect the EIS electrochemical response which is then subsequently used to model interactions in the system, and that different corrosion surfaces respond to EIS perturbations in greatly differing ways. Recognising this, an attempt can be made to apply an IR-drop correction to one-dimensional pits of 304L and 316L stainless steels during a potential sweep.

A frequency of potential perturbations was selected to be at 30 kHz, as this was the frequency that gave the lowest phase angle in preliminary experiments on passive pit surfaces, as seen in Figure 6-8a, and was in agreement with previous work [57]. The condition of the interface during active dissolution changes significantly during pitting, so a decision was made to use the more stable results found on a passive surface. A typical equivalent circuit for a passive surface is shown in Figure 6-8b[57].

The Constant Phase Element (CPE) in Figure 6-8b represents the capacitance of the electrical double layer on the metal surface, with the polarisation resistance in parallel (R_{pol}) and solution resistance (R_s) in series. At approximately 30 kHz perterbations, R_{pol} will be short-circuited by the CPE term. This allows the R_S term to be calculated, which includes the resistance from the bulk solution, the pit solution, and the experimental cell[194].

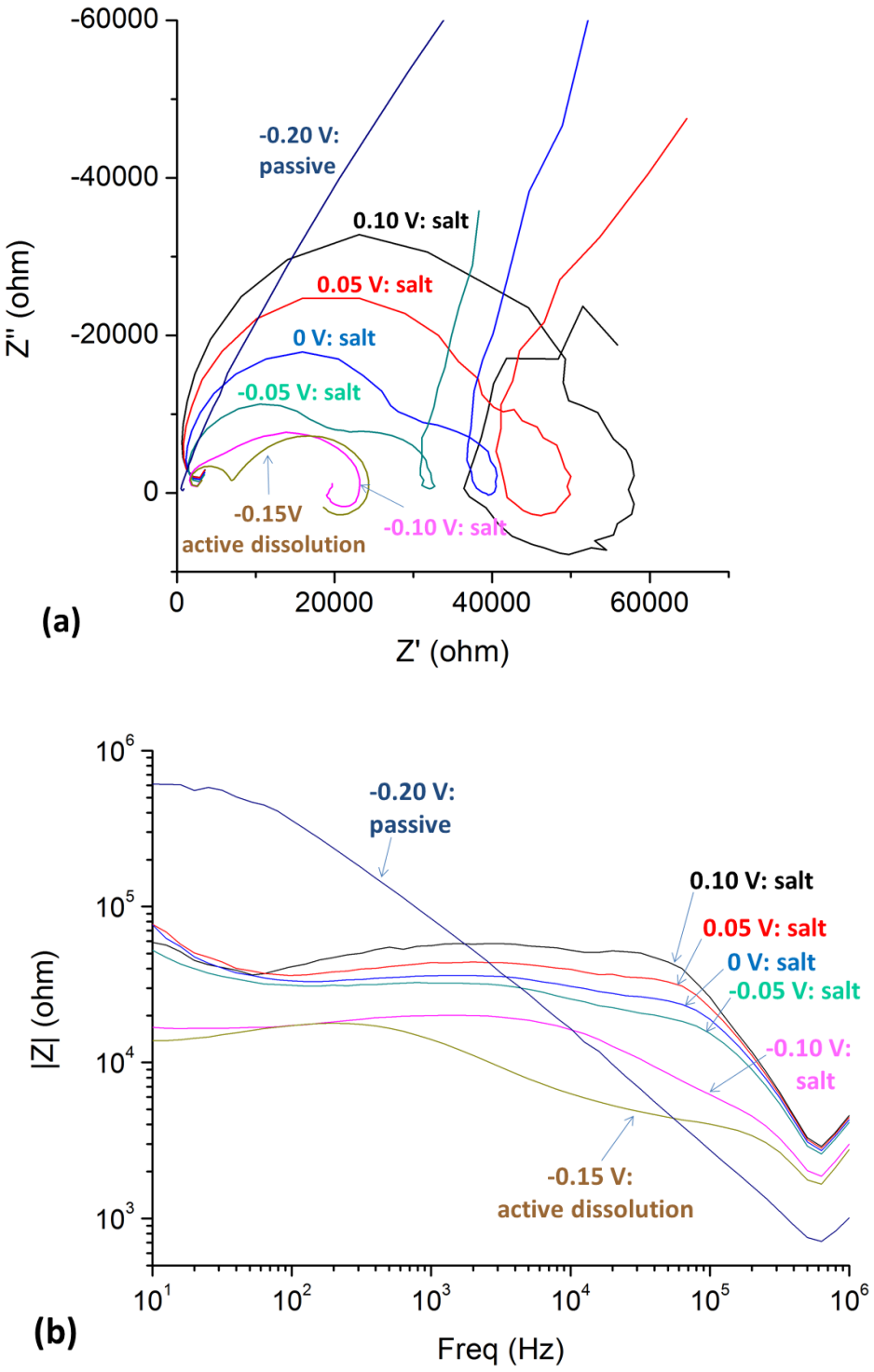

Figure 6-7 (a) Nyquist plots and (b) Bode plots of frequency sweeps of 304L stainless steel in 3 M $MgCl_2$ at pit depth of 65 µm over a range of applied potentials (SCE). Frequency Swept from 1 M Hz to 10 Hz, 10 frequencies per decade with 51 frequencies in total at 10 mV perturbation. Sweeps each took 43 s.

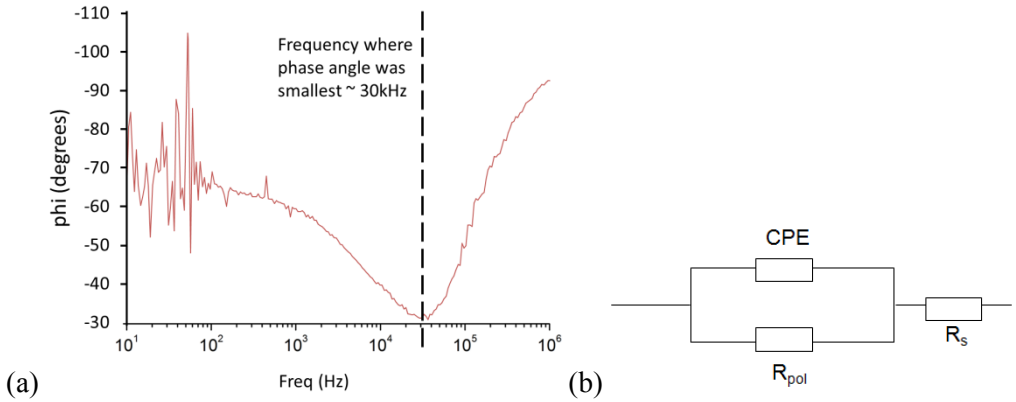

Figure 6-8 (a) Phase angle frequency sweep of 304L stainless steel in 3 M $MgCl_2$ at a depth of 65 µm at applied potential of 0 V (SCE) on a passive surface. Frequency Swept from 1 M Hz to 10 Hz, 10 frequencies per decade with 51 frequencies in total at 10 mV perturbation. (b) Equivalent circuit used to obtain values for R_s in series with the constant phase element modelling the electrical double layer.

Figure 6-9 shows IR-drop corrected current voltage characteristics for one-dimensional pits whose current densities are shown in Figure 6-3. There is a clear difference in behaviour between dissolution under a salt layer and during activation control. In conditions where repassivation is observed, "current loops" occur when potential drops to where it approaches passivation. This is an indication of partial passivation behaviour, as the current does not retrace its downward path during the zig-zag sweep. The region of active dissolution is also curved in regimes where repassivation occurs. Where repassivation does not occur, Tafel β values are able to be measured and are shown on Figure 6-9c and d.

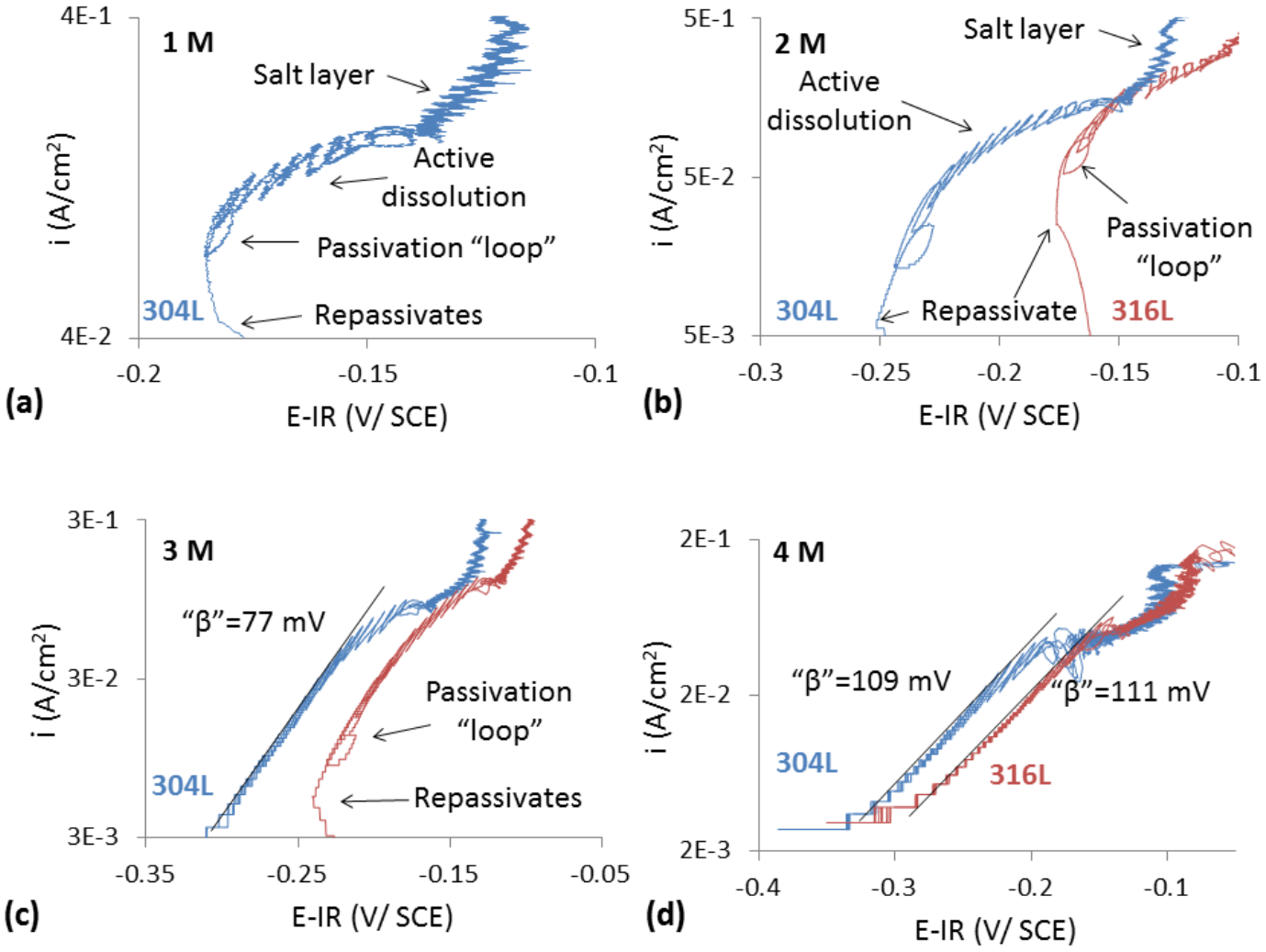

Figure 6-9 Current-Voltage characteristic curves of 304L and 316L stainless steel one-dimensional pits after IR-drop correction using 30 kHz frequency. (a) 1 M $MgCl_2$, (b) 2 M $MgCl_2$, (c) 3 M $MgCl_2$ and (d) 4 M $MgCl_2$ using potential program found in Figure 6-3a.

6.2.5. Wire Electrochemistry

Cyclic voltammetry is a common method of investigating the corrosion behaviour of an alloy in a particular solution. Initially, the potential is held below the open circuit potential (OCP) then increased at a constant rate. Once the alloy has shown signs of corrosion, particularly pitting on passive surfaces, the sweep is reversed and potential is reduced at a constant rate until it drops below OCP again. Wires are often used as they have a broadly regular geometry and consistent surface finish. By conducting cyclic voltammetry on wires of 304L ans 316L stainless steels in various concentrations of $MgCl_2$ solutions, it is hoped that more insight will be given on the corrosion behaviour of stainless steels at humidity reduces.

The upward potential sweeps of 304L and 316L stainless steel wires in a range of $MgCl_2$ concentrations are shown in Figure 6-10. 316L has significantly higher E_{pit} when compared to 304L (Table 6-1), which is expected as this is a well-established phenomenon in the literature, with E_{pit} defined as the potential when current density surpasses 0.1 $mAcm^{-2}$. There is a large difference in E_{pit} between the alloys when the concentration is at 3 M $MgCl_2$. This large variation in E_{pit} corresponds to significant changes in metastable pitting behaviour observed in both alloys as concentration increases. In 304L, metastable pitting is observed at 1 M and 2 M $MgCl_2$ but is not apparent at concentrations above this. In 316L, metastable pitting is also observed at 3 M $MgCl_2$, but not at higher concentrations. The loss of metastable pitting coincides with a change in pitting current profile, which is clear when current is plotted on a linear scale as seen in Figure 6-11. In 1 M $MgCl_2$, metastable pitting is observed followed by a sharp increase in current density. However, in 3.5 M $MgCl_2$ there is no sharp increase and instead a gradual curve up in current density until pitting has established. There appears to be some evidence of noise in current on the curve upwards, which may be related to metastable pitting events but this is unclear.

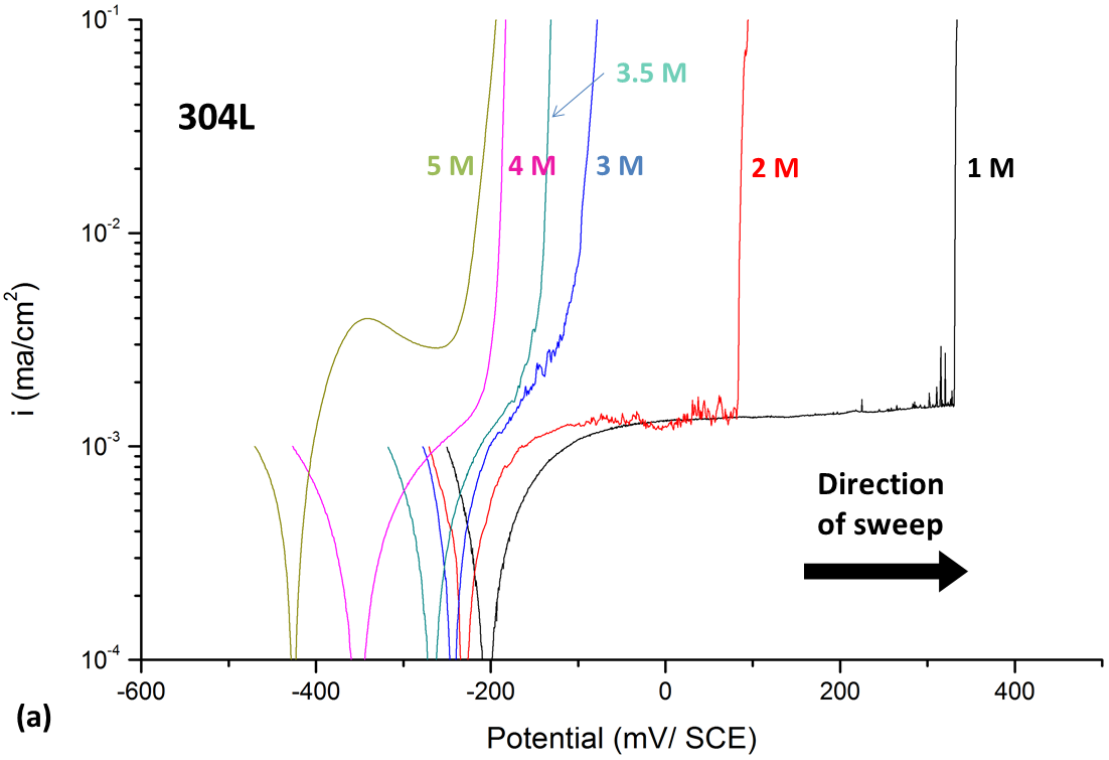

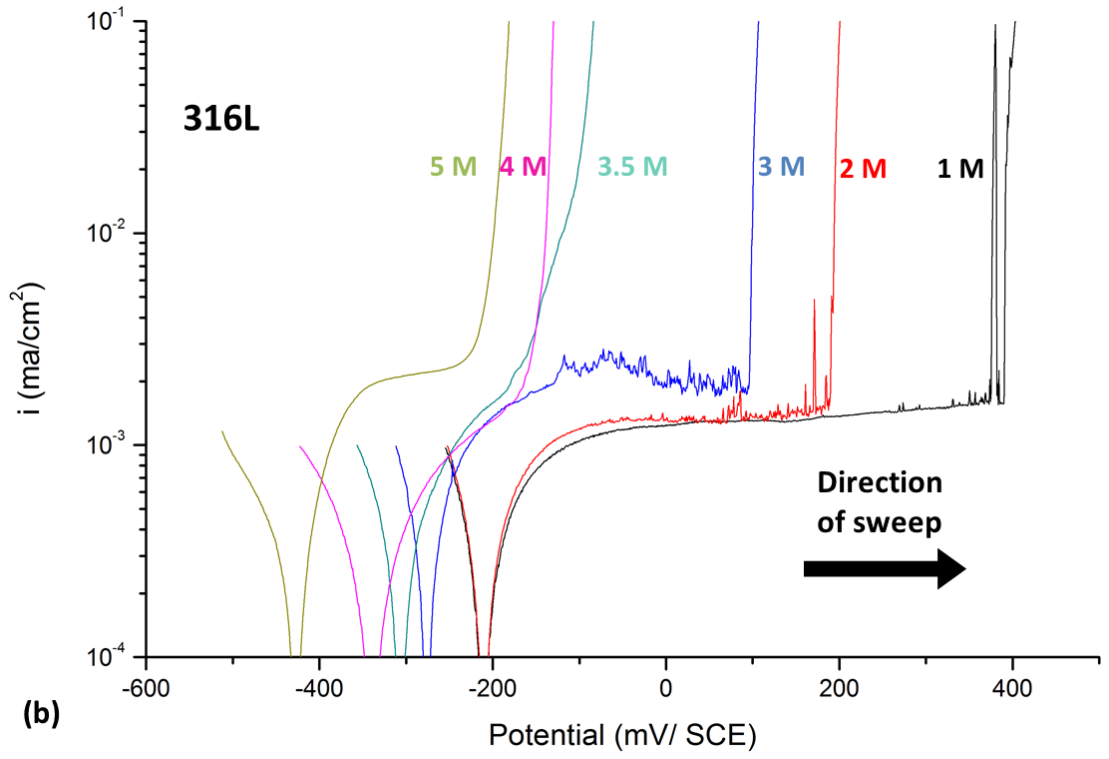

Figure 6-10 Upward potential sweeps of (a) 304L and (b) stainless steels wires in varying concentrations of $MgCl_2$. Wires were held at 100 mV below OCP for 900 s in each case.

Table 6-1 Pitting Potential (E_{pit}) values for 304L and 316L in various concentrations of $MgCl_2$. Average of three sweeps for each concentration.

$MgCl_2$ concentration (M)	E_{pit} of 304L (mV/ SCE)	E_{pit} of 316L (mV/ SCE)	Equivalent Rel. Humidity
1	333	402	94%
2	94	201	83%
3	-78	99	68%
3.5	-138	-83	59%
4	-183	-130	50%
5	-250	-205	34%

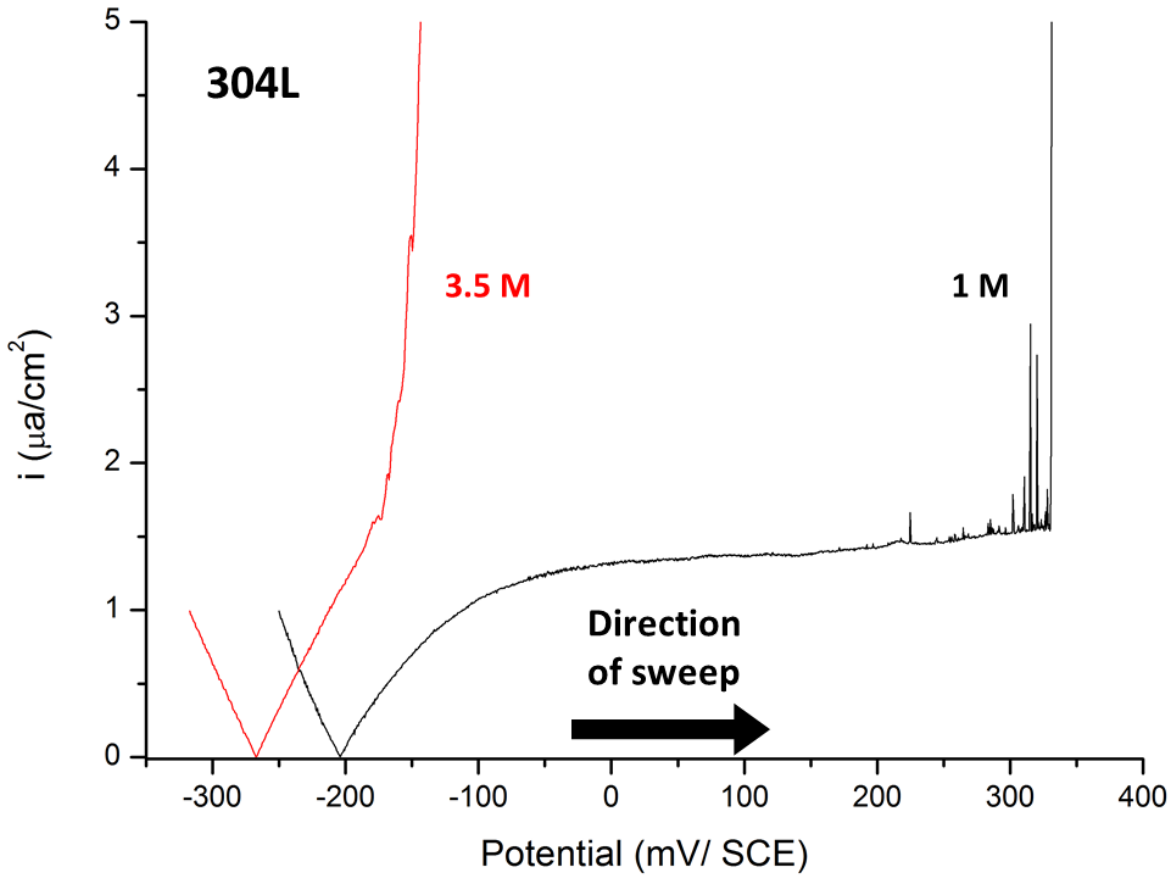

Figure 6-11 Upward potential sweeps on 304L stainless steel in 3.5 M $MgCl_2$ and 1 M $MgCl_2$. Swept at 0.5 mV/s. Plots on linear scales.

Downwards sweeps were also collected on these wire samples, with data for 304L and 316L wires shown in Figure 6-12. The repassivation behaviour changes in both alloys as concentration increases. In 1 M $MgCl_2$, for both alloys, the current is seen to drop periodically before falling sharply. This behaviour becomes less dramatic as concentration increases. At high concentrations, the repassivation behaviour of both alloys follows mostly a smooth curve. Repassivation potentials, E_{rp}, are shown in Figure 6-13 and Table 2 where E_{rp} is defined as when current drops below the upward current. Values of E_{rp} appear to converge as concentration increases.

The change in passivation behaviour is more apparent when plotted on a linear scale, as shown in Figure 6-14. While repassivation in 1 M $MgCl_2$ shows sharp drops in current, indicating competition threshold events inside the pit, repassivation in concentrated solutions such as 3.5 M $MgCl_2$ show a smooth "cessation" of current as potential is reduced.

Comparing full sweeps side-by-side shows the effect solution concentration has on the morphology of the cyclic voltammetry. Figure 6-15 shows cycles of 304L and 316L in (a) 2 M, (b) 3 M, and (c) 3.5 M $MgCl_2$.

Potential sweeps were also conducted on 304L stainless steel plate (Figure *6-16*a), prepared by grinding with 800 grit sanding paper, similar to atmospheric corrosion experiments in later chapters. For 1 M and 4 M $MgCl_2$ solutions, electrochemical behaviour looks very similar to that of the wire electrochemistry found in Figure 6-10 and Figure 6-12. The sudden increase in pitting behaviour and decrease in repassivation behaviour observed in 1 M $MgCl_2$ sample indicates threshold events. Inspection of the 1 M $MgCl_2$ plate (Figure 6-16b) showed no obvious signs of pitting or attack anywhere on the surface, indicating that this was most likely a crevice attack between the plate and the resin.

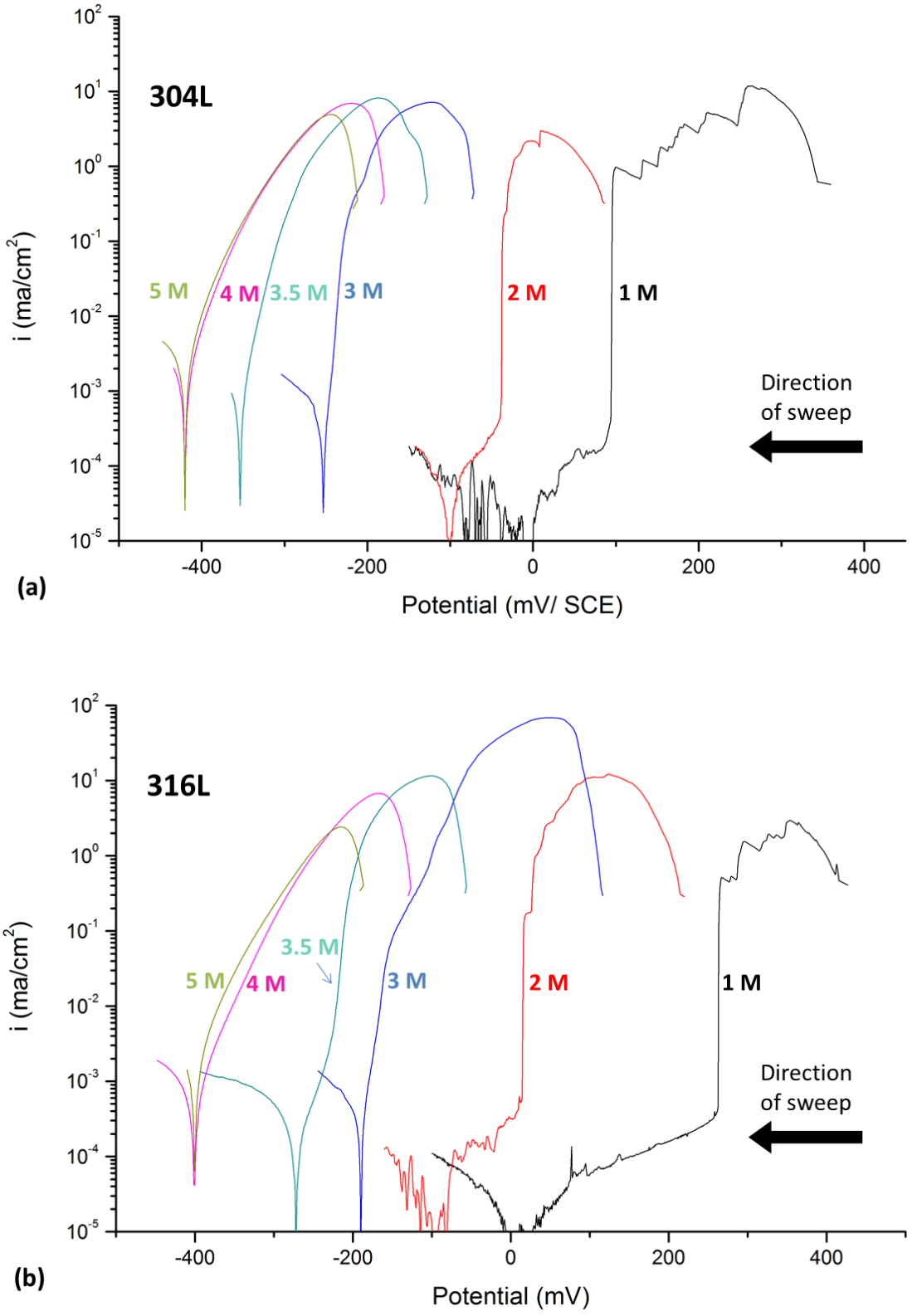

Figure 6-12 Downward potential sweeps of (a) 304L and (b) 316L stainless steel wires in varying concentrations of MgCl2. Reverse sweep started at 0.1 mA/cm2

Table 6-2 Repassivation Potential (E_{rp}) values for 304L and 316L in various concentrations of $MgCl_2$. Average of three scans per solution

$MgCl_2$ concentration (M)	E_{rp} of 304L (mV/ SCE)	E_{rp} of 316L (mV/ SCE)	Equivalent Rel. Humidity
1	94	262	94%
2	-84	13	83%
3	-250	-134	68%
3.5	-345	-261	59%
4	-416	-393	50%
5	-420	-395	34%

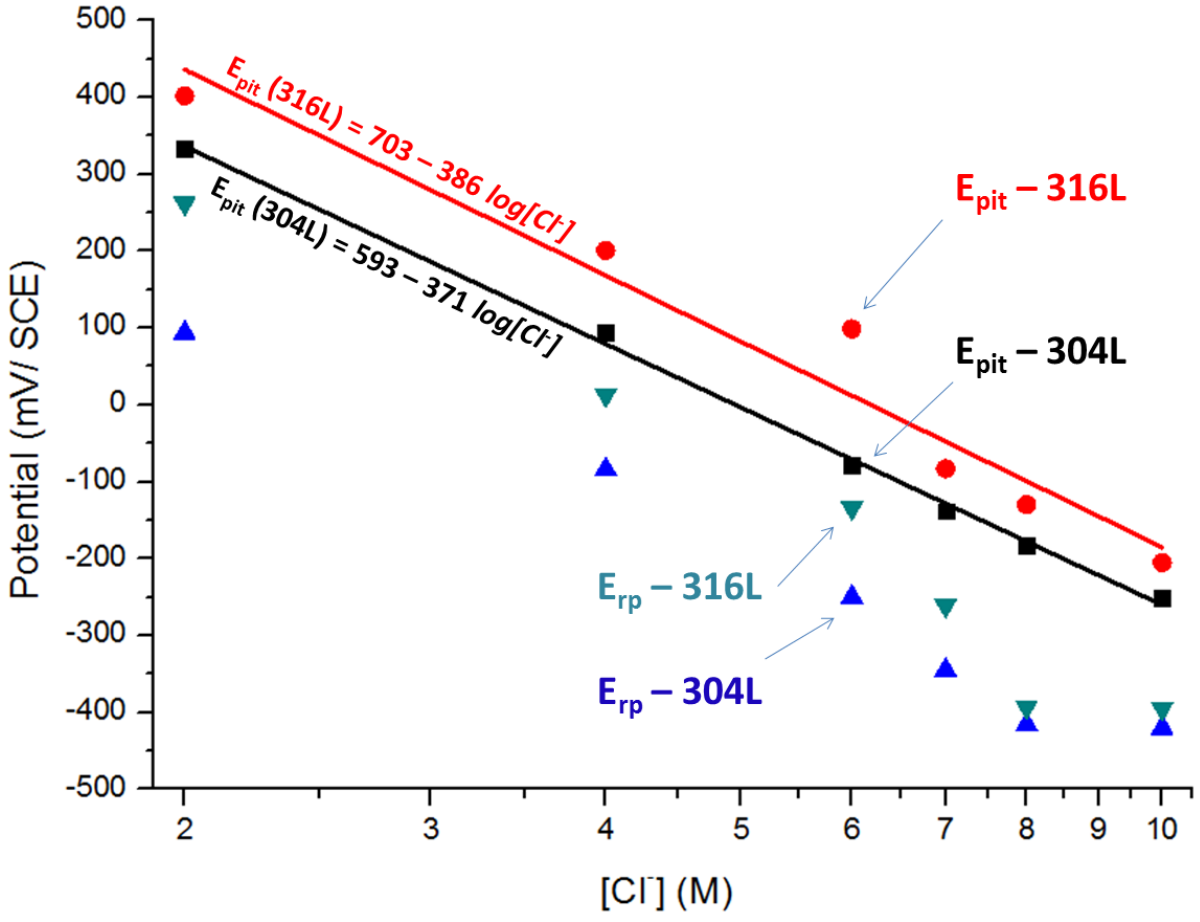

Figure 6-13 Pitting Potential (E_{pit}) values for 304L and 316L stainless steel wires in varying concentrations of Cl^-. E_{pit} and E_{rp} values taken from Figure 6-10 and Figure 6-12 respectively. E_{pit} defined as 1 mA/cm^2, E_{rp} defined as point current drops below upward passive current.

However, the 4 M $MgCl_2$ sample (Figure 6-16) showed attack in dozens of sites all over the plate surface. Closer inspection of the plate showed a single deep pit (Figure 6-16d) and large regions of an etched attack (Figure 6-16e) where grain boundaries and stringers and be seen in the rolling direction of the plate. This etched attack was not observed on the 1 M $MgCl_2$ plate (Figure 6-16f).

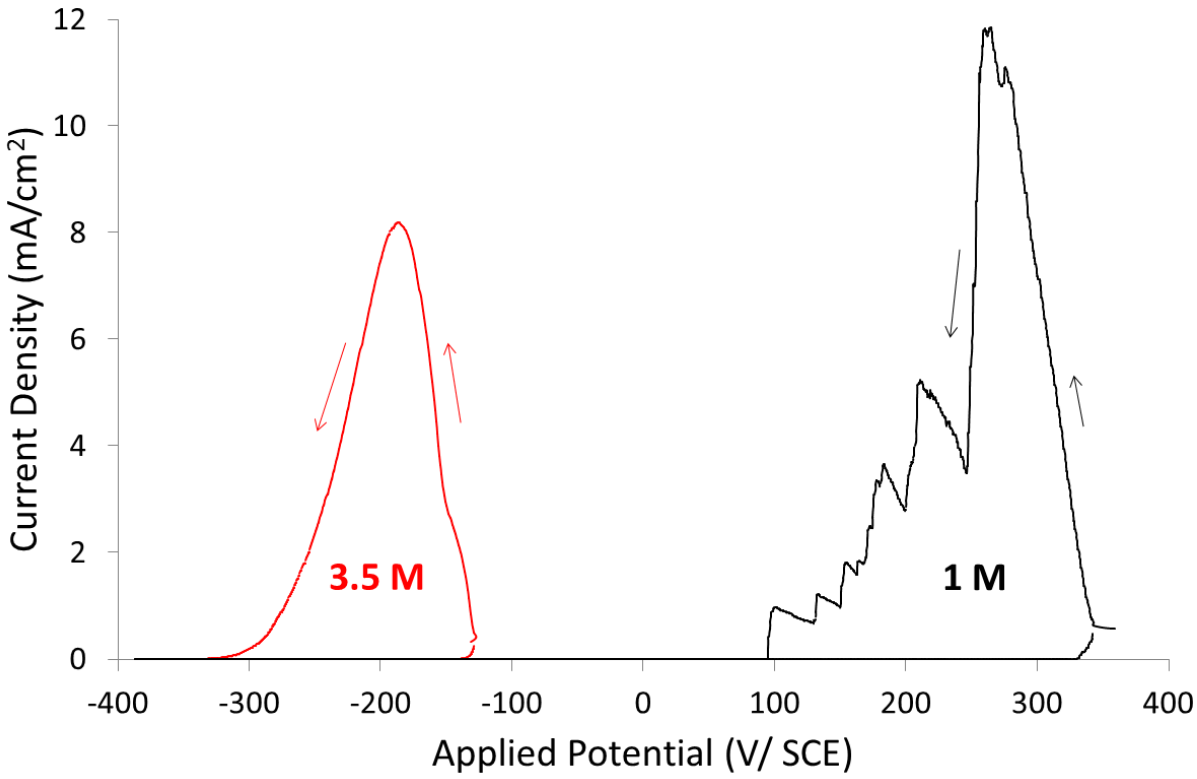

Figure 6-14 Downward potential sweeps of 304L stainless steel wires in 1 M and 3.5 M $MgCl_2$. Sweep was at 0.5 mV/s

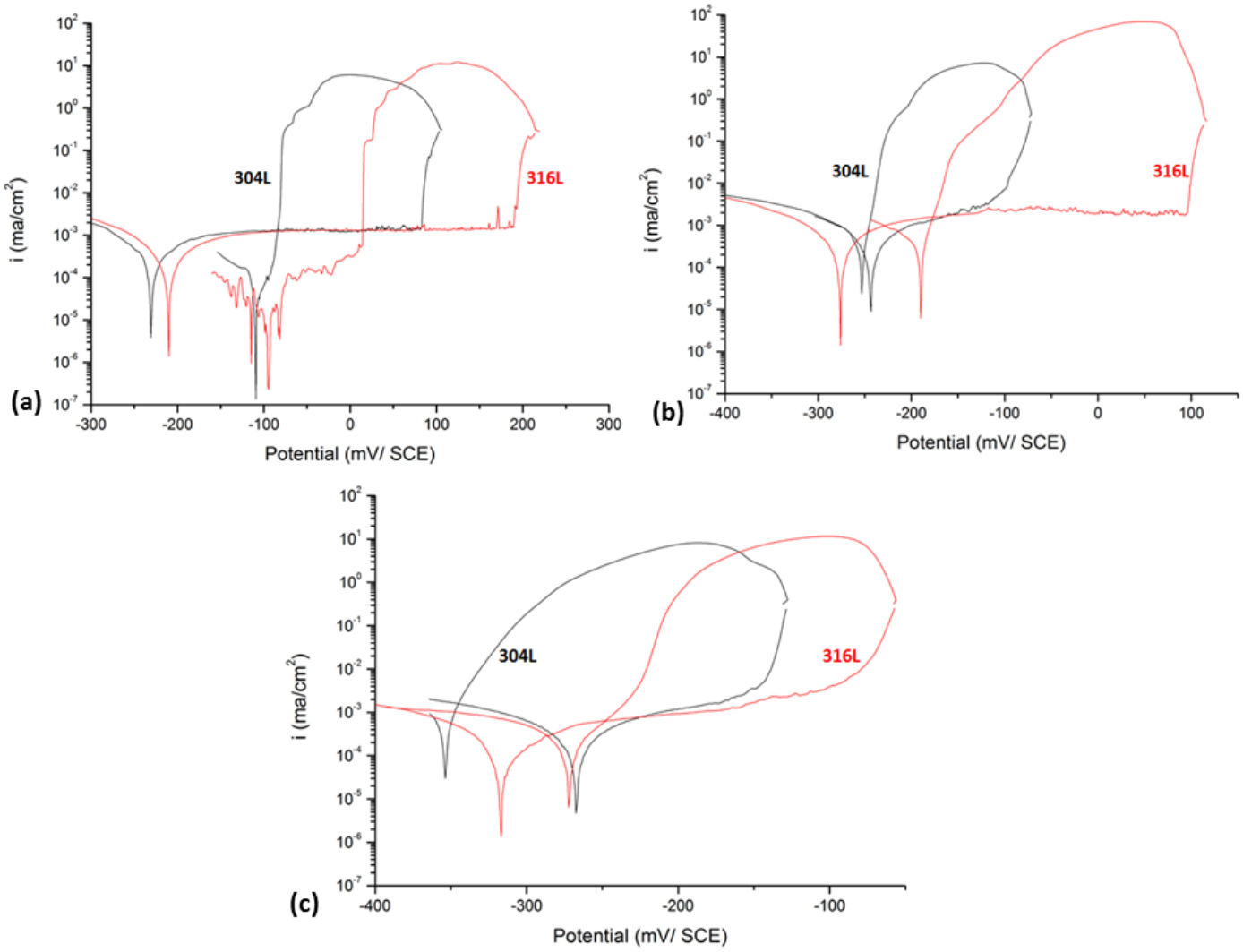

Figure 6-15 Polarisation curve on 125 µm diameter wires of 304L and 316L stainless steel in (a) 2 M, (b) 3 M and (c) 3.5 M MgCl2 . Wires were held at 100 mV below OCP for 900s and then swept at 0.5 mV/s. Wires were ground with 2500 grit paper and rinsed with DI water

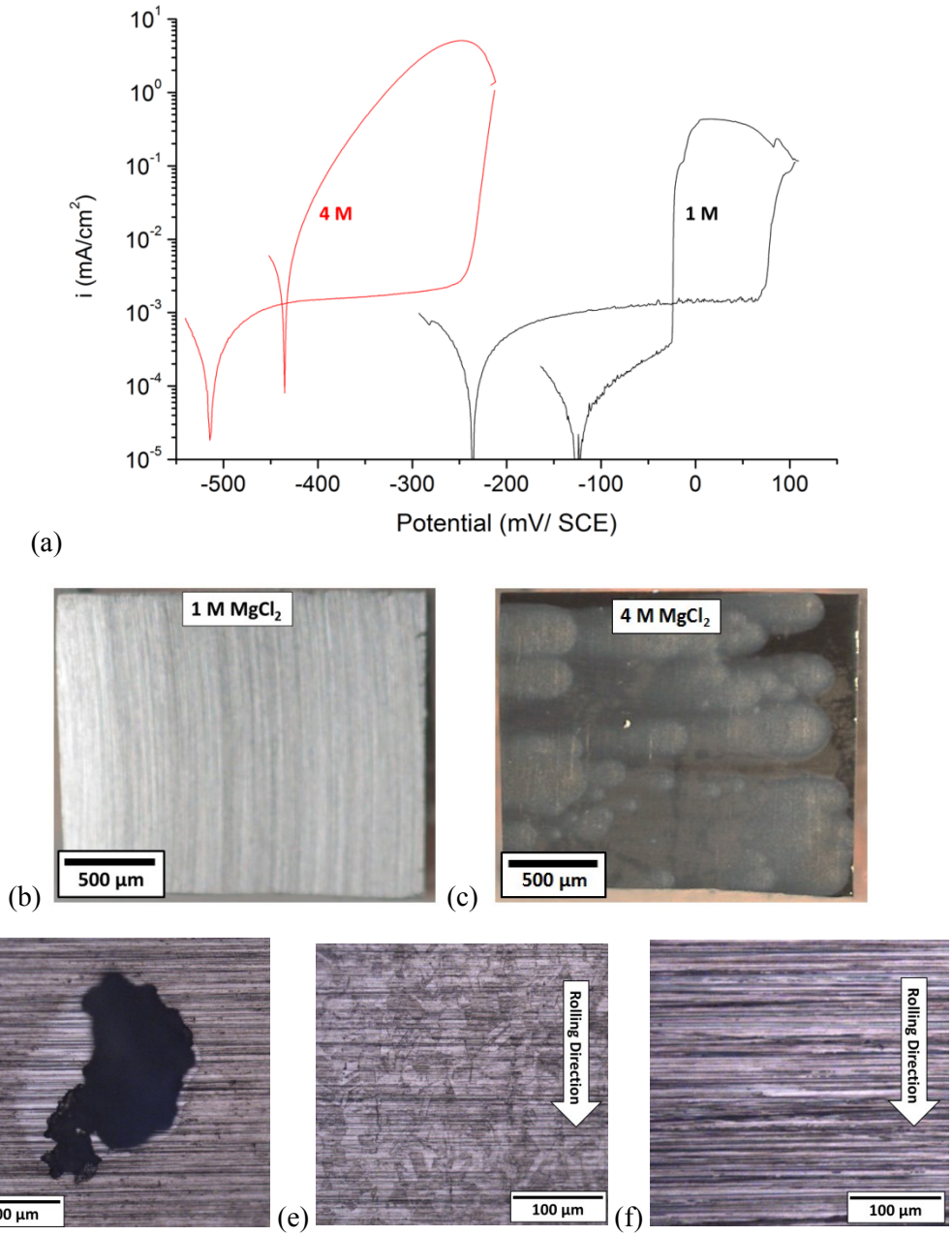

Figure 6-16 304L plates immersed in 1 M and 4 M $MgCl_2$. (a) Potential sweeps showing similar behaviour as to wire experiments above, with the sample in 1 M $MgCl_2$ showing sharp pitting potential and repassivation behaviour, and 4 M $MgCl_2$ sample showing gradual curve upwards when pitting and "cessation" behaviour when passivating, (b) 1 M $MgCl_2$ sample surface with no visible pits, indicating that attack was most likely crevice corrosion, (c) 4 M $MgCl_2$ sample with dozens of attack sites on the surface, (d) Single pit found on surface of 4 M $MgCl_2$ sample, and (e) surface etching found across the surface of 4 M $MgCl_2$ sample showing crystallographic etching MnS stringers orientated in rolling direction, (f) surface of plate after corrosion in 1 M $MgCl_2$

6.3. Discussion

6.3.1. Pitting

The pitting potential, E_{pit}, is considered to be the potential at which a pit can stably propagate [13]. Pitting potential is not a single thermodynamically related value but is broadly considered to be a function of the breakdown of a passive film by attack of surface inclusions or some other mechanism [22]. E_{pit} is thus specific to a combination of the alloy, the environment, and surface treatment [195] in which the experiment is conducted. The need for propagation separates it from metastable pitting events [48].

E_{pit} values on wire experiments are seen to vary with solution concentration for both 304L (Figure 6-10a) and 316L (Figure 6-10b) alloys and decrease approximately linearly with log of increasing solution concentration (Figure 6-13). Galvele [27] suggested using a one-dimensional diffusion-based model of corrosion over a range of different alloys that E_{pit} decreases with increasing Cl concentration with the relationship

$$E_{pit} = E^0_{pit} - A\ log[Cl^-] \qquad \textit{Equation 6-2}$$

Where E^0_{pit}, A are constants. Galvele estimated A to be 59 mV/decade, calculated from $2.303RT/F$ where R is the gas constant. Leckie and Uhlig [92] noted a logarithmic dependence on Cl^- concentration in dilute NaCl solutions between 0.01 and 1 M for 18-8 stainless steel, yielding A of 85 mV/decade. Laycock and Newman [13] on 302 stainless steel noted A of 93 mV/decade in NaCl between 0.1 and 1 M and an increase in E_{pit} for 316 stainless steel of 70-100 mV.

In this work *A* was significantly higher, for both 304L (386 mV/decade) and 316L (371 mV/decade). Most highly cited papers that look at the influence of [Cl^-] on E_{pit}, like those mentioned above, do so at low bulk solution concentrations and do not consider highly concentrated conditions. In her thesis, Mi [12] examined 304 stainless steel in $MgCl_2$ with a [Cl^-] range of 0.1 to 10 M, and found a change in trend between low and high concentrations. At concentrations of 0.1 - 2 M [Cl^-], *A* was between 110 and 200 mV/decade. In solutions at concentrations 2 - 10 M [Cl^-], *A* increased significantly to values above 400 mV/decade.

The increase in *A* at high concentrations of chloride ions is thought to be, in part, attributed the influence of the common-ion effect at high concentrations. This can decrease solubility of metal ions released during dissolution, increasing pitting stability by allowing aggressive conditions to be maintained at lower potentials. There is also an underlying assumption with the Galvele model that Cl^- does not participate in complexation of metal cations which has been shown not to be accurate in stainless steels [196]. Pardo *et al.* [197] also saw significant reductions in E_{pit} in concentrated solutions, though with particular attention paid to temperature variations. Variation in E_{pit} within an alloy is consistent with the literature [198] as variations in sample preparation, e.g. surface roughness after grinding and time spent passivating before experiment [13], are known to affect pitting potential.

Pitting events were detected electrochemically and the shape of the current-potential diagrams varied significantly depending on solution concentration. The sudden pitting events at concentrations 1 M and 2 M $MgCl_2$ (Figure 6-10) agree with typical hemispherical pitting behaviour discussed in the literature [20] that result in a single pit being formed. In highly concentrated solutions, e.g. between 3.5-5 M $MgCl_2$ in both alloys, this pitting occurs at a far less defined potential. Plate experiments at

4 M $MgCl_2$ (Figure 6-16) show that although there is a single pitting event at these conditions there is also significant superficial attack across the plate surface at dozens of sites. There was also observed heavy etching on the plate surface where grain boundaries and other metallurgical features can be seen. This superficial attack shows great similarity to the "earing" attack of the shallow dish region seen in atmospheric corrosion of stainless steels under droplets [136, 162] which has been shown to be an initial attack that leads onto pitting behaviour [126]. This concerted attack on the plate surface may explain why no metastable pitting is seen in concentrated solutions. The decrease in diffusivity and saturation concentration of the solution may make a large number of inclusions be able to maintain an aggressive local solution [49] and attack the underlying metal matrix.

Speciation and transport properties are known to be affected in concentrated solutions, particularly ion-ion and ion-neutral molecule interactions [199, 200]. Water activity, or the ease of with which water may be utilised, is also important in understanding these transport processes. Smart and Bockris [201] were able to show a downward linear relationship between the water activity of concentrated solutions and i_{corr} values.

Work has been conducted investigating the concentrations thresholds for both initiation and repassivation for atmospheric corrosion on stainless steels [125]. On 304L, Nam *et al*. found "pitting" to start at between 47-58 %RH, which corresponds to 3.6 – 4.1 M $MgCl_2$, and continue at lower humidites. Repassivation began at higher relative humidities 56-70 %RH, corresponding to 2.9- 3.7 M $MgCl_2$. It is not surprising that initiation requires more aggressive solution conditions than propagation considering the specific chemical requirements needed for the

dissolution of sulphide inclusions and the local chemistry that is needed to allow a pit to stabilise.

6.3.2. Repassivation

The repassivation potential, E_{rp}, of stainless steels is generally considered to be the potential where a critical chemistry is no longer able to be maintained to keep the corroding surface active [202]. As seen with E_{pit}, E_{rp} values of wire samples declined linearly with increase in concentration (Figure 6-13) where E_{rp} values for 304L and 316L appear to converge as concentration approaches saturation. One-dimensional pitting also showed very low repassivation potentials, where zigzag potential sweeps showed active dissolution until the experiment was halted (Figure 6-3). This has been observed previously [197, 198].

As with pitting, the repassivation not only occurs at lower potentials but the behaviour itself changes as concentration increases. Repassivation reactions require a thermodynamic preference for the stability of reduction reactions at the corroding interface, which is generally considered to be a sharp threshold below which allows passivation [171]. The adsorption of free water in close-to-neutral environments that allows deprotonation and passive film growth may not be possible in highly concentrated chloride solutions. The increased ion concentration makes greater demands of the water in solution to participate in solvate shells, restricting access and hence water activity to the corroding interface. Highly concentrated solutions also reduce pH to between 4-5 pH, destabilising any passive oxide that does manage to grow on the surface. These factors allow the corroding pit to remain active at very low potentials and “cease” corroding when the corroding interfaces activation energy can no longer be surpassed rather than “passivate” due to competing chemical processes.

6.3.3. Passive Current Density

Passive current increases significantly with the increase of $MgCl_2$ concentration, particularly in the range above 4 M. This has been observed previously in deaerated wire experiments in 304L [12, 126]. In 304L, passive current density roughly doubles between 2 M and 3 M $MgCl_2$ (Figure 6-10a). This close to what was found in 304L in deaerated $MgCl_2$, with a doubling of passive current density occurring between 3 and 3.2 M $MgCl_2$. This increase in passive current is more pronounced in 316L as the resistance to pitting of this alloy increases the range where passive current dissolution takes place (Figure 6-10b).

The rate of passive current dissolution may be related to the beginnings of atmospheric corrosion seen under droplets of $MgCl_2$, where shallow dish regions [136] are seen to occur initially before pitting continues. Rough approximations have been made for the amount of metal dissolution needed for the formation of shallow dish regions in highly concentrated solutions [126]. The current density for vertical growth of the shallow dish can be estimated from Faraday's law (from Chapter 2):

$$x = \frac{QM_W}{AnF\rho} \qquad \textit{Equation 2-13}$$

using ρ of 7.9 g/cm^3 and n of 2.2 for 304L, typical depth of shallow dish regions, x, of 10 μm, with the majority of growth occurring in the first two hours. This yields a current density of ~4 μA/cm^2, which is in the same order of magnitude as the passive current densities observed at high chloride concentration (i.e. above 3.5 M $MgCl_2$).

This can be further explained using a mixed-potential theory and an Evans' diagram (Figure 6-17). An increase in $MgCl_2$ concentration will not only increase current density, but will drive dissolution at lower potentials. This will allow an increase in passive current density more readily at low RH when under atmospheric conditions.

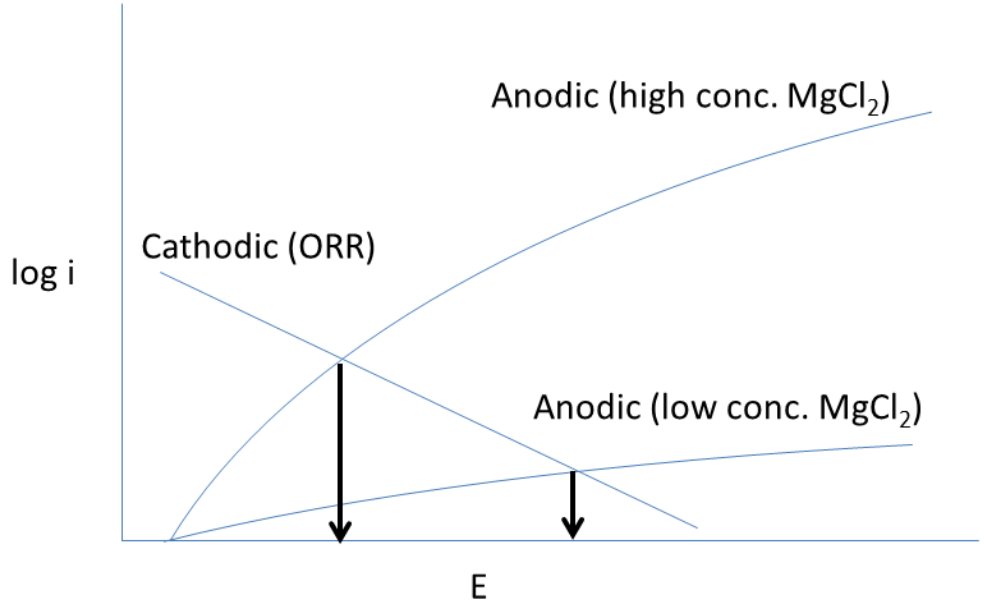

Figure 6-17 Evans' Diagram explaining the effect of increased $MgCl_2$ on the passive current density of austenitic stainless steels. Increasing solution concentrations drive potential lower and current higher, increasing dissolution when at low RH. This mechanism may cause the formation of shallow dish regions

The effect of Mo on the corrosion of austenitic stainless steels has been explored by a variety of techniques. EIS has been used to show that Mo influences nearly all of the principal reactions involved in dissolution, intermediate formation and repassivation of stainless steels [203].

The pitting and repassivation behaviour of 304L and 316L goes through a transition at 3 M $MgCl_2$ (Figure 6-15b), which is equivalent to an atmospheric humidity of 58% RH. In 316L, both pitting and repassivation show well defined potential values rather than the gradual curves observed in 304L. Metastability is also prominent in 316L during pitting initiation in this concentration. These observations are related to the well-established effect of molybdenum on localised corrosion, both during initiation and repassivation. Mo is considered to enrich the corroding interface [109,

110] which not only affects dissolution but also the initiation phase. Mo-enrichment in passive films is only found in the passive film after extended polarisation at active potentials and would not normally be found in a passive film that has been held at negative potentials before use [204-206].

The E_{pit} value of 316L was observed to be higher than that of 304L in the same solution in all wire electrochemistry in this work. This is consistent with previous pitting behaviour experienced in austenitic stainless steel alloys in chloride solutions [207] which is largely agreed to be due to a combination of enrichment of the passive oxide layer by Mo [26, 77, 107, 192, 207, 208] and the reduction of current density during active dissolution [109, 110]. These combine to allow pit initiation to fail, resulting in metastable pitting. During repassivation, the reduced active dissolution is a key influence of Mo. The mechanism is considered to be an enrichment of Mo in the sublayer of the corroding surface [209], increasing the *IR*-drop of the system by raising the exchange current density of the alloy and thus increasing the interfacial potential required for metal ions to be liberated from the corrosion front. The Mo-distribution in the passive layer is not relevant during this repassivation as the mechanism requires a 3D oxide.

6.3.4. Application of EIS to one-dimensional pitting

Figure 6-9 shows an attempt to discern the interfacial potential in 1D pits. There are significant differences in response to electrochemical perturbations between salt-covered surfaces and during active dissolution. It is clear that the same equivalent circuit model is not suitable for all surfaces during pitting, as was alluded to in Figure 6-7. However, clear differences between 304L and 316L were able to be shown. 316L has a significantly high IR-corrected potential than 304L at the same current density, which is in agreement with experimental observations [110].

Attempts to extract Tafel slopes from the activation region of these pits have given values that are significantly higher that in the literature. Mi [12] showed that for 304L, 3 M $MgCl_2$ has a Tafel slope between 48-57 mV/decade and in 4 M $MgCl_2$ a Tafel slope between 50-66 mV/decade. The values found in these data show 77 mV/decade in 3 M $MgCl_2$ and 107 mV/decade in 4 M $MgCl_2$. This indicated a weakness in the modelling used in this work that needs further development.

6.3.5. Application to atmospheric corrosion

One of the key factors that defines atmospheric corrosion is the presence of highly concentrated chloride solutions. Prosek *et al*.[210] observed a difference in pitting between 304L and 316L: 304L suffered attack at 50% RH in 304L and etching seen at up to 70% RH at 30 °C, while 316L saw attack only at 30% RH at 30 °C. Nam *et al.*[125] used silver-wire electrodes to isolate pitting initiation under droplets of $MgCl_2$ in 304L to isolate a range of humidities for pit initiation of between 48-58 %RH, which equates to solution concentrations of between 3.5-4.1 M $MgCl_2$ at initiation. Nam *et al.* also showed for the same droplets repassivation occurs between 56%-70% RH, or between 2.9-3.7 M $MgCl_2$. In these results, pitting and repassivation behaviour in solutions with concentrations of 3.5 M $MgCl_2$ and greater showed a different nature than those at more dilute concentrations.

At high concentrations, between 3.5 M and 5 M $MgCl_2$, there is a virtual absence of metastable pitting during initiation which shows a dramatic increase in pitting stability in early stages, possibly caused by reduction in the $D\Delta C$ term. This is also supported by the plate results in 4 M $MgCl_2$ showing multiple sites of initial attack. This means that the initiation site that succeeds when atmospheric corrosion occurs under a droplet may not be primarily determined by the most active initiation site but by other environmental factors. This observation is supported by results in chapter 5

regarding corrosion under droplets of different deposition concentration. When saturated $MgCl_2$ droplets are deposited on 304L there is a strong trend towards pitting at the centre of the droplet. This implies a rapid deoxygenation of the droplet shortly after deposition that allows cathodic regions to develop at the droplet edges. The evidence of multiple attack sites in plates submerged in 4 M $MgCl_2$ provides a mechanism to explain how the solution at the plate interface would deoxygenate so quickly, as so many sites are active at the same time. The reduced $D\Delta C$ values at such high concentrations also limit the resupply of oxygen to these regions.

Repassivation is also hindered at concentrations similar to those that show atmospheric corrosion. The sharp drops in current seen in both wire loops and one-dimensional pitting experiments in 1 M and 2 M $MgCl_2$ solutions indicate repassivation, but these correspond to humidities above 83% RH which is significantly above the repassivation threshold of atmospheric corrosion observed in both alloys. The lack of repassivation behaviour in solutions with concentrations above 3.5 M $MgCl_2$ shows that repassivation does not readily occur in atmospheric corrosion if humidity is kept in an aggressive range. This has consequences for the interpretation of the role of Mo in 316L. Reduction in active dissolution rates after alloying with Mo, as proposed by Newman *et al*. [13, 109, 110, 180, 211-213], is probably a much more significant factor the passivation and repassivation behaviour in these conditions, than suggested by Marcus *et al* [26, 77, 107, 180, 214].

Atmospheric corrosion under droplets of $MgCl_2$ is observed to have a shallow dish region that appears early in the corrosion process [126, 136]. The appearance of this shallow dish region, which has significant etching in the region surrounding the attacked sulphide inclusions, is very similar to the superficial etching attack observed in fully-immersed plate in 4 M $MgCl_2$ (Figure 6-16e).

6.4. Conclusions

- Potentiodynamic sweeps were conducted using three types of electrochemical samples: wires, one-dimensional artificial pits, and flat plates of stainless steel. Sweeps were conducted in solutions of between 1 – 5 M $MgCl_2$. Experiments used both 304L and 316L austenitic stainless steels.
- It was found that increasing solution concentration reduces E_{pit} and E_{rp} in wire and plate experiments, and E_{rp} in one-dimensional experiments. At concentrations of 3 M $MgCl_2$ and above, i.e. concentrations where attack is normally observed in atmospheric corrosion, pitting and repassivation behaviour was changed as compared to lower concentrations. Metastable pitting was rarely observed at higher concentrations and pitting potential was not a single point but a gradual increase in current density over a period of tens of seconds. Repassivation behaviour at high $MgCl_2$ concentrations was not a sharp reduction of current density but a gradual reduction that showed no sign of repassivation but instead a mere cessation of current. There did not appear to be a competition between repassivation and active dissolution at high concentrations of $MgCl_2$.
- Where a repassivation did exist, at lower $MgCl_2$ concentrations, this did not appear at a sharp potential but over a range of potentials as shown by the zig-zag data. This indicated that partial passivation occurs on the surface of the pit that then propagates over the active surface.
- The addition of Mo to austenitic stainless steel is observed to affect both the active dissolution rate and repassivation potential. However, in conditions similar to those that induce atmospheric corrosion on stainless steels, repassivation behaviour is less significant due to the general resistance to

repassivation in these highly concentrated solutions. Mo is seen to cause passivation in more aggressive solution.

- EIS has potential to be useful in helping to calculate interfacial potentials, and clear differences have been observed between 304L and 316L under salt layer dissolution and active dissolution. There is still scope for improvement in this approach as the suggested model did not generate data that is consistent with current knowledge about the physical system of one-dimensional pitting.

7. General Discussions and Future Work

7.1. Synchrotron studies

7.1.1. Identification of nitrate-rich salt with XRD

Synchrotron-based XRD was used to identify the species of salt at the bottom of pits in 304L stainless steel pits grown in 1 M NaCl and with trace amounts of nitrate. This study solves a long-standing question about the nature of the salt layer in these pits [14]. There had been a suggestion that this presence of nitrate causes between nitrate-rich and chloride-rich salt species, generating current oscillations [215]. There was also the possibility that a molten salt may be present, as observed in high voltage electrochemical machining of Fe in $NaNO_3$ solutions [98, 216]. We have shown **(4.2.3)** that this is not the case and that competitive salt species are not the likely cause of the oscillatory behaviour seen in electrochemical scans.

7.1.2. Use of radiography to isolate partial passivation mechanism

By using radiography on 1D pits, we were able to isolate subtle variations in pit surface roughness, that led to the observation of a partial passivation mechanism where the surface showed islands of passive regions that propagated out **(4.2.5).** This was not a uniform transition between two competing processes, as had been previously argued by Uhlig and Leckie [88], who proposed a uniform transition occurred at certain potentials where Cl ions would be displaced at the corrosion surface by adsorbed NO_3^- ions. A mechanism has been proposed that explains the partial passivation behaviour and how it could generate current oscillation by the advancing corrosion front undercutting localised passive regions

7.2. Electrochemistry of Atmospheric Corrosion

$MgCl_2$ is a significant salt in atmospheric corrosion as it has low deliquescence humidity (33% RH) and is abundant in sea water. By using highly concentrated

$MgCl_2$ we are able to closely link this electrochemistry with atmospheric corrosion. Both the pitting and repassivation behaviour of 304L and 316L are affected by changes in concentration.

7.2.1. Pitting Behaviour in 'atmospheric' conditions

In wire samples, forward sweeps of 304L in highly concentrated solutions of $MgCl_2$ were conducted by Mi [12, 126]. Mi found that E_{pit} reduced with increasing solution concentration and that metastable pitting ceased at concentrations of 4 M $MgCl_2$ or greater. The pitting potential at these higher concentrations was between -200 and -350 mV, which is close to OCP values. In the current work with polarisation curves on wires on 304L and 316L **(6.2.5)**, pitting was preceded by metastable pitting in solutions with concentrations of 1-3.5 M for both alloys with sharp pitting potentials between 1-2 M $MgCl_2$ in 304L and 1-3 M $MgCl_2$ in 316L. The extended pitting resistance of 316L is significant as this is the concentration that pitting is generally considered to start in atmospheric conditions [114]. Traces of metastability appear at concentrations of 3.5 M in both alloys, but the pitting behaviour at higher concentrations is not a sudden increase but a curve upwards. This behaviour agrees with the results from the plate sample **(3.7)** which shows extensive attack around dozens of sites, indicating the gradual increase in current may well be a summation of several sites of attack. In practice, very few instances of atmospheric corrosion show multiple sites [126, 190] of attack, due to cathodic protection across the droplets surface.

7.2.2. Repassivation behaviour in 'atmospheric' conditions

Understanding of E_{rp} is not particularly consistent in the literature. Analysis is usually done under bulk conditions, and does not consider local effects. Solution concentration has shown to generally lower E_{rp} linearly with logarithmic increase in chloride concentration [81, 85]. However, this work shows that the various

definitions of repassivation may not inform us of the physical processes occurring at low potentials. Ernst and Newman [55] suggested repassivation occurs when the current density cannot be recovered with a rapid increase in potential. Mi [12] also used this definition. Repassivation was said to be detectable by a pronounced curvature in the plot of current against potential during slow reverse sweeps. Woldemedhin *et al.* [11, 217] looked at one-dimensional pitting that has been conducted in different chloride solutions to look at repassivation behaviour, but the concentration tested never goes above 3 M [Cl-] and once E_{rp} is reached there is no reverse sweep to ensure that the surface has fully passivated. Guo [57] developed this technique by implementing zig-zag potential program on one dimensional pits of 304L. This technique gives "passivation loops" **(6.2.2),** as once repassivation begins and potential is increased current cannot be contributed by the passivated region. This allows easier isolation of the E_{rp} value.

In the current study, this zig-zag technique was extended to include both 304L and 316L to investigate the role of Mo on repassivation behaviour on localised corrosion. Passivation loops were observed in 1 M and 2 M $MgCl_2$ on 304L, and 2 M and 3 M $MgCl_2$ on 316L (1 M on 316L passivated readily). Each of these also showed pronounced curvature **(6.2.3),** agreeing with Ernst and Newman's observation. At 3 and 4 M $MgCl_2$ for 304L and 4 M $MgCl_2$ for 316L, passivation loops were not observed and current showed ohmic response to until very low potentials. In these pits, there does not appear to be the partial passivation observed in more dilute solutions, or in the nitrate-rich solutions examined using synchrotron techniques **(4.2.5).** This is also seen in the reverse sweep for the wire experiments **(6.2.5).** In 304L, E_{rp} becomes less of a sharp transition in concentrations of 3 M $MgCl_2$ and above, and in concentrations of 4 M $MgCl_2$ and above in 316L. This sharp transition

can be seen as the propagation of passivity inside the pit, as witnessed with radiography in **(6.3.2)**.As E_{rp} has been found to be independent of pit depth[11], it can be suggested that under atmospheric conditions pits will not repassivate by the formation of a passive oxide layer unless diluted. This ties in well with the wet-dry cycling results in atmospheric corrosion [57, 125, 150], where pits are observed to passivate at high humidities that correspond to solution concentrations of less than 3 M $MgCl_2$. Fluctuations in RH to higher percentages may limit corrosion damage.

7.3. Role of Molybdenum in atmospheric corrosion

316L is known to have higher corrosion resistance than 304L. Prosek [210] observed that this improved resistance is also observed in atmospheric corrosion of Mo-rich stainless steels. Mohammed-Ali [131] observed a pitting threshold where attack on 316L plate occurred much less often than on 304L at 56% RH when using droplets of 1000 μg/cm^2. Above 65% RH, 304L still occasionally pitted but 316L did not. Albores-Silva *et al*. [218] showed that in stress corrosion cracking tests that at elevated temperatures of 50 °C, the pitting that did occur at 60% RH resulted in large crack formation.

Three main theories have been used to explain the effect of Mo on localised corrosion:

1. Interruption of mass transport through the formation of polymeric molybdate species
2. Reduction of active dissolution due to subsurface enrichment of Mo
3. Increased stability of passive layer due to enrichment of Mo in oxide layer

Interruption of mass transport by polymeric molybdates has largely been disproved by XANES analysis [112]. This is further supported by the similarity in dissolution rates of 304L and 316L when a salt layer is present.

Although this diffusion-limited current density is the same, the E_T for both alloys are different and the anodic dissolution kinetics of the bare (film-free) actively dissolving surface are different (6.2.1), as previously discussed by Newman [110, 219]. This demonstrates that passive film formation is not the dominant factor for repassivation in the pit. Repassivation of 316L appears to occur at higher current densities than 304L. This implies that 316L passivates in more concentrated solutions, since:

$$\frac{i}{i_{sat}} = \frac{C}{C_{sat}} \qquad \textbf{Equation 7-1}$$

Where i is current density, i_{sat} is saturated current density, c is solution concentration and c_{sat} is saturated concentration. As such, the solution when 316L passivates is more aggressive than when 304L passivates. There may be some effect of Mo on the passive film growth, but this is at very early stages of film growth and not at steady state. There is strong evidence of the absence of passivation in high concentrations of $MgCl_2$, so this difference in passive layer stability is only relevant in non-atmospheric conditions where solutions are dilute enough for passivation to occur. The increase in E_T and reduction in active dissolution reduce pit stability significantly.

7.4. Analysis of corrosion under droplets

Maier and Frankel [136] and Hastuty *et al*. [162] both observed shallow dish formation of pits under droplets of $MgCl_2$ on stainless steels. Maier observed pit

formation on 304L in the first 100s of seconds to appear to grow as “earring” or in an ear-shaped morphology as it. Hastuty observed on 430L after 6 hours of growth large, shallow attack. Mohammed-Ali [131] showed the development of these shallow dish regions in relationship to 304L and 316L plate samples, showing that their diameter was broadly similar between alloys but was influenced by the size of the droplet. Mohammed-Ali also noted the development of satellite pits, that occur in the region near the shallow dish, and spiral morphologies that, developed from the earring attack, occur within the shallow dish region.

In this work, the dependence on droplet thickness and concentration was linked to the formation of specific morphologies of pits (5.2.2). “Spiral” shaped pitting always occurred when a shallow dish region was present. Satellite pits only occurred in some conditions, when in concentrated solutions and under thin solution thicknesses. Where satellite pits did occur, time-lapse imaging showed that spiral pitting stopped growing after a few hours while satellite pitting continued. This is attributed to the cathodic limited nature of atmospheric corrosion under droplets [163, 186], with the satellite pits starving the spiral regions of current by nature of being more stable due to increased occlusion. Satellite pits never occurred in the shallow dish region, though Mohammed-Ali did see instances where this did occur [131]. Satellite pit caps are known to have elevated S content [126] so it is reasonable to assume that they occur at sulphur inclusions and need sufficient occlusion to propagate. In highly concentrated solutions, diffusivity is lower so satellite pits would be more likely to stabilise and propagate.

The facetted nature of the shallow dish regions implies either active dissolution from a bare surface or dissolution of the passive surface, as dissolution under a salt

layer would lead to roughened surfaces, as seen in the spiral pits adjacent to the shallow dish regions and artificial pitting morphologies [6].

This work also addresses a common misconception about the relevance of Evans droplet model to metals that are highly passive (5.3.2.4). In Evans' seminal work on droplets on freshly abraded Fe, he found that dissolution tended to be in the centre of the droplet, due to differential aeration. As iron can easily undergo reductive dissolution on the passive film dissolution can migrate across the metal-solution interface. However this approach is not appropriate for pitting of stainless steel, as pits initiate at inclusions.

Recent work by Schindelhoz *et al*. has tried to compare salt crystal deposition to droplet work over long periods and has found that corrosion can occur under salt crystals by adsorbed water. This work also clarified the difference between atmospheric corrosion by aerosol deposition (where with first liquid phase is saturated) and by splash zone deposition (where the first liquid phase is dilute) which is not always appreciated in the literature [126, 190, 191].

7.5. Future Work

7.5.1. More accurate EIS data to isolate critical values using TRFT-EIS

There is great scope to continue in trying to isolate electrochemical values for modelling. The electrochemical impedance spectroscopy (EIS) that was used in 6.2.3 was a useful preliminary approach with some limitations on providing accurate interfacial potential in one-dimensional pits of 304L and 316L. The time taken to conduct frequency sweeps during corrosion meant that the surface was changing appreciably during the course of the scan, and there was limitation in the range of

frequencies that could be used. It is possible to use more advanced EIS techniques, such as Time Resolved Fourier Transform EIS [220]. This technique is able to do full frequency sweeps between 1 M Hz to 10 mHz in under a second instead of several hours.

7.5.2.*In Situ* investigation of partial passivation and repassivation

While the foil results from radiography have provided useful data, the majority of the sample surface is in close proximity with the pit edge. By using a fast tomography set up at a synchrotron, it may be possible to observe local changes in morphology and any partial passivation when the sample is less influenced by restrictions in mass transfer near a pit edge. Radiography of nitrate to see oscillatory behaviour would also further inform localised corrosion studies

High speed atomic force microscopy (HS-AFM) has recently been used to investigate the early stages of corrosion [221]. This technique can achieve sub-angstrom height resolution coupled with millisecond temporal resolution and has been used to investigate initiation stages of localised corrosion. It is feasible that this technique could be used to investigate the repassivation of localised corrosion, particularly using scratch-type experiments where the corroding interface is largely unoccluded.

7.5.3.Nitrate Reduction Mechanisms

The exact mechanism of nitrate reduction that caused passivation on 304L stainless steel in 1M NaCl, is still unknown. Use of synchrotron based spectroscopy, such as XANES or XAFS, could give evidence of reduction states of ions in the solution adjacent to the pit, allowing nitrate reduction pathways to be established.

7.5.4. Role of Molybdenum in concentrated solutions.

Scratch tests have been used on passive alloys to measure the charge needed for oxides to regrow, and there has already been work comparing 304/316. However, this has never been done in concentrated solutions and could further inform the influence of repassivation and the role Mo plays in the additional corrosion resistance that Mo gives to stainless steels.

.

8. Conclusions

1. Work in this thesis has developed ideas about the competition between active dissolution and repassivation inside austenitic stainless steel pits. The development of passivation has been observed using both radiography and electrochemistry. In the case of stainless steel 304L dissolving under a salt layer in a mixed chloride:nitrate solution, repassivation develops first in a finite region on the pit surface and propagates across the metal surface.
2. The salt layer that occurs during current oscillations of pitting of 304L in mixed chloride:nitrate solutions is not a nitrate salt but has been identified as being similar to $FeCl_2.4H_2O$. A mechanism has been proposed to explain the oscillatory behaviour in current as a consequence of partial passivation leading to accelerated dissolution adjacent to passive areas and undercutting them.
3. Pitting and repassivation behaviour of 304L and 316L stainless steels in chloride solutions is affected by solution concentration. In more dilute solutions, polarisation curves show metastable pitting in the passive regions followed by a sharp breakdown (pitting) potential However, in highly concentrated solutions, similar to those found during atmospheric corrosion, pitting was found to give a gradual increase in current with no obvious sign of metastable pitting. Where repassivation of stainless steels in dilute solutions shows a sharp drop in current as the passivation spreads rapidly throughout the pit, this was not observed in highly concentrated solutions in which the current reduced gradually.
4. A comparison was made between the electrochemical behaviour of 304L and 316L artificial pits in concentrated solutions to establish the significance of Mo in atmospheric corrosion of stainless steels. When the potential was swept down from conditions where the current was under diffusion control and the pit surface was initially covered with a salt layer, 316L was observed to lose its salt layer at

higher potentials than 304L, and have a lower active dissolution rate. When passivation of the pit took place, it was observed to occur at higher current densities in 316L than in 304L, indicating that the passive film is stable in more concentrated and aggressive solutions.

5. Electrochemical impedance spectroscopy (EIS) was used to calculate *IR*-corrected current voltage characteristic diagrams. Evidence was shown of an increased interfacial potential in 316L as compared to 304L, supporting the hypothesis of Mo enrichment at the corrosion interface.
6. The morphology of atmospheric corrosion under droplets of $MgCl_2$ on 304L stainless steels has been shown to be strongly influenced by RH and solution thickness during the propagation phase. The initial stage of pit growth when RH $\leq$ 52%. involves development of a shallow "dish" that has crystallographic attack, and is likely to be covered with a rapidly dissolving passive film. Following this, the dish may develop spiral pits (sometimes referred to as "ears") under conditions where there are higher and more dilute droplets (higher chloride deposition density and higher RH). However, under conditions of lower chloride deposition density and lower RH, "satellite" pits with dense covers may be observed outside the shallow dish region. This sensitivity to RH, hence solution concentration, has been attributed to a combination of diffusivity and conductance in the solution. The formation of "satellite" pits at low RH in thin solutions has been attributed to the increase of stability of pitting sites adjacent to the shallow dish region.
7. Pitting position under droplets of $MgCl_2$ on 304L stainless steel is affected by the initial solution concentration and the thickness of the solution droplet as at the moment initiation occurs. Under dilute solutions, there is no trend in pitting

position regardless of environmental RH. A trend towards pitting towards the edge of the droplet occurs in more concentrated solutions, and in highly concentrated solutions, i.e. concentrations that promote immediate pitting, there is a trend for pitting at the centre of the droplet. This has been explained by the generation of different aeration in the droplet and changes in IR drop between anodic and cathodic regions with droplet thickness.

8. The variation in pitting behaviour between deposition of dilute and concentrated droplets highlighted differences in atmospheric corrosion application. Corrosion caused by the aerosol deposition of salts experience saturated solutions as their first liquid phase. Corrosion caused by splash zone deposition experience dilute concentrations initially. These two regimes behave differently in application, though this difference is rarely acknowledged in the literature.

9. References

1. Smart, N., A. Pritchard, and A. Turnbull. *Review of Environmental Conditions for Storage of ILW Radioactive Waste Containers*. 2010; Available from: http://www.nda.gov.uk.
2. Padovani, C., R.J. Winsley, N.R. Smart, P.A.H. Fennell, C. Harris, and K. Christie, *Corrosion Control of Stainless Steels in Indoor Atmospheres-Practical Experience (Part 2).* Corrosion, 2015. **71**(5): p. 646-666.
3. Cole, I.S., D.A. Paterson, W.D. Ganther, A. Neufeld, B. Hinton, G. McAdam, M. McGeachie, R. Jeffery, L. Chotimongkol, C. Bhamornsut, N.V. Hue, and S. Purwadaria, *Holistic Model for Atmospheric Corrosion - Part 3 - Effect of Natural and Man Made Landforms on Deposition of Marine Salts in Australia and South-East Asia.* Corrosion Engineering Science and Technology, 2003. **38**(4): p. 267-274.
4. Cole, I.S., T.H. Muster, N.S. Azmat, M.S. Venkatraman, and A. Cook, *Multiscale Modelling of the Corrosion of Metals under Atmospheric Corrosion.* Electrochimica Acta, 2011. **56**(4): p. 1856-1865.
5. Wexler, A., W.M. Haynes, and L.D. R., *CRC Handbook of Chemistry and Physics : A Ready-Reference Book of Chemical and Physical Data*2011, Boca Raton, Fla.: CRC Press.
6. Xu, W., S.R. Street, M. Amri, J.F.W. Mosselmans, P.D. Quinn, T. Rayment, and A.J. Davenport, *In-Situ Synchrotron Studies of the Effect of Nitrate on Iron Artificial Pits in Chloride Solutions (I). On the Structures of Salt Layers.* Journal of the Electrochemical Society, 2015. **162**(6): p. C238-C242.
7. Rayment, T., A.J. Davenport, A.J. Dent, J.P. Tinnes, R.J.K. Wiltshire, C. Martin, G. Clark, P. Quinn, and J.F.W. Mosselmans, *Characterisation of Salt Films on Dissolving Metal Surfaces in Artificial Corrosion Pits Via in Situ Synchrotron X-Ray Diffraction.* Electrochemistry Communications, 2008. **10**(6): p. 855-858.
8. Ghahari, M., D. Krouse, N. Laycock, T. Rayment, C. Padovani, M. Stampanoni, F. Marone, R. Mokso, and A.J. Davenport, *Synchrotron X-Ray Radiography Studies of Pitting Corrosion of Stainless Steel: Extraction of Pit Propagation Parameters.* Corrosion Science, 2015. **100**: p. 23-35.
9. Laycock, N.J., D.P. Krouse, S.M. Ghahari, A.J. Davenport, T. Rayment, and C. Padovani, *Localised Dissolution Kinetics from Fast in-Situ Radiography of Propagating Pits in Stainless Steel and Implications for Modeling Pitting Corrosion over Long Time-Scales*, in *Critical Factors in Localized Corrosion 7*, J.R. Kish, et al., Editors. 2012. p. 3-16.
10. Ghahari, S.M., D.P. Krouse, N.J. Laycock, T. Rayment, C. Padovani, T. Suter, R. Mokso, F. Marone, M. Stampanoni, M. Monir, and A.J. Davenport, *Pitting Corrosion of Stainless Steel: Measuring and Modelling Pit Propagation in Support of Damage Prediction for Radioactive Waste Containers.* Corrosion Engineering Science and Technology, 2011. **46**(2): p. 205-211.
11. Woldemedhin, M.T., J. Srinivasan, and R.G. Kelly, *Effects of Environmental Factors on Key Kinetic Parameters Relevant to Pitting Corrosion.* Journal of Solid State Electrochemistry, 2015: p. 1-13.
12. Mi, N., *Synchrotron X-Ray Studies of Atmospheric Pitting Corrosion of Stainless Steel*, in *Metallurgy and Materials*2013, University of Birmingham: Birmingham.
13. Laycock, N.J. and R.C. Newman, *Localised Dissolution Kinetics, Salt Films and Pitting Potentials.* Corrosion Science, 1997. **39**(10-11): p. 1771-1790.
14. Newman, R.C. and M.A.A. Ajjawi, *A Microelectrode Study of the Nitrate Effect on Pitting of Stainless-Steels.* Corrosion Science, 1986. **26**(12): p. 1057-1063.

15. Alkire, R., D. Ernsberger, and T.R. Beck, *Occurrence of Salt Films During Repassivation of Newly Generates Metal-Surfaces.* Journal of the Electrochemical Society, 1978. **125**(9): p. 1382-1388.
16. Aouina, N., F. Balbaud-Celerier, F. Huet, S. Joiret, H. Perrot, F. Rouillard, and V. Vivier, *Initiation and Growth of a Single Pit on 316l Stainless Steel: Influence of So42- and Clo4- Anions.* Electrochimica Acta, 2013. **104**: p. 274-281.
17. Heurtault, S., R. Robin, F. Rouillard, and V. Vivier, *Initiation and Propagation of a Single Pit on Stainless Steel Using a Local Probe Technique.* Faraday Discussions, 2015. **180**(0): p. 267-282.
18. Trethewey, K.R. and J. Chamberlain, *Corrosion for Science and Engineering*. 2nd ed1995 Harlow: Addison Wesley Longman Ltd.
19. Llewellyn, D.T. and R.C. Hudd, *Steels - Metallurgy and Applications (3rd Edition)*, Elsevier.
20. ASM International. Handbook Committee., *ASM Handbook*. 10th editon. ed. volumes.
21. Fontana, M., *Corrosion Engineering* 1986, New York: McGraw-Hill Book Company.
22. Frankel, G.S., *Pitting Corrosion of Metals - a Review of the Critical Factors.* Journal of the Electrochemical Society, 1998. **145**(6): p. 2186-2198.
23. Sato, N., *Theory for Breakdown of Anodic Oxide Films on Metals.* Electrochimica Acta, 1971. **16**(10): p. 1683-&.
24. Burstein, G.T. and S.P. Mattin, *Nucleation of Corrosion Pits on Stainless-Steel.* Philosophical Magazine Letters, 1992. **66**(3): p. 127-131.
25. Okada, T., *A Theory of Perturbation-Initiated Pitting.* Journal of the Electrochemical Society, 1985. **132**(3): p. 537-544.
26. Marcus, P., V. Maurice, and H.H. Strehblow, *Localized Corrosion (Pitting): A Model of Passivity Breakdown Including the Role of the Oxide Layer Nanostructure.* Corrosion Science, 2008. **50**(9): p. 2698-2704.
27. Galvele, J.R., *Transport Processes and Mechanism of Pitting of Metals.* Journal of the Electrochemical Society, 1976. **123**(4): p. 464-474.
28. Stewart, J. and D.E. Williams, *The Initiation of Pitting Corrosion on Austenitic Stainless-Steel - on the Role and Importance of Sulfide Inclusions.* Corrosion Science, 1992. **33**(3): p. 457-474.
29. ASM International., *Casting Design and Performance,* 2009, Materials Park , Ohio: ASM International.
30. Hoar, T.P. and U.R. Evans, *Some Factors in Anodic Processes on Corroding Metals.* Journal of the Electrochemical Society, 1952. **99**(5): p. 212-218.
31. Streicher, M.A., *Pitting Corrosion of 18cr-8ni Stainless Steel.* Journal of the Electrochemical Society, 1956. **103**(7): p. 375-390.
32. Eklund, G.S., *Initiation of Pitting at Sulfide Inclusions in Stainless-Steel.* Journal of the Electrochemical Society, 1974. **121**(4): p. 467-473.
33. Wranglen, G., *Pitting and Sulfide Inclusions in Steel.* Corrosion Science, 1974. **14**(5): p. 331-349.
34. Castle, J.E. and R. Ke, *Studies by Auger-Spectroscopy of Pit Initiation at the Site of Inclusions in Stainless-Steel.* Corrosion Science, 1990. **30**(4-5): p. 409-428.
35. Lott, S.E. and R.C. Alkire, *The Role of Inclusions on Initiation of Crevice Corrosion of Stainless-Steel .1. Experimental Studies.* Journal of the Electrochemical Society, 1989. **136**(4): p. 973-979.
36. Ryan, M.P., D.E. Williams, R.J. Chater, B.M. Hutton, and D.S. McPhail, *Why Stainless Steel Corrodes.* Nature, 2002. **415**(6873): p. 770-774.
37. Meng, Q., G.S. Frankel, H.O. Colijn, and S.H. Goss, *Metallurgy - Stainless-Steel Corrosion and Mns Inclusions.* Nature, 2003. **424**(6947): p. 389-390.

38. Ryan, M.P., D.E. Williams, R.J. Chater, B.M. Hutton, and D.S. McPhail, *Metallurgy - Stainless-Steel Corrosion and Mns Inclusions - Reply.* Nature, 2003. **424**(6947): p. 390-390.
39. Schmuki, P., H. Hildebrand, A. Friedrich, and S. Virtanen, *The Composition of the Boundary Region of Mns Inclusions in Stainless Steel and Its Relevance in Triggering Pitting Corrosion.* Corrosion Science, 2005. **47**(5): p. 1239-1250.
40. Chiba, A., I. Muto, Y. Sugawara, and N. Hara, *Direct Observation of Pit Initiation Process on Type 304 Stainless Steel.* Materials Transactions, 2014. **55**(5): p. 857-860.
41. Chiba, A., I. Muto, Y. Sugawara, and N. Hara, *Pit Initiation Mechanism at Mns Inclusions in Stainless Steel: Synergistic Effect of Elemental Sulfur and Chloride Ions.* Journal of the Electrochemical Society, 2013. **160**(10): p. C511-C520.
42. Williams, D.E., M.R. Kilburn, J. Cliff, and G.I.N. Waterhouse, *Composition Changes around Sulphide Inclusions in Stainless Steels, and Implications for the Initiation of Pitting Corrosion.* Corrosion Science, 2010. **52**(11): p. 3702-3716.
43. Hakkarainen, T., *Anodic Behaviour of Stainless Steels in Simulated Pit Solutions*, in *Corrosion Chemistry within Pits, Crevices and Cracks*, A. Turnbull, Editor 1987, HMSO Books: London. p. 17-26.
44. Hoar, T.P., *The Corrosion of Tin in Nearly Neutral Solutions.* Transactions of the Faraday Society, 1937. **33**(2): p. 1152-1166.
45. Wilde, B.E. and E. Williams, *Use of Current/Voltage Curves for Study of Localized Corrosion and Passivity Breakdown on Stainless Steels in Chloride Media.* Electrochimica Acta, 1971. **16**(11): p. 1971-1985.
46. Wilde, B.E. and E. Williams, *Relevance of Accelerated Electrochemical Pitting Tests to Long-Term Pitting and Crevice Corrosion Behavior of Stainless Steels in Marine Environments.* Journal of the Electrochemical Society, 1971. **118**(7): p. 1057-1062.
47. Beck, T.R. and R.C. Alkire, *Occurrence of Salt Films During Initiation and Growth of Corrosion Pits.* Journal of the Electrochemical Society, 1979. **126**(10): p. 1662-1666.
48. Isaacs, H.S., *The Localized Breakdown and Repair of Passive Surfaces During Pitting.* Corrosion Science, 1989. **29**(2-3): p. 313-323.
49. Pistorius, P.C. and G.T. Burstein, *Metastable Pitting Corrosion of Stainless-Steel and the Transition to Stability.* Philosophical Transactions of the Royal Society of London Series a-Mathematical Physical and Engineering Sciences, 1992. **341**(1662): p. 531-559.
50. Pickering, H.W. and R.P. Frankenthal, *Mechanism of Localized Corrosion of Iron and Stainless-Steel .1. Electrochemical Studies.* Journal of the Electrochemical Society, 1972. **119**(10): p. 1297-1304.
51. Frankenthal, R.P. and H.W. Pickering, *Mechanism of Localized Corrosion of Iron and Stainless-Steel .2. Morphological Studies.* Journal of the Electrochemical Society, 1972. **119**(10): p. 1304-1310.
52. Isaacs, H.S., *Behavior of Resistive Layers in Localized Corrosion of Stainless-Steel.* Journal of the Electrochemical Society, 1973. **120**(11): p. 1456-1462.
53. Beck, T.R., *Pitting of Titanium .2. One-Dimensional Pit Experiments.* Journal of the Electrochemical Society, 1973. **120**(10): p. 1317-1324.
54. Tester, J.W. and H.S. Isaacs, *Diffusional Effects in Simulated Localized Corrosion.* Journal of the Electrochemical Society, 1975. **122**(11): p. 1438-1445.
55. Ernst, P. and R.C. Newman, *Pit Growth Studies in Stainless Steel Foils. I. Introduction and Pit Growth Kinetics.* Corrosion Science, 2002. **44**(5): p. 927-941.
56. Street, S.R., W. Xu, M. Amri, L. Guo, S.J.M. Glanvill, P.D. Quinn, J.F.W. Mosselmans, J. Vila-Comamala, C. Rau, T. Rayment, and A.J. Davenport, *The Effect of Nitrate on Salt Layers in Pitting Corrosion of 304l Stainless Steel.* Journal of the Electrochemical Society, 2015. **162**(9): p. C457-C464.

57. Guo, L., *Atmospheric Localised Corrosion of Type 304 Austenitic Stainless Steels*, in *Metallurgy and Materials*2016, University of Birmingham: Birmingham.
58. Xu, W., *Synchrotron X-Ray and Electrochemical Studies of Pitting Corrosion of Iron*, in *School of Metallurgy and Materials,*2014, University of Birmingham: Birmingham, UK.
59. Novakovsi, V.M. and A.N. Sorokina, *Model Study of Chloride Pitting in 18-8 Stainless Steel.* Corrosion Science, 1966. **6**(5): p. 227-233.
60. Beck, T.R., *Formation of Salt Films During Passivation of Iron.* Journal of the Electrochemical Society, 1982. **129**(11): p. 2412-2418.
61. Russell, P. and J. Newman, *Current Oscillations Observed within the Limiting Current Plateau for Iron in Sulfuric-Acid.* Journal of the Electrochemical Society, 1986. **133**(10): p. 2093-2097.
62. Hoar, Mears, and Rothwell, *The Relationships between Anodic Passivity, Brightening and Pitting.* Corrosion Science, 1965. **5**: p. 279 - 289.
63. Danielson, M.J., *Transport-Properties of Salt Films on Nickel in 0.5n Hcl.* Journal of the Electrochemical Society, 1988. **135**(6): p. 1326-1332.
64. Clerc, C. and D. Landolt, *Ac Impedance Study of Anodic Films on Nickel in Licl.* Electrochimica Acta, 1988. **33**(7): p. 859-871.
65. Grimm, R.D., A.C. West, and D. Landolt, *Ac Impedance Study of Anodically Formed Salt Films on Iron in Chloride Solution.* Journal of the Electrochemical Society, 1992. **139**(6): p. 1622-1629.
66. Grimm, R.D. and D. Landolt, *Salt Films Formed During Mass-Transport Controlled Dissolution of Iron-Chromium Alloys in Concentrated Chloride Media.* Corrosion Science, 1994. **36**(11): p. 1847-1868.
67. West, A.C., R.D. Grimm, D. Landolt, C. Deslouis, and B. Tribollet, *Electrohydrodynamic Impedance Study of Anodically Formed Salt Films on Iron in Chloride Solutions.* Journal of Electroanalytical Chemistry, 1992. **330**(1-2): p. 693-706.
68. Sridhar, N. and D.S. Dunn, *In Situ Study of Salt Film Stability in Simulated Pits of Nickel by Raman and Electrochemical Impedance Spectroscopies.* Journal of the Electrochemical Society, 1997. **144**(12): p. 4243-4253.
69. Xu, W., S.R. Street, M. Amri, J.F.W. Mosselmans, P.D. Quinn, T. Rayment, and A.J. Davenport, *In-Situ Synchrotron Studies of the Effect of Nitrate on Iron Artificial Pits in Chloride Solutions (ii). On the Effect of Carbon.* Journal of the Electrochemical Society, 2015. **162**(6): p. C243-C250.
70. Tang, Y.C. and A.J. Davenport, *Magnetic Field Effects on the Corrosion of Artificial Pit Electrodes and Pits in Thin Films.* Journal of the Electrochemical Society, 2007. **154**(7): p. C362-C370.
71. Newman, R.C. and H.S. Isaacs, *Diffusion-Coupled Active Dissolution in the Localized Corrosion of Stainless-Steels.* Journal of the Electrochemical Society, 1983. **130**(7): p. 1621-1624.
72. Gaudet, G.T., W.T. Mo, T.A. Hatton, J.W. Tester, J. Tilly, H.S. Isaacs, and R.C. Newman, *Mass-Transfer and Electrochemical Kinetic Interactions in Localized Pitting Corrosion.* Aiche Journal, 1986. **32**(6): p. 949-958.
73. Enerhaug, J., U.M. Steinsmo, O. Grong, and L.R. Hellevik, *Dissolution and Repassivation Kinetics of a 12.3cr-2.6mo-6.5ni Super Martensitic Stainless Steel - a Comparative Study.* Journal of the Electrochemical Society, 2002. **149**(6): p. B256-B264.
74. Steinsmo, U. and H.S. Isaacs, *Dissolution and Repassivation Kinetics of Fe-Cr Alloys in Pit Solutions. 1. Effect of the Surface Salt Layer.* Journal of the Electrochemical Society, 1993. **140**(3): p. 643-653.

75. Macdonald, D.D., *Passivity - the Key to Our Metals-Based Civilization.* Pure and Applied Chemistry, 1999. **71**(6): p. 951-978.
76. Keir, J., *Phil. Trans., 80, 374; 1790.* Phil. Trans., 1790. **80**: p. 374.
77. Clayton, C.R. and I. Olefjord, *Passivity of Austenitic Stainless Steels*, in *Corrosion Mechanisms in Theory and Practice, Third Edition*, P. Marcus, Editor 2011, CRC Press: Hoboken.
78. Pourbaix, M., L. Klimzack-Mathieiu, C. Mertens, J. Meunier, C. Vanleugenhaghe, L. de Munck, J. Laureys, L. Neelemans, and M. Warzee, *Potentiokinetic and Corrosimetric Investigations of the Corrosion Behaviour of Alloy Steels.* Corrosion Science, 1963. **3**(4): p. 239-259.
79. Starr, K.K., E.D. Verink, and M. Pourbaix, *Significance of Protection Potential for Fe-Cr Alloys at Room-Temperature.* Corrosion, 1976. **32**(2): p. 47-51.
80. Ernst, P. and R.C. Newman, *Explanation of the Effect of High Chloride Concentration on the Critical Pitting Temperature of Stainless Steel.* Corrosion Science, 2007. **49**(9): p. 3705-3715.
81. Anderko, A., N. Sridhar, and D.S. Dunn, *A General Model for the Repassivation Potential as a Function of Multiple Aqueous Solution Species.* Corrosion Science, 2004. **46**(7): p. 1583-1612.
82. Dunn, D.S., G.A. Cragnolino, and N. Sridhar, *An Electrochemical Approach to Predicting Long-Term Localized Corrosion of Corrosion-Resistant High-Level Waste Container Materials.* Corrosion, 2000. **56**(1): p. 90-104.
83. Pourbaix, M., *Atlas of Electrochemical Equilibria in Aqueous Solutions*1974, Houston, Texas: National Association of Corrosion Engineers.
84. Hinds, G., L. Wickstrom, J. Abda, A. Turnbull, V. Smith, and R. Woollam, *Novel Method for Determination of Pitting Susceptibility in Aggressive Environments at Elevated Temperature and Pressure.* Corrosion Science, 2014. **85**: p. 33-41.
85. Yashiro, H. and K. Tanno, *The Effect of Electrolyte-Composition on the Pitting and Repassivation Behavior of Aisi 304 Stainless-Steel at High-Temperature.* Corrosion Science, 1990. **31**: p. 485-490.
86. Okada, T., *Considerations of the Stability of Pit Repassivation During Pitting Corrosion of Passive Metals.* Journal of the Electrochemical Society, 1984. **131**(5): p. 1026-1032.
87. Rodriguez, M.A., *Inhibition of Localized Corrosion in Chromium Containing Stainless Alloys.* Corrosion Reviews, 2012. **30**(1-2): p. 19-32.
88. Uhlig, H.H. and J.R. Gilman, *Pitting of 18-8 Stainless Steel in Ferric Chloride Inhibited by Nitrates.* Corrosion, 1964. **20**(9): p. T289-T292.
89. Kelly, R.G., Scully, Buchheit, and Shoesmith, *Electrochemical Methods*. Corrosion Technology, ed. P.E. Schweitzer2003, Boca Raton, Fl: CRC Press.
90. Lillard, R.S., G. Vasquez, and D.F. Bahr, *The Kinetics of Anodic Dissolution and Repassivation on Stainless Steel 304l in Solutions Containing Nitrate.* Journal of the Electrochemical Society, 2011. **158**(6): p. C194-C201.
91. Schwenk, W., *Theory of Stainless Steel Pitting.* Corrosion, 1964. **20**(4): p. T129-T137.
92. Leckie, H.P. and H.H. Uhlig, *Environmental Factors Affecting Critical Potential for Pitting in 18-8 Stainless Steel.* Journal of the Electrochemical Society, 1966. **113**(12): p. 1262-1267.
93. Donohoe, C.J., G.O.H. Whillock, and P.J. Apps, *Localized Corrosion of Stainless Steel in a Nuclear Waste Cooling Water System-Part 2: Plant Inspection Findings.* Corrosion, 2012. **68**(9): p. 844-852.
94. Lillard, R.S., G. Vasquez, and D.F. Bahr, *Influence of Nitrate on Pit Stability in Austenitic Stainless Steel.* Corrosion, 2010. **66**(7).

95. Toshima, Y., T. Hashimoto, K. Naitoh, E. Yamamoto, and Y. Kogawa, *Influence of Nitrate on Pitting Corrosion of Type-316l Stainless-Steel in Fgd Processes.* Journal of Chemical Engineering of Japan, 1982. **15**(1): p. 11-16.
96. Newman, R.C. and T. Shahrabi, *The Effect of Alloyed Nitrogen or Dissolved Nitrate Ions on the Anodic Behaviour of Austenitic Stainless-Steel in Hydrochloric-Acid.* Corrosion Science, 1987. **27**(8): p. 827-838.
97. Sazou, D. and M. Pagitsas, *Nitrate Ion Effect on the Passive Film Breakdown and Current Oscillations at Iron Surfaces Polarized in Chloride-Containing Sulfuric Acid Solutions.* Electrochimica Acta, 2002. **47**(10): p. 1567-1578.
98. Lohrengel, M.M., I. Kluppel, C. Rosenkranz, H. Bettermann, and J.W. Schultze, *Microscopic Investigations of Electrochemical Machining of Fe in NaNO3.* Electrochimica Acta, 2003. **48**(20-22): p. 3203-3211.
99. Rosenkranz, C., M.M. Lohrengel, and J.W. Schultze, *The Surface Structure During Pulsed ECM of Iron in NaNO3.* Electrochimica Acta, 2005. **50**(10): p. 2009-2016.
100. Hudson, J.L. and T.T. Tsotsis, *Electrochemical Reaction Dynamics - a Review.* Chemical Engineering Science, 1994. **49**(10): p. 1493-1572.
101. Evans, U.R., *Behaviour of Metals in Nitric Acid.* Transactions of the Faraday Society, 1944. **40**: p. 0120-0129.
102. Balbaud, F., G. Sanchez, P. Fauvet, G. Santarini, and G. Picard, *Mechanism of Corrosion of Aisi 304l Stainless Steel in the Presence of Nitric Acid Condensates.* Corrosion Science, 2000. **42**(10): p. 1685-1707.
103. Bandy, R. and D. Vanrooyen, *Properties of Nitrogen-Containing Stainless Alloy Designed for High-Resistance to Pitting.* Corrosion, 1985. **41**(4): p. 228-233.
104. Brossia, C.S. and R.G. Kelly, *Occluded Solution Chemistry Control and the Role of Alloy Sulfur on the Initiation of Crevice Corrosion in Type 304ss.* Corrosion Science, 1998. **40**(11): p. 1851-1871.
105. Li, X.J., H.B. Cong, F. Gui, C.S. Brossia, and G.S. Frankel, *Development of Liquid-Air-Interface Corrosion of Steel in Nitrate Solutions.* Corrosion, 2014. **70**(3): p. 230-246.
106. Newman, R.C., *2001 W.R. Whitney Award Lecture: Understanding the Corrosion of Stainless Steel.* Corrosion, 2001. **57**(12): p. 1030-1041.
107. Maurice, V., H. Peng, L.H. Klein, A. Seyeux, S. Zanna, and P. Marcus, *Effects of Molybdenum on the Composition and Nanoscale Morphology of Passivated Austenitic Stainless Steel Surfaces.* Faraday Discussions, 2015. **180**: p. 151-170.
108. Wanklyn, J.N., *The Role of Molybdenum in the Crevice Corrosion of Stainless-Steels.* Corrosion Science, 1981. **21**(3): p. 211-225.
109. Newman, R.C., *The Dissolution and Passivation Kinetics of Stainless Alloys Containing Molybdenum .1. Coulometric Studies of Fe-Cr and Fe-Cr-Mo Alloys.* Corrosion Science, 1985. **25**(5): p. 331-339.
110. Newman, R.C., *The Dissolution and Passivation Kinetics of Stainless Alloys Containing Molybdenum .2. Dissolution Kinetics in Artificial Pits.* Corrosion Science, 1985. **25**(5): p. 341-350.
111. Kimura, M., M. Kaneko, and N. Ohta, *In Situ Analysis of Pitting Corrosion in Artificial Crevice of Stainless Steel by X-Ray Absorption Fine Structure.* Isij International, 2002. **42**(12): p. 1399-1403.
112. Davenport, A.J., A.J. Dent, M. Monir, J.A. Hammons, S.M. Ghahari, P.D. Quinn, and T. Rayment, *Xanes Study of the Chemistry of Molybdenum in Artificial Corrosion Pits in 316l Stainless Steel.* Journal of the Electrochemical Society, 2011. **158**(5): p. C111-C117.
113. Schindelholz, E., B.E. Risteen, and R.G. Kelly, *Effect of Relative Humidity on Corrosion of Steel under Sea Salt Aerosol Proxies.* Journal of the Electrochemical Society, 2014. **161**(10): p. C460-C470.

114. Tsutsumi, Y., A. Nishikata, and T. Tsuru, *Pitting Corrosion Mechanism of Type 304 Stainless Steel under a Droplet of Chloride Solutions.* Corrosion Science, 2007. **49**(3): p. 1394-1407.
115. Schindelholz, E., B.E. Risteen, and R.G. Kelly, *Effect of Relative Humidity on Corrosion of Steel under Sea Salt Aerosol Proxies.* Journal of the Electrochemical Society, 2014. **161**(10): p. C450-C459.
116. Evans, U.R., *The Ferroxyl Indicator in Corrosion Research, with Special Reference to the Controversy Regarding the Cause of Pitting.* Metal Industry, 1926. **29**: p. 481-482.
117. Evans, U.R., *The Corrosion and Oxidation of Metals*. 1st ed1960, London: Edward Arnold Ltd.
118. Evans, U.R., *Oxygen Distribution as a Factor in the Corrosion of Metals.* Industrial & Engineering Chemistry, 1925. **17**(4): p. 363-372.
119. Chen, C.Y. and F. Mansfeld, *Potential Distribution in the Evans Drop Experiment.* Corrosion Science, 1997. **39**(2): p. 409-413.
120. Neufeld, A.K., I.S. Cole, A.M. Bond, and S.A. Furman, *The Initiation Mechanism of Corrosion of Zinc by Sodium Chloride Particle Deposition.* Corrosion Science, 2002. **44**(3): p. 555-572.
121. Cole, I.S., N.S. Azmat, A. Kanta, and M. Venkatraman, *What Really Controls the Atmospheric Corrosion of Zinc? Effect of Marine Aerosols on Atmospheric Corrosion of Zinc.* International Materials Reviews, 2009. **54**(3): p. 117-133.
122. King, P.C., I.S. Cole, P.A. Corrigan, A.E. Hughes, T.H. Muster, and S. Thomas, *Fib/Sem Study of Aa2024 Corrosion under a Seawater Drop, Part II.* Corrosion Science, 2012. **55**: p. 116-125.
123. King, P.C., I.S. Cole, P.A. Corrigan, A.E. Hughes, and T.H. Muster, *Fib/Sem Study of Aa2024 Corrosion under a Seawater Drop: Part I.* Corrosion Science, 2011. **53**(3): p. 1086-1096.
124. Oltra, R., B. Malki, and F. Rechou, *Influence of Aeration on the Localized Trenching on Aluminium Alloys.* Electrochimica Acta, 2010. **55**(15): p. 4536-4542.
125. Nam, T.V., E. Tada, and A. Nishikata, *Pit Initiation and Repassivation of Stainless Steels Exposed to Cyclic Relative Humidity Changes.* Journal of the Electrochemical Society, 2015. **162**(9): p. C419-C425.
126. Street, S.R., N. Mi, A.J.M.C. Cook, H.B. Mohammed-Ali, L. Guo, T. Rayment, and A.J. Davenport, *Atmospheric Pitting Corrosion of 304l Stainless Steel: The Role of Highly Concentrated Chloride Solutions.* Faraday Discussions, 2015.
127. Thomas, S., I.S. Cole, and N. Birbilis, *Compact Oxides Formed on Zinc During Exposure to a Single Sea-Water Droplet.* Journal of the Electrochemical Society, 2013. **160**(2): p. C59-C63.
128. Wang, Y.H., W. Wang, Y.Y. Liu, L. Zhong, and J. Wang, *Study of Localized Corrosion of 304 Stainless Steel under Chloride Solution Droplets Using the Wire Beam Electrode.* Corrosion Science, 2011. **53**(9): p. 2963-2968.
129. Wang, Y.H. and Y.Y. Liu, *Localized Corrosion of 304 Stainless Steel under a Nacl Droplet*, in *Materials Engineering for Advanced Technologies, Pts 1 and 2*, Y.W. Wu, Editor 2011. p. 443-447.
130. Tsuru, T., K.I. Tamiya, and A. Nishikata, *Formation and Growth of Micro-Droplets During the Initial Stage of Atmospheric Corrosion.* Electrochimica Acta, 2004. **49**(17-18): p. 2709-2715.
131. Mohammed-Ali, H.B., *Atmospheric Pitting Corrosion of Stainless Steel,* , in *Metallurgy and Materials*2016, University of Birmingham: Birmingham.
132. Wang, J., L.H. Liang, and J. Jiang, *The Role of Electrochemical Polarization in Micro-Droplets Formation.* Electrochemistry Communications, 2008. **10**(11): p. 1788-1791.

133. Li, J.F., B. Maier, and G.S. Frankel, *Corrosion of an Al-Mg-Si Alloy under MgCl2 Solution Droplets.* Corrosion Science, 2011. **53**(6): p. 2142-2151.
134. Morton, S.C. and G.S. Frankel, *Atmospheric Pitting Corrosion of Aa7075-T6 under Evaporating Droplets with and without Inhibitors.* Materials and Corrosion-Werkstoffe Und Korrosion, 2014. **65**(4): p. 351-361.
135. Frankel, G.S., M. Stratmann, M. Rohwerder, A. Michalik, B. Maier, J. Dora, and M. Wicinski, *Potential Control under Thin Aqueous Layers Using a Kelvin Probe.* Corrosion Science, 2007. **49**(4): p. 2021-2036.
136. Maier, B. and G.S. Frankel, *Pitting Corrosion of Bare Stainless Steel 304 under Chloride Solution Droplets.* Journal of the Electrochemical Society, 2010. **157**(10): p. C302-C312.
137. Winsley, R.J., N.R. Smart, B. Reddy, A.P. Rance, and P.A.H. Fennell, *4 Meter Box Monitoring Programme - Final Report for the Period 2007-2010 - Serco/Tcs/006028.01/Issue001/Finalreport.*, 2011, Serco.
138. Azmat, N.S., K.D. Ralston, B.C. Muddle, and I.S. Cole, *Corrosion of Zn under Fine Size Aerosols and Droplets Using Inkjet Printer Deposition and Optical Profilometry Quantification.* Corrosion Science, 2011. **53**(11): p. 3534-3541.
139. Mi, N., M. Ghahari, T. Rayment, and A.J. Davenport, *Use of Inkjet Printing to Deposit Magnesium Chloride Salt Patterns for Investigation of Atmospheric Corrosion of 304 Stainless Steel.* Corrosion Science, 2011. **53**(10): p. 3114-3121.
140. Schindelholz, E. and R.G. Kelly, *Application of Inkjet Printing for Depositing Salt Prior to Atmospheric Corrosion Testing.* Electrochemical and Solid State Letters, 2010. **13**(10): p. C29-C31.
141. Chen, Z.Y., D. Persson, and C. Leygraf, *Initial Nacl-Particle Induced Atmospheric Corrosion of Zinc-Effect of CO2 and SO2.* Corrosion Science, 2008. **50**(1): p. 111-123.
142. Hihara, L.H. and S. Li, *Atmospheric Corrosion Initiation on Steel from Predeposited Nacl Salt Particles in High Humidity Atmospheres.* Corrosion Engineering, Science and Technology, 2010. **45**(1): p. 49-56.
143. Lobnig, R., J.D. Sinclair, M. Unger, and M. Stratmann, *Mechanism of Atmospheric Corrosion of Copper in the Presence of Ammonium Sulfate Particles - Effect of Surface Particle Concentration.* Journal of the Electrochemical Society, 2003. **150**(6): p. A835-A849.
144. Cole, I.S., D. Lau, and D.A. Paterson, *Holistic Model for Atmospheric Corrosion - Part 6 - from Wet Aerosol to Salt Deposit.* Corrosion Engineering Science and Technology, 2004. **39**(3): p. 209-218.
145. Chen, Z.Y., D. Persson, A. Nazarov, S. Zakipour, D. Thierry, and C. Leygraf, *In Situ Studies of the Effect of CO2 on the Initial Nacl-Induced Atmospheric Corrosion of Copper.* Journal of the Electrochemical Society, 2005. **152**(9): p. B342-B351.
146. Stratmann, M. and H. Streckel, *On the Atmospheric Corrosion of Metals Which Are Covered with Thin Electrolyte Layers .1. Verification of the Experimental-Technique.* Corrosion Science, 1990. **30**(6-7): p. 681-696.
147. Stratmann, M. and H. Streckel, *On the Atmospheric Corrosion of Metals Which Are Covered with Thin Electrolyte Layers .2. Experimental Results.* Corrosion Science, 1990. **30**(6-7): p. 697-714.
148. Stratmann, M., H. Streckel, K.T. Kim, and S. Crockett, *On the Atmospheric Corrosion of Metals Which Are Covered with Thin Electrolyte Layers .3. The Measurement of Polarization Curves on Metal-Surfaces Which Are Covered by Thin Electrolyte Layers.* Corrosion Science, 1990. **30**(6-7): p. 715-734.
149. Tada, E. and G.S. Frankel, *Effects of Particulate Silica Coatings on Localized Corrosion Behavior of Aisi 304ss under Atmospheric Corrosion Conditions.* Journal of the Electrochemical Society, 2007. **154**(6): p. C318-C325.

150. Cruz, R.P.V., A. Nishikata, and T. Tsuru, *Pitting Corrosion Mechanism of Stainless Steels under Wet-Dry Exposure in Chloride-Containing Environments.* Corrosion Science, 1998. **40**(1): p. 125-139.
151. Wang, Y.H., Y.Y. Liu, W. Wang, L. Zhong, and J. Wang, *Influences of the Three-Phase Boundary on the Electrochemical Corrosion Characteristics of Carbon Steel under Droplets.* Materials and Corrosion-Werkstoffe Und Korrosion, 2013. **64**(4): p. 309-313.
152. Mankowski, J. and Z. Szklarskasmialowska, *Effect of Specimen Position on Shape of Corrosion Pits in an Austenitic Stainless-Steel.* Corrosion Science, 1977. **17**(9): p. 725-735.
153. Ernst, P., N.J. Laycock, M.H. Moayed, and R.C. Newman, *The Mechanism of Lacy Cover Formation in Pitting.* Corrosion Science, 1997. **39**(6): p. 1133-1136.
154. Ernst, P., M.H. Moayed, N.J. Laycock, and R.C. Newman, *Shapes of Corrosion Pits in Metals*. Proceedings of the International Symposium on Pits and Pores: Formation, Properties, and Significance for Advanced Luminescent Materials, ed. P. Schmuki, et al. Vol. 97. 1997. 176-185.
155. Rosenfeld, I.L. and I.S. Danilov, *Electrochemical Aspects of Pitting Corrosion.* Corrosion Science, 1967. **7**(3): p. 129-142.
156. Pickering, H.W., *Transition from Internal to External Oxidation in Ternary Alloys.* Journal of the Electrochemical Society, 1972. **119**(5): p. 641-649.
157. Davenport, A.J., L. Guo, N. Mi, H. Mohammed-Ali, S.M. Ghahari, S.R. Street, N.J. Laycock, T. Rayment, C. Reinhard, C. Padovani, and D. Krouse, *Mechanistic Studies of Atmospheric Pitting Corrosion of Stainless Steel for ILW Containers.* Corrosion Engineering, Science and Technology, 2014. **49**(6): p. 514-520.
158. Laycock, N.J. and S.P. White, *Computer Simulation of Single Pit Propagation in Stainless Steel under Potentiostatic Control.* Journal of the Electrochemical Society, 2001. **148**(7): p. B264-B275.
159. Frankel, G.S., *The Growth of 2-D Pits in Thin-Film Aluminum.* Corrosion Science, 1990. **30**(12): p. 1203-1218.
160. Sato, N., *The Stability of Pitting Dissolution of Metals in Aqueous-Solution.* Journal of the Electrochemical Society, 1982. **129**(2): p. 260-264.
161. Sato, N., *The Stability of Localized Corrosion.* Corrosion Science, 1995. **37**(12): p. 1947-1967.
162. Hastuty, S., A. Nishikata, and T. Tsuru, *Pitting Corrosion of Type 430 Stainless Steel under Chloride Solution Droplet.* Corrosion Science, 2010. **52**(6): p. 2035-2043.
163. Chen, Z.Y. and R.G. Kelly, *Computational Modeling of Bounding Conditions for Pit Size on Stainless Steel in Atmospheric Environments.* Journal of the Electrochemical Society, 2010. **157**(2): p. C69-C78.
164. Willmott, P., *An Introduction to Synchrotron Radiation,* 2011, Villigen: John Wiley and Sons.
165. www.howitworksdaily.com. *Electron Guns*. 2014 22 September 2016]; Available from: www.diamond.ac.uk/PressOffice/dms/Media/140811_How-It-Works/140811_How%2520It%2520Works.pdf.
166. Thompson, S.P., J.E. Parker, J. Marchal, J. Potter, A. Birt, F. Yuan, R.D. Fearn, A.R. Lennie, S.R. Street, and C.C. Tang, *Fast X-Ray Powder Diffraction on I11 at Diamond.* Journal of Synchrotron Radiation, 2011. **18**: p. 637-648.
167. Drakopoulos, M., T. Connolley, C. Reinhard, R. Atwood, O. Magdysyuk, N. Vo, M. Hart, L. Connor, B. Humphreys, G. Howell, S. Davies, T. Hill, G. Wilkin, U. Pedersen, A. Foster, N. De Maio, M. Basham, F.J. Yuan, and K. Wanelik, *I12: The Joint Engineering, Environment and Processing (Jeep) Beamline at Diamond Light Source.* Journal of Synchrotron Radiation, 2015. **22**: p. 828-838.

168. Cullity, B.D. and S.R. Stock, *Elements of X-Ray Diffraction*. 3rd ed2001, New Jersey: Prentice Hall.
169. Dowsett, M., A. Adriaens, C. Martin, and L. Bouchenoire, *The Use of Synchrotron X-Rays to Observe Copper Corrosion in Real Time.* Analytical Chemistry, 2012. **84**(11): p. 4866-4872.
170. Ko, M., N.J. Laycock, B. Ingham, and D.E. Williams, *In Situ Synchrotron X-Ray Diffraction Studies of CO2 Corrosion of Carbon Steel with Scale Inhibitors Atmpa and Pei at 80 Degrees C.* Corrosion, 2012. **68**(12): p. 1085-1093.
171. Ghahari, S.M., A.J. Davenport, T. Rayment, T. Suter, J.P. Tinnes, C. Padovani, J.A. Hammons, M. Stampanoni, F. Marone, and R. Mokso, *In Situ Synchrotron X-Ray Micro-Tomography Study of Pitting Corrosion in Stainless Steel.* Corrosion Science, 2011. **53**(9): p. 2684-2687.
172. Hammons, J.A., A.J. Davenport, S.M. Ghahari, M. Monir, J.P. Tinnes, M. Amri, N. Terrill, F. Marone, R. Mokso, M. Stampanoni, and T. Rayment, *Interfacial Phenomena During Salt Layer Formation under High Rate Dissolution Conditions.* Journal of Physical Chemistry B, 2013. **117**(22): p. 6724-6732.
173. Nagy, Z. and H. You, *Radiolytic Effects on the in-Situ Investigation of Buried Interfaces with Synchrotron X-Ray Techniques.* Journal of Electroanalytical Chemistry, 1995. **381**(1-2): p. 275-279.
174. Mosselmans, J.F.W., P.D. Quinn, A.J. Dent, S.A. Cavill, S.D. Moreno, A. Peach, P.J. Leicester, S.J. Keylock, S.R. Gregory, K.D. Atkinson, and J.R. Rosell, *I18-the Microfocus Spectroscopy Beamline at the Diamond Light Source.* Journal of Synchrotron Radiation, 2009. **16**: p. 818-824.
175. De Nolf, W. and K. Janssens, *Micro X-Ray Diffraction and Fluorescence Tomography for the Study of Multilayered Automotive Paints.* Surface and Interface Analysis, 2010. **42**(5): p. 411-418.
176. Rau, C., U. Wagner, Z. Pesic, and A. De Fanis, *Coherent Imaging at the Diamond Beamline I13.* Physica Status Solidi a-Applications and Materials Science, 2011. **208**(11): p. 2522-2525.
177. Aishima, J., M. Basham, P. Chang, B. El Kassaby, J. Filik, M. Gerring, K. Levik, I. Sikharulidze, M. Webber, and A. Ashton. *Dawn Science V1.6 (Dls Edition)*. 2014; Available from: https://zenodo.org/record/12478.
178. Verbist, J.J., T.F. Koetzle, M.S. Lehmann, and W.C. Hamilton, *Neutron-Diffraction Study of Iron(II) Chloride Tetrahydrate, FeCl2.4h2o.* Journal of Chemical Physics, 1972. **56**(7): p. 3257-&.
179. Militky, J. and V. Bajzik, *Surface Roughness and Fractal Dimension.* Journal of the Textile Institute, 2001. **92**(3): p. 91-113.
180. Frankel, G., G. Thornton, S. Street, T. Rayment, D. Williams, A. Cook, A. Davenport, S. Gibbon, D. Engelberg, C. Ornek, A. Mol, P. Marcus, D. Shoesmith, C. Wren, K. Yliniemi, G. Williams, S. Lyon, R. Lindsay, T. Hughes, J. Lutzenkirchen, S.-T. Cheng, J. Scully, S.F. Lee, R. Newman, C. Taylor, R. Springell, J. Mauzeroll, S. Virtanen, S. Heurtault, and J. Sullivan, *Localised Corrosion: General Discussion.* Faraday Discussions, 2015. **180**(0): p. 381-414.
181. *Standard Guide for Examination and Evaluation of Pitting Corrosion*, in *ASTM Standard G46-94*2013, ASTM International.
182. Turnbull, A., K. Mingard, J.D. Lord, B. Roebuck, D.R. Tice, K.J. Mottershead, N.D. Fairweather, and A.K. Bradbury, *Sensitivity of Stress Corrosion Cracking of Stainless Steel to Surface Machining and Grinding Procedure.* Corrosion Science, 2011. **53**(10): p. 3398-3415.
183. OLI Systems, I., *Oli Analyzer 9.0*, 2013.

184. Cole, I.S., T.H. Muster, D. Lau, N. Wright, and N.S. Azmat, *Products Formed During the Interaction of Seawater Droplets with Zinc Surfaces II. Results from Short Exposures.* Journal of the Electrochemical Society, 2010. **157**(6): p. C213-C222.
185. *Matlab and Statistic Toolbox Release,* , 2011, The MathWorks, Inc.: Natick, Massachusetts, United States.
186. Chen, Z.Y. and R.G. Kelly, *An Analytical Modeling Method for Calculating the Maximum Cathode Current Deliverable by a Circular Cathode under Atmospheric Exposure*, in *Simulation of Electrochemical Processes II*, V.G. DeGiorgi, C.A. Brebbia, and R.A. Adey, Editors. 2007. p. 33-41.
187. Chen, Z.Y., F. Cui, and R.G. Kelly, *Calculations of the Cathodic Current Delivery Capacity and Stability of Crevice Corrosion under Atmospheric Environments.* Journal of the Electrochemical Society, 2008. **155**(7): p. C360-C368.
188. Webb, E.G. and R.C. Alkire, *Pit Initiation at Single Sulfide Inclusions in Stainless Steel - I. Electrochemical Microcell Measurements.* Journal of the Electrochemical Society, 2002. **149**(6): p. B272-B279.
189. Zhang, J., J. Wang, and Y. Wang, *Micro-Droplets Formation During the Deliquescence of Salt Particles in Atmosphere.* Corrosion, 2005. **61**(12): p. 1167-1172.
190. Gunther, M., N.P.C. Stevens, G. McFiggans, and A.B. Cook, *Investigation into Composition and Deposition of Artificially Produced Marine Aerosols on Austenitic Stainless Steels.* Corrosion Engineering Science and Technology, 2014. **49**(6): p. 509-513.
191. Risteen, B.E., E. Schindelholz, and R.G. Kelly, *Marine Aerosol Drop Size Effects on the Corrosion Behavior of Low Carbon Steel and High Purity Iron.* Journal of the Electrochemical Society, 2014. **161**(14): p. C580-C586.
192. Maurice, V., G. Despert, S. Zanna, M.P. Bacos, and P. Marcus, *Self-Assembling of Atomic Vacancies at an Oxide/Intermetallic Alloy Interface.* Nature Materials, 2004. **3**(10): p. 687-691.
193. Jun, J., G.S. Frankel, and N. Sridhar, *Effect of Chloride Concentration and Temperature on Growth of 1d Pit.* Journal of Solid State Electrochemistry, 2015. **19**(12): p. 3439-3447.
194. Wallinder, D., J. Pan, C. Leygraf, and A. Delblanc-Bauer, *Eis and XPS Study of Surface Modification of 316lvm Stainless Steel after Passivation.* Corrosion Science, 1999. **41**(2): p. 275-289.
195. Isaacs, H.S. and G. Kissel, *Surface Preparation and Pit Propagation in Stainless-Steels.* Journal of the Electrochemical Society, 1972. **119**(12): p. 1628-&.
196. Monir, M., *Xanes Study of Chemistry of Localised Corrosion in Artificial Pits of 316l Stainless Steel and Titanium.*, in *School of Metallurgy and Materials*2011, University of Birmingham: Birmingham.
197. Pardo, A., E. Otero, M.C. Merino, M.D. Lopez, M.V. Utrilla, and F. Moreno, *Influence of pH and Chloride Concentration on the Pitting and Crevice Corrosion Behavior of High-Alloy Stainless Steels.* Corrosion, 2000. **56**(4): p. 411-418.
198. Sridhar, N. and G.A. Cragnolino, *Applicability of Repassivation Potential for Long-Term Prediction of Localized Corrosion of Alloy-825 and Type-316l Stainless-Steel.* Corrosion, 1993. **49**(11): p. 885-894.
199. Wang, P., A. Anderko, and R.D. Young, *Modeling Electrical Conductivity in Concentrated and Mixed-Solvent Electrolyte Solutions.* Industrial & Engineering Chemistry Research, 2004. **43**(25): p. 8083-8092.
200. Anderko, A. and M.M. Lencka, *Computation of Electrical Conductivity of Multicomponent Aqueous Systems in Wide Concentration and Temperature Ranges.* Industrial & Engineering Chemistry Research, 1997. **36**(5): p. 1932-1943.

201. Smart, N.G. and J.O.M. Bockris, *Effect of Water Activity on Corrosion.* Corrosion, 1992. **48**(4): p. 277-280.
202. Srinivasan, J., M.J. McGrath, and R.G. Kelly, *A High-Throughput Artificial Pit Technique to Measure Kinetic Parameters for Pitting Stability.* Journal of the Electrochemical Society, 2015. **162**(14): p. C725-C731.
203. Jargelius-Pettersson, R.F.A. and B.G. Pound, *Examination of the Role of Molybdenum in Passivation of Stainless Steels Using Ac Impedance Spectroscopy.* Journal of the Electrochemical Society, 1998. **145**(5): p. 1462-1469.
204. Goetz, R. and D. Landolt, *The Influence of Chromium Content and Potential on the Surface-Composition of Fe-Cr-Mo Alloys Studied by AES.* Electrochimica Acta, 1984. **29**(5): p. 667-676.
205. Landolt, D., S. Mischler, A. Vogel, and H.J. Mathieu, *Chloride-Ion Effects on Passive Films on Fecr and Fecrmo Studied by AES, XPS and SIMS.* Corrosion Science, 1990. **31**: p. 431-440.
206. Yaniv, A.E., J.B. Lumsden, and R.W. Staehle, *Composition of Passive Films on Ferritic Stainless-Steels.* Journal of the Electrochemical Society, 1977. **124**(4): p. 490-496.
207. Kaneko, M. and H.S. Isaacs, *Effects of Molybdenum on the Pitting of Ferritic- and Austenitic-Stainless Steels in Bromide and Chloride Solutions.* Corrosion Science, 2002. **44**(8): p. 1825-1834.
208. Clayton, C.R. and Y.C. Lu, *A Bipolar Model of the Passivity of Stainless-Steel - the Role of Mo Addition.* Journal of the Electrochemical Society, 1986. **133**(12): p. 2465-2473.
209. Newman, R.C. and E.M. Franz, *Growth and Repassivation of Single Corrosion Pits in Stainless-Steel.* Corrosion, 1984. **40**(7): p. 325-330.
210. Prosek, T., A. Iversen, C. Taxen, and D. Thierry, *Low-Temperature Stress Corrosion Cracking of Stainless Steels in the Atmosphere in the Presence of Chloride Deposits.* Corrosion, 2009. **65**(2): p. 105-117.
211. Ernst, P. and R.C. Newman, *The Interaction between Alloyed Molybdenum and Dissolved Bromide in the Pitting Corrosion of Stainless Steels.* Electrochemical and Solid State Letters, 2008. **11**(1): p. C1-C4.
212. Laycock, N.J., M.H. Moayed, and R.C. Newman, *Metastable Pitting and the Critical Pitting Temperature.* Journal of the Electrochemical Society, 1998. **145**(8): p. 2622-2628.
213. Betts, A.J. and R.C. Newman, *The Effect of Alloyed Molybdenum on the Activation of Anodic-Dissolution by Reduced Sulfur-Compounds.* Corrosion Science, 1993. **34**(9): p. 1551-1555.
214. Seyeux, A., V. Maurice, and P. Marcus, *Breakdown Kinetics at Nanostructure Defects of Passive Films.* Electrochemical and Solid State Letters, 2009. **12**(10): p. C25-C27.
215. Lillard, R.S., *A Review of Corrosion Issues Related to Uranyl Nitrate Base Aqueous Homogeneous Reactors.* Corrosion Engineering Science and Technology, 2010. **45**(3): p. 194-203.
216. Lohrengel, M.M., C. Rosenkranz, and D. Rohrbeck, *The Iron/Electrolyte Interface at Extremely Large Current Densities.* Microchimica Acta, 2006. **156**(1-2): p. 163-166.
217. Woldemedhin, M.T., D. Raabe, and A.W. Hassel, *Grain Boundary Electrochemistry of Beta-Type Nb-Ti Alloy Using a Scanning Droplet Cell.* Physica Status Solidi a-Applications and Materials Science, 2011. **208**(6): p. 1246-1251.
218. Albores-Silva, O.E., E.A. Charles, and C. Padovani, *Effect of Chloride Deposition on Stress Corrosion Cracking of 316l Stainless Steel Used for Intermediate Level Radioactive Waste Containers.* Corrosion Engineering Science and Technology, 2011. **46**(2): p. 124-128.

219. Clark, B.E., S.J. Thorpe, and K.T. Aust, *The Pitting Behavior of Fe-Ni-Cr-Mo Alloys.* Corrosion Science, 1990. **31**: p. 551-556.
220. Garland, J.E., C.M. Pettit, and D. Roy, *Analysis of Experimental Constraints And. Variables for Time Resolved Detection of Fourier Transform Electrochemical Impedance Spectra.* Electrochimica Acta, 2004. **49**(16): p. 2623-2635.
221. Payton, O.D., L. Picco, and T.B. Scott, *High-Speed Atomic Force Microscopy for Materials Science.* International Materials Reviews, 2016. **61**(8): p. 473-494.